UNIVERSITY OF
Southampton

Study of Inorganic Transparent Materials with Near-Infrared Absorbing Properties

by
Florian Norindr

A thesis submitted in partial fulfillment for the degree of Doctor of Philosophy

in the
Faculty of Engineering, Science and Mathematics
School of Chemistry

September 2009

DECLARATION OF AUTHORSHIP

I, Florian Norindr, declare that this thesis titled "Study of Inorganic Transparent Materials with Near-Infrared Absorbing Properties" and the work presented in it are my own. I confirm that:

- This work was done wholly or mainly while in candidature for a research degree at this University.
- Where any part of this thesis has previously been submitted for a degree or any other qualification at this University or any other institution, this has been clearly stated.
- Where I have consulted the published work of others, this is always clearly attributed.
- Where I have quoted from the work of others, the source is always given. With the exception of such quotations, this thesis is entirely my own work.
- I have acknowledged all main sources of help.
- Where the thesis is based on work done by myself jointly with others, I have made clear exactly what was done by others and what I have contributed myself.

Signed:_____

Date:_____

UNIVERSITY OF SOUTHAMPTON

Abstract

Faculty of Engineering, Science and Mathematics

School of Chemistry

Doctor of Philosophy

Study of Inorganic Transparent Materials with Near-Infrared Absorbing Properties

by Florian Norindr

The pigments investigated in this thesis were synthesised and characterised in order to find promising candidates for near-infrared absorbers. The chemical systems were chosen due to their absorbing properties and also their chemical and thermal stability and non-toxicity as well as for economical reasons. Investigations were undertaken on several phosphates and silicates.

Within the group of phosphates, first several known copper compounds, *i.e.* $Cu_2P_2O_7$, $Cu_4P_2O_9$, $Cu_5P_2O_{10}$, $Cu_3(PO_4)_2$, $Cu(PO_3)_2$ and $Cu_2P_4O_{12}$, were tested and the most suitable were chosen for more detailed experiments. The structure types with the general formula $M_2P_2O_7$ were found to be promising and the metals calcium, strontium and copper were investigated as a starting point. It was confirmed that $M_2P_2O_7$ (with M = Ca or Sr) and $Cu_2P_2O_7$ could only form a pigment material for the middle member *e.g.* $MCuP_2O_7$.

Better candidates were found in the systems Mg/Cu and Zn/Cu. Here solid solutions occur and the absorption behaviour could be adjusted according to the ratio of the metal cations. A series of different cation ratio compounds were synthesised for both systems. As Zn/Cu shows more favourable absorption properties compared to Mg/Cu, a full investigation of structural parameters including neutron powder diffraction and EXAFS studies was undertaken and the influence of the shape of M–O coordination spheres on the near-infrared absorption properties is discussed in detail.

After deriving the successful concept it was investigated in two further chemical systems. First, the cation Fe^{2+} was used into the $Zn_3(PO_4)_2$ structure to form a solid solution $(Zn,Fe)_3(PO_4)_2$ and then Cu^{2+} was introduced into the $Mg_2Si_2O_6$ pyroxene structure.

Resulting from the studies, three promising systems for transparent near-infrared absorbing pigment applications were isolated: $(Zn,Cu)_2P_2O_7$, $(Zn,Fe)_3(PO_4)_2$ and $(Mg,Cu)_2Si_2O_6$ solid solutions.

ACKNOWLEDGEMENTS

I wish to thank Professor Mark Weller for his help and encouragement through this entire project. In addition I would like to thank Dr Reinhold Rueger and Rodney Riddle from the pigment division of Merck Chemicals for their financial help and their ideas through the duration of this project. I would also like to thank the EPSRC for their financial support for my course and conference trips abroad.

I have to thank everyone from the inorganic materials group with whom I have worked. In particular Dr Sergio Russu who help me through the process of EXAFS refinement, Peter Hickey who spent some time explaining the basis of Rietveld refinement and Rosa Galati and Eleni Kotsapa without whom the group would have been too quiet.

Dr Alexandra Lieb and Dr Valeska Ting need a special mention for encouraging me through the writing process and cheering me up. Their expertise, advice and grammatical correctness helped me a lot to shape this document into form.

I would also like to thank Otello Maria Roscioni who has been a great friend and who showed me how to use LaTeX to produce my thesis using this formatting tool.

Finally I have to give special thanks to my family for their trust and support especially when I needed it. Their love gave me hope even during the most frustrating moments.

INDEX

CHAPTER 1

INTRODUCTION

Pigments have been used since the existence of mankind to embellish life with colour and carry a message through time [1]. However, the majority of synthetic pigments were only discovered within the past two or three centuries. The purpose of these materials has evolved to become more functional. Indeed, a lot of recent attention has been focussed on enhancing the physical and chemical properties of these materials. For many applications inorganic materials are preferred over organic systems, due to their greater photo-, thermo- and chemical stabilities.

Inorganic pigments are by far the most common colouring materials used in the world. Around 96% of all pigments synthesised world-wide are inorganic pigments [2], hence they form a fundamental class of pigments with widespread applications. They are most frequently utilised in plastics, paints and varnishes, printing inks, rubber, cosmetics, ceramic glazes and enamels.

A modern definition of pigments characterises these materials as particulate inorganic solids which are insoluble and physically and chemically unaffected by the substrate into which they are incorporated and which alter appearance by selective absorption and/or scattering of light [3]. The substrate can be of any kind, plastic, polymeric or water, oil, *etc*.

As there is a wide variety of pigments available they tend to be classified into several sub-categories, which are summarised below in Table 1.1 .

Recently a new category has emerged. Indeed, for these new functional materials

Table 1.1: Classification of inorganic pigments [3].

Term	Definition
white pigments	the optical effect is caused by non selective light scattering (examples: titanium dioxide and zinc sulfide pigments, lithopone, zinc white)
coloured pigments	the optical effect is caused by selective light absorption and also to a large extent by selective light scattering (examples: iron oxide red and yellow, cadmium pigments, ultramarine pigments, chrome yellow, cobalt blue)
black pigments	the optical effect is caused by non selective light absorption (examples: carbon black pigment, iron oxide black)
effect pigments	the optical effect is caused by regular reflection or interference
metal effect pigments	regular reflection takes place on mainly flat and parallel metallic pigment particles (example: aluminium flakes)
pearl luster pigments	regular reflection takes place on highly refractive parallel pigment platelets (example: titanium dioxide on mica)
interference pigments	the optical effect of coloured luster pigments is caused mainly or completely by the phenomenon of interference (example: iron oxide on mica)
luminescent pigments	the optical effect is caused by the capacity to absorb radiation and to emit it as light of a longer wavelength
fluorescent pigments	the light of longer wavelength is emitted after excitation without a delay (example: silver-doped zinc sulfide)
phosphorescent pigments	the light of longer wavelength is emitted within several hours after excitation (example: copper-doped zinc sulfide)

the colour property is not primordial and sometimes no interaction in the visible is even desired. Typical pigments of this type are magnetic pigments like Fe_3O_4 [4] and γFe_2O_3 [5] used in magnetic information storage systems such as audio and videocassettes, floppy disks, hard disks [3] or anticorrosive pigments like the red lead (Pb_3O_4)

or $CaCrO_4$ used mainly as protective films on metallic materials [6].

Other pigments have changed categories, this is the case for TiO_2 or ZnO. These white pigments are used now in sunscreen lotions as active broadband sunscreens that screen both UVB (290 - 320 nm) and UVA (320 - 400 nm) sunlight radiation [7].

Finally, driven by national laws and regulations in the ecological and toxicological area, the industries and the major consumers for pigment materials have produced non toxic materials such as rare earth metal pigments (cerium based) and environmentally active pigments to control, for example the heat inside a building to lower energy consumption.

1.1 Origin of Colour

To speak about colour or the absence of colour, one has to speak about the origin of colour. In fact there is more than one reason for a pigment to appear coloured and by understanding the reasons, it is possible to design pigments with specific properties.

Optical properties of materials derive from interactions with light. When photons enter a pigment they can be either absorbed, scattered or transmitted by the particles. Depending on the strength of these three complementary phenomena, the particulate material will have a certain colour. However if these phenomena take place in different regions than the visible, the human eye will see the material as colourless/white.

Titanium dioxyde (TiO_2) for example appears white because none of the visible wavelengths are absorbed, scattering back to the eye the entire range it is sensitive to [8]. On the other hand, the specific colour of Egyptian blue ($CaCuSi_4O_{10}$ [9]) is due to the absorption of only the red part of the visible.

For most inorganic materials, absorption takes place because the incident wavelength is of the same energy as the difference between two quantised levels of energy within the electron shell of the involved atoms. Characterization of these levels of energy and the way they occur in pigments gives control over the optical properties of the compound.

1.1.1 Electronic Transitions

d - *d* Transitions

The cause of colour for transition metal complexes involves the electron distribution within the *d* orbitals (Figure 1.1). This is for example the reason for the intense purple colour of $[Ti(H_2O)_6]^{3+}$, an octahedral complex [10].

The five *d* orbitals are usually separated into two sets depending of the arrangement of the ligands surrounding the transition metal. Indeed, for an isolated transition metal ion, all of its orbitals are degenerate *i.e.* they have the same energy. Once the transition metal atom starts to be coordinated to ligands, the increasing repulsion be-

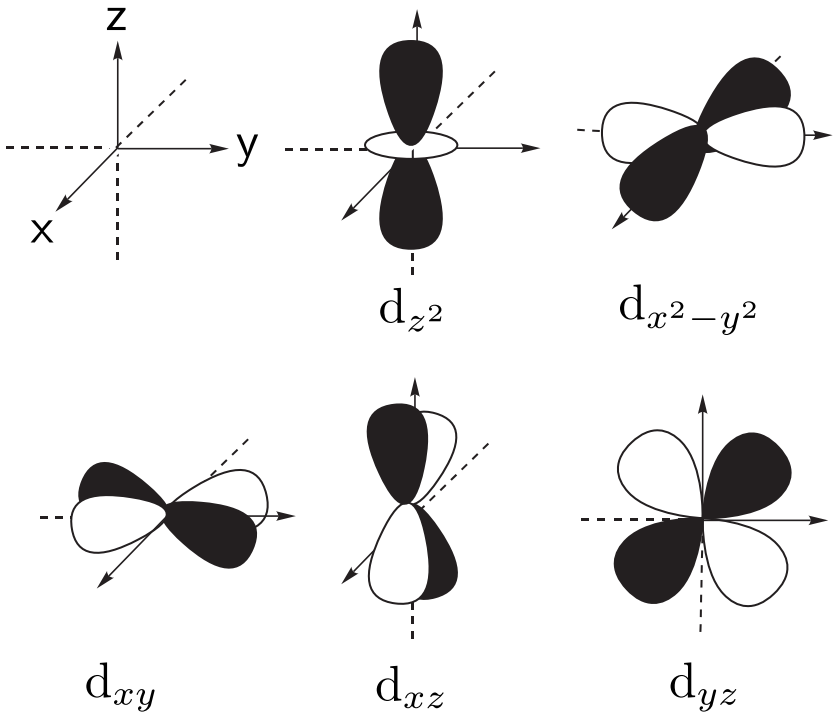

Figure 1.1: The five *d* orbitals. The shaded and unshaded areas represent lobes of different signs [11].

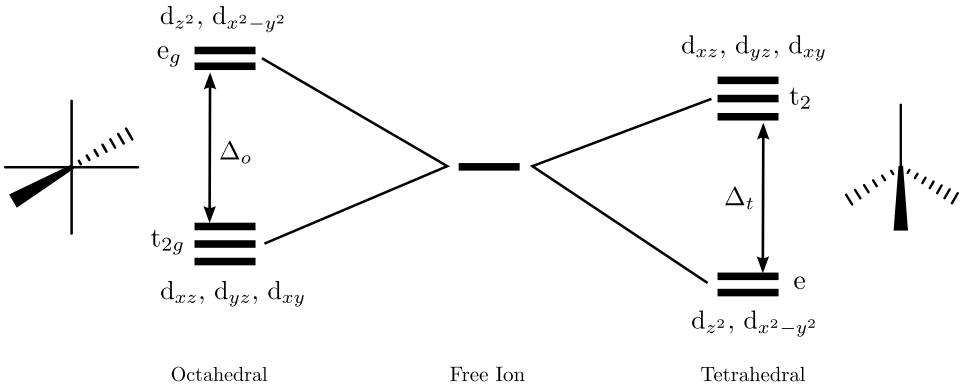

Figure 1.2: Orbital splitting in an octahedral and tetrahedral symmetry.

tween the electron cloud surrounding the ligand and some of the *d* orbitals, splits them into groups of distinct energy. This is known as crystal field splitting and for common configuration, such as octahedral or tetrahedral, the energy difference is quantified as Δ_o or Δ_t respectively (Figure 1.2). Absorption of photons is the direct consequence of

this splitting; electrons from one orbital of low energy can be excited and if the energy matches the crystal field splitting they move to the higher energy orbital. For an octahedral complex this is a $t_{2g} \rightarrow e_g$ transition which is typically situated in the visible region of the electromagnetic spectrum.

Fundamentally, *d* - *d* transitions are spin allowed as there is no change in electron spin, but symmetry forbidden for centrosymmetric species (*Laporte rule*). Indeed, transitions involving the redistribution of electrons in a single quantum shell are forbidden. That means $s \rightarrow d$ or $p \rightarrow d$ transitions are allowed, but $d \rightarrow d$ is forbidden unless the symmetry is reduced by vibration or distortion of the perfect shape [12].

Tetrahedral symmetry (T_d) does not suffer from this rule. Indeed, transition metal complexes of T_d symmetry can be described by involving a combination of sp^3 and sd^3 hybridation of the metal atom orbitals. The mixing of *p* orbital character with *d* character relaxes the *Laporte rule* [13]. Therefore these transitions are more intense and tend to dominate the electronic spectrum.

On the other hand, octahedral symmetry O_h is prone to this selection rule. However, if a solid state vibrational mode is not possible, distortion from regular symmetry is often encountered.

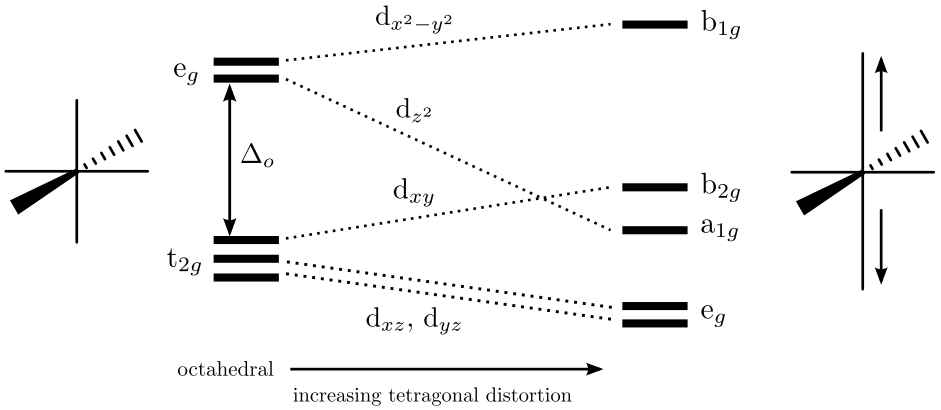

Figure 1.3: Orbital correlation diagram showing the effect of an increasing tetragonal distortion on octahedral symmetry.

The most common distortion is a tetragonal distortion; two ligands trans to each

Table 1.2: Intensities of spectroscopic bands in 3*d* complexes [17].

Band Type	ϵ_{max} ($dm^3mol^{-1}cm^{-1}$)	Type of Transition
spin forbidden	< 1	*d* - *d* (*e.g.* Mn^{2+}, d^5)
Laporte forbidden	20 - 100	*d* - *d* (*e.g.* O_h)
Laporte allowed	*ca.* 250	*d* - *d* (*e.g.* T_d)
symmetry allowed	1000 - 5000	charge transfer

other are either closer or further away from the metal centre than are the other four equatorial ligands [14]. This distortion follows the *Jahn Teller theorem* which states that for a nonlinear molecule in an electronically degenerate state, distortion must occur to lower the symmetry, remove the degeneracy and lower the energy [15, 16] (Figure 1.3).

Orbitally speaking, for an elongated tetragonal distortion of the O_h symmetry the field is lowered along the z direction. The e_g and t_{2g} degeneracy is removed. d_{z^2} becomes more stable compared to $d_{x^2-z^2}$ since the trans ligands exert a more repulsive effect on the former, while d_{xz} and d_{yz} are stabilized relative to the d_{xy} orbital.

By taking this distortion to the limit by removing the ligands along the z axis completely, the orbital energy splitting is increased greatly. This is actually the configuration of a square planar complex.

In order to understand the relationship between these different selection rules, Table 1.2 details some values for the extinction coefficient (ϵ) depending on the band type. These values are approximate based on solution UV data and not on solid state examples. Nevertheless they can give a general idea for understanding transition metal pigments.

Other Geometries

Due to the relative rigidity of crystals and the close packing of atoms within them, transition metals in ceramic materials can exist in different coordination spheres. Hence,

five coordinate species are commonly found and can have two related geometries, square pyramidal or trigonal bipyramidal. Neither of these geometries have a symmetry centre. Transitions are therefore symmetry allowed.

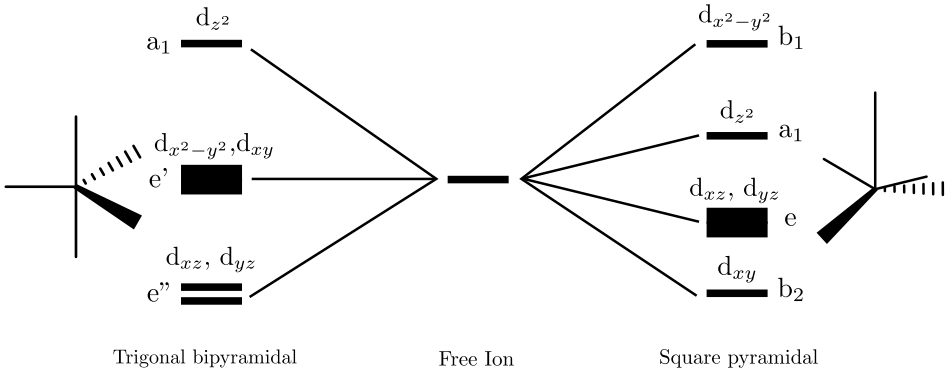

Figure 1.4: Orbital splitting for five-fold coordination geometries.

A typical orbital correlation diagram for these geometries is displayed in Figure 1.4. However, representing a lower symmetry compared to O_{h} or T_{d}, the energy levels of their orbitals are less definite and strongly dependent on spacial position of the ligands.

Careful tuning of the geometry of the metal centres coordination sphere was investigated for this study to obtain absorption in the desired area of the spectrum.

Charge Transfer

Covalent or non-polar character increases either with an increase in anion size or with an increase in anionic charge such as the replacement of an oxygen anion (O^{2-}) for a nitrogen anion (N^{3-}). With anions of greater charge or greater size the electrons are more loosely held thus making them more easily polarised by cations. Appreciable amounts of polarisation results in charge transfer bands [18]. These are intense absorption bands in the visible and ultra-violet regions of the spectrum. The absorption involves the promotion of a ground state electron from a localised orbital on one atom to an excited state energy level of a neighbouring atom.

Chromate pigments are an example of materials that involve charge transfer pro-

cesses [3]. The strong yellow colour arises from an electron being transferred from an oxygen atom to a chromium atom in a tetrahedral environment, which is known as ligand to metal charge transfer (LMCT). For this to occur the metal is usually in a high oxidation state and the ligand has a low ionisation energy.

Conversely metal to ligand charge transfer (MLCT) occurs in the red material tris(bipyridyl) iron (II) [17]. This transfer happens when the metal is in a low oxidation state and the ligand tends to have vacant $\pi^\star$ orbitals (π acceptor orbitals).

Mixed Valence Transitions

Compounds containing elements in more than one oxidation state are called mixed valence compounds. Many of them are coloured due to transitions between these two differing oxidation states. A good example is Prussian Blue $KFe[Fe(CN)_6]$ [19] which contains Fe in both 2+ and 3+ oxidation states. The iron(III) species is coordinated to the carbon atom of the CN ligand and the adjacent iron(II) species is linked to the nitrogen atom of the same ligand. This creates a three dimensional network of alternating FeC_6 and FeN_6 octahedra.

The colour arises from the transfer of an electron from a nearly localized donor site to an adjacent acceptor site, where both donor and acceptor metal ions possess more than one accessible oxidation state. Several factors affect this intervalence electron transfer notably the nature of the donor and acceptor metal ions and the bridging ligand. In the Prussian blue system, the delocalisation and mixing of the ground state and charge transfer state will therefore be much more favourable for a small energy differences between ground and excited state if the Fe(II) and Fe(III) sites are adjacent and are bridged by a covalent ligand (CN), giving this particularly vivid blue colour.

Band Theory

Band theory is derived from molecular orbital theory and is used to characterise the bonding and energy levels in an infinitely large molecule, *i.e.* a solid. It is useful to understand the broadening effect of energy levels into bands in a metal, semiconductor

and insulator.

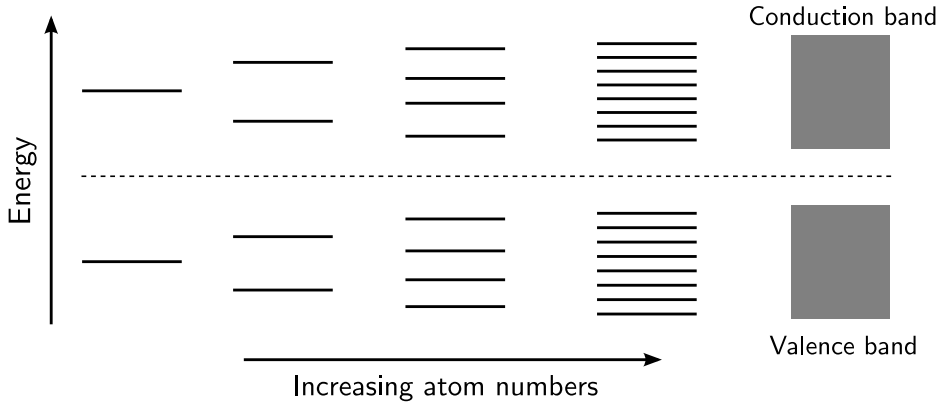

Figure 1.5: Formation of energy bands in a solid.

For an isolated atom, electrons occupy discrete energy levels. If another atom is close enough to the first, their outer electron clouds interact and the result is that the single energy level splits into two non-degenerate levels, one at higher energy than the other [20]. If the outer electron clouds of these two atoms interact with another two atoms, splitting occurs similarly. If, like in a crystal, the number of atoms is very large, the high energy levels come very close to each other. The same effect occurs for the low energy levels. Therefore they are considered as bands of energy, the lower energy band is called valence band and the higher energy band is called conduction band (Figure 1.5). These bands are filled the same way as the molecular orbitals, from the lowest energy to the highest.

The energy difference between these two bands of energy is very important since it characterises the energy necessary for an electron from the top of the filled valence band to be transferred to the bottom of the empty conduction band. It determines both the electronic and the absorption properties of the solid.

As mentioned previously, the energy difference *i.e.* the *band gap* determines the electronic properties of the solid.

In semiconductors, a narrow band gap separates the valence band from the conduction band. Which means, in contrast to metals (which have no band gap but a partially

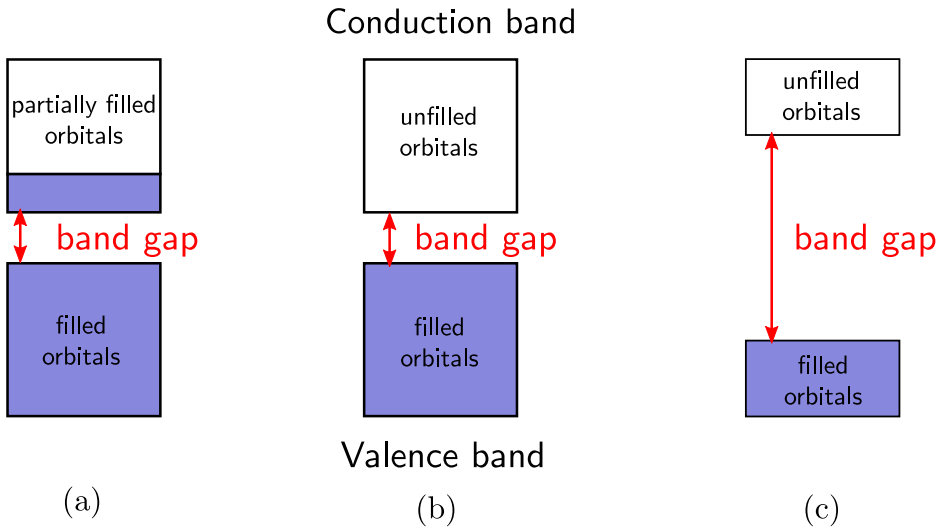

Figure 1.6: Schematic illustration of the energy bands in a metal (a), a semiconductor (b) and an insulator (c).

filled valence or conduction band and thus absorb all wavelengths, appearing metallic by consequence [21]), semiconductors have a wavelength threshold (Figure 1.6). Indeed, wavelengths not energetic enough to excite valence electrons will not be absorbed and the material will appear transparent to these wavelengths. Such an example is the white pigment TiO_2, which is an excellent insulator and has a large band gap (3 eV for rutile and 3.2 eV for anatase [22]). If the minimum energy is much smaller, lying in the infra-red region of the spectrum, the solid will absorb (and reflect) all of the visible spectrum and will appear metallic in nature, such is the case of graphite, which is semi-metallic and dark grey / black in colour and has a small band gap.

If we consider the electromagnetic spectrum, the minimum band gap for a solid to be transparent in the visible is 3.1 eV (400 nm). Since each semiconductor presents a different band gap, it should be possible to tune this band gap and then tune the wavelengths absorbed by mixing these semiconductors together.

Dopants and Impurities in Semiconductors

Impurities or dopants are foreign atoms present within a pure material. These dopants can be of two types. If they have more electrons than the atom they replace, then they contribute electrons to the conduction band and are called donors. If they have fewer electrons than the atoms they replace, they take up electrons from the valence band and are called acceptors [23].

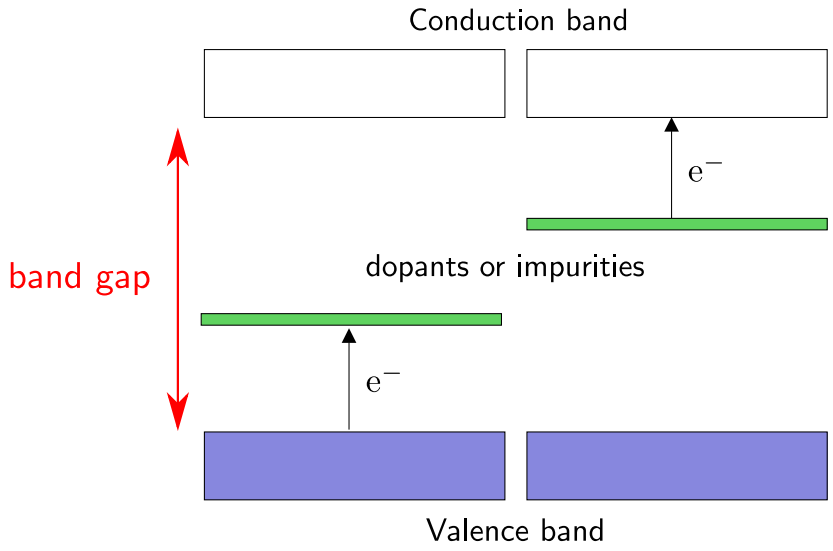

Figure 1.7: Schematic illustration of the energy bands of the discrete levels of energy provoked by dopants or impurities.

In both cases, the concentration of impurities is very low but they create discrete levels of energy close to the conduction band for donors and close to the valence band for acceptors (Figure 1.7). Since they are discrete levels, they contribute in absorption of light and could be used to select a certain range of wavelengths.

Colour

The band theory can be used to explain the colours of some pigments. For instance vermilion, manufactured from the mineral cinnabar or mercuric sulfide (HgS), has a band gap energy of $3.2x10^{-19}$J (2.0 eV). This corresponds to the red-orange end of the

visible region. Photons of a shorter wavelength than this, thus more energetic, will be absorbed.

Another example is cadmium yellow or cadmium sulfide (CdS). This pigment has a band gap of $4.16x10^{-19}$J (2.6 eV), which corresponds to the green-blue part of the visible spectrum. Photons of a lower energy, (red, orange, yellow and some green), will not be absorbed whilst the higher energy greens, blue, indigo and violet will be absorbed. The net result of this is that the material appears yellow.

1.2 Near-infrared Absorbers

Near-infrared absorber materials are materials which absorb wavelength from 750 nm to 1500 nm. In this field, literature data is limited and the principal contributors have mainly developed near-infrared absorbing organic compounds (*i.e.* azulenic chromophore [24] or phthalocyanine dyes [25]). However, the need for more robust pigments has driven some chemical companies (Merck, BASF) to actively investigate the field of inorganic pigments. Indeed, although organic pigments exhibit greater vividness and higher colour intensity as well as higher staining potential, their drawbacks are greater sensitivity to the action of chemical compounds, temperature and solvents.

Interesting applications for near-infrared absorbing pigments include optical recording, solar cells, laser filter and laser welding.

Laser Welding

Welding is the process of joining two materials by causing coalescence. The technique needs a high temperature collimated source to melt the materials at a precise position. In the automotive industry, lasers are often used to join multiple pieces of metal, as they provide a concentrated heat source, allowing for narrow, deep welds and high welding rates. Solid-state lasers are much easier to operate and are growing in popularity. However these lasers operate at wavelengths of the order of 1 μm which plastics and polymers are transparent to. Therefore additives which absorb in the near-infrared

are needed to join these materials.

The conventional additive is carbon black, impacting greatly on the colour property of the medium [26]. Some materials with strong absorption at the laser wavelengths, but little or no absorption at visible wavelengths have been developed. They allow a weld to be produced with little or no impact on the visual appearance of the part, giving designers flexibility in the choice of materials and colours. However these materials are organic dyes (*i.e.* metalloporphyrin and metalloazaporphyrin [27]) and can degrade rapidly through solar irradiation. Some of these compounds are found in medical devices *i.e.* bloodbags, and are often the reason for the blue tint of these devices.

Laser Marking

Laser marking is used in all sectors of industry where labelling is important. It is a way of permanently marking a physical item for tracking, either for security of quality control reasons and rather than using a vibrating or rotating tool to engrave a mark on the item, a high-powered laser is used.

The advantage of this technique is that while most forms of engraving result in a loss of some of the marked material, laser marking results in essentially no loss of material. Instead, the laser is used to create a shift in the colour of the material, creating a visible, virtually indestructible mark with minimal impact to the item.

The process is used on everything from identification badges to complimentary pens. Given its indelible nature, laser marking is an ideal choice for bar codes and other forms of inconspicuous tracking.

An added benefit of laser marking is environmental: with no inks or solvents used, the impact is very minimal. The other one is economic: laser marking is a fast process and since it is a non-contact method, wearing of the apparatus is minimal.

There are three main results of conventional laser marking, depending on the material affected and the laser used to mark the item. Charring occurs when the absorbed energy heats up the surrounding material enough to create a slight degradation, re-

sulting in a black mark. Foaming occurs in the case of plastic marking when the surrounding temperature is raised enough to cause the polymers to degrade to gases, forming small bubbles. Ablation occurs when the material becomes extremely hot and the plastic degrades completely, leaving a clean depression.

In the case of laser marking the incorporation of a colourless pigment with near-infrared absorption properties gives a double benefit, the same laser can be used for any colour or mixture of colours of the substrate and the substrate colour is not altered.

An example of such a near-infrared absorbing pigment is the nanoparticulate multilayer oxides (indium tin oxide or antimony tin oxide) coated on mica [28]. However this pigment tends to tint the substrate slightly yellow.

Clear Solar Control Glazing

The sun's radiation emission is like a blackbody of 5800 K. About half of this radiation lies in the visible region of the electromagnetic spectrum, the other half is concentrated in the near-infrared to infrared region (Figure 1.8). However, most of the heat that the sunlight carries is due to radiation in this latter region.

It is beneficial for a building to allow daylight to enter, and therefore architects design buildings with large windows [29]. However, in warmer climate zones, these windows increase the amount of near-infrared radiation getting into the building, which then requires intensive use of air conditioning. This way of cooling is costly and not environmentally friendly.

Pigments for the creation of windows which transmit visible radiation but block the near-infrared are therefore of great interest for solar control glazing. The established approach to the manufacture of this type of glazing is the use of multilayered thin films of metal oxide-silver layers sandwiched between insulating layers (*i.e.* $WO_3/Ag/WO_3$ transparent heat mirrors [30]). The high cost of this technique is the main drawback. NIR blocking is also possible through use of tinting materials such as iron silicate and oxides or lanthanum hexaboride [31] in the glass itself, but the impact on the colour of the glass in the visible region is too unfavourable for a beneficial absorption in the

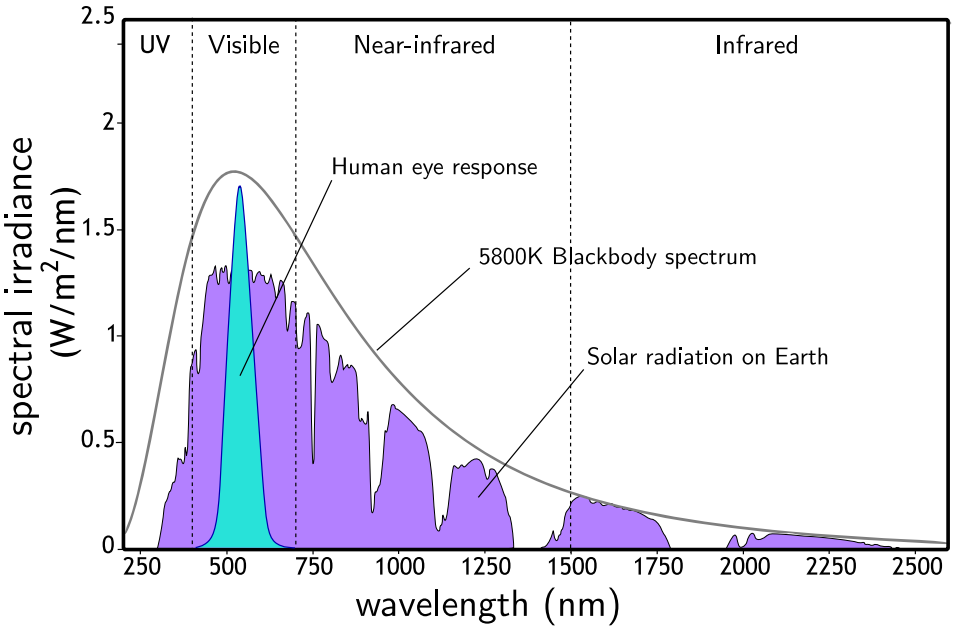

Figure 1.8: Electromagnetic spectrum adjacent to the visible region showing the human eye response to light and the solar spectrum.

NIR. Organic dyes and pigments have been incorporated into polymers (*i.e.* dithiolene metal complex [32]), but due to their organic nature they tend to be highly sensitized by solar irradiance and are not suitable for long term application.

A suitable material to be used for this solar heat control would be a colourless/transparent inorganic pigment with NIR absorption properties.

1.3 Candidate Materials

Phosphates and Silicates

The chemistry of phosphates and silicates is very similar and both of the systems form structures closely related [33]. Both form compounds with anionic entities of one XO_4 (X = Si, P) tetrahedron or as a result of condensation of several XO_4 groups sharing one, two or three oxygens [34]. This particularity allows an infinite number of geometries and ring, chain ions and layers of linked XO_4 tetrahedra can be formed.

Both families form very stable compounds and many natural minerals are based on these tetrahedral units (*e.g.* olivine, $(Mg,Fe)_2SiO_4$ or hydroxyapatite, $Ca_5(PO_4)_2(OH)$ [35]). They are non-toxic which makes them attractive for environmentally viable pigments. However, phosphates are easier to make as generally speaking they require a lower synthesis temperatures than silicates.

At elevated temperatures phosphates tend to condense and form linear linkages of corner sharing PO_4 tetrahedra generally known as *polyphosphates* with general formula $[P_nO_{3n+1}]^{(n+2)-}$. Thus phosphates are a structurally versatile family of compounds which offer the possibility to create different coordination spheres for incorporated cations in order to tune their absorption properties. Most of the transition metal phosphates are coloured through *d* - *d* transitions, exemplified by commercial manganese violet ($MnNH_4P_2O_7$ [36]). The anionic behaviour of the phosphates is beneficial as anticorrosive paint as well. Zinc phosphate pigments such as $Zn_3(PO_4)_2.4H_2O$ replace efficiently the toxic zinc chromate and red lead as non-polluting pigments for paint [37].

Within the family of phosphates, the diphosphates are especially suitable for creating near-infrared absorbing pigments as they exhibit structures with either five-fold coordinated oxygen cavities or octahedrally shaped cavities for the cations. Such coordinations are very interesting for fine tuning of colour properties by incorporating different cations. Also, as the diphosphate structures do not have 3-dimensional connectivity of the phosphate groups they are not very rigid and tolerate large non-

stoichiometric behaviour, *e.g.* cation mixture, by relaxing the local geometry. Here one remarkable structure is to be mentioned for the divalent-cation diphosphates. Indeed most of the $M_2^{II}P_2O_7$ compounds have a polymorph with an atomic arrangement closely related to *thortveitite*, $Sc_2Si_2O_7$, a disilicate [38].

The *Thortveitite* structure is monoclinic, $C2/m$, with Z=2 and unit-cell dimensions $a = 6.56$ Å, $b = 8.58$ Å, $c = 4.74$ Å and $\beta = 103.13°$. In this arrangement the linked oxygen atom of the Si_2O_7 group is located on an inversion centre with an unusual value for the Si–O–Si angle of 180°. This confers to the disilicate group a high internal symmetry since the silicon atoms and one oxygen atom are located on a mirror plane. Figure 1.9 is a projection along the c axis and shows the layers formed by the disilicate group, the scandium atoms have distorted octahedral oxygen coordination.

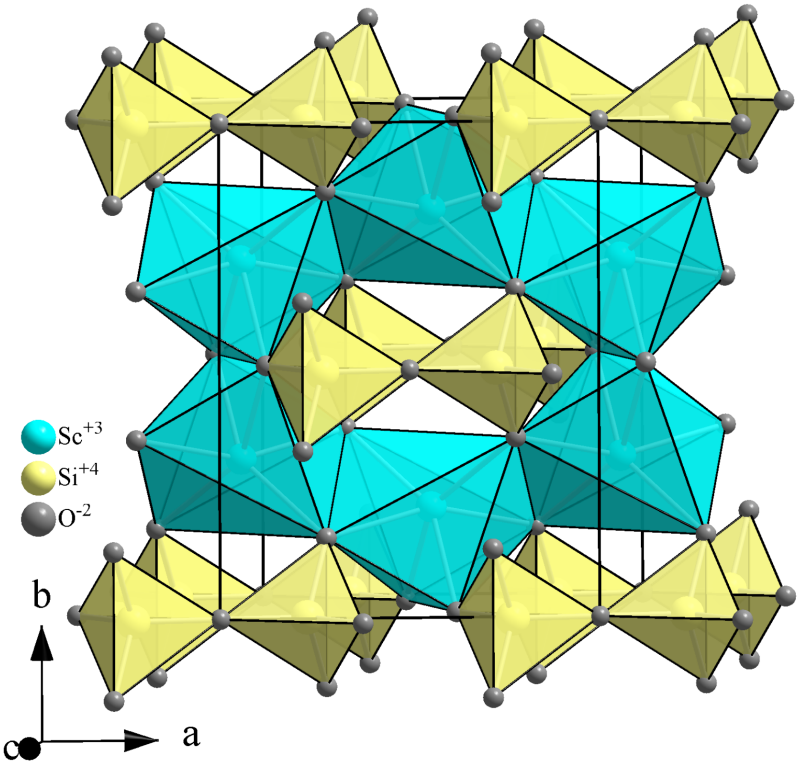

Figure 1.9: Projection along the c axis of the *thortveitite* structure. The Si_2O_7 group is shown as yellow tetrahedra and octahedral arrangement around the Sc atom is shown in cyan.

These properties and the fact that diphosphates are chemically and thermally stable make pigments deriving from them particularly interesting in the development of weather durable pigments.

Copper(II)

Copper is commonly found in +2 oxidation state which confers a d^9 configuration for the Cu^{2+} ion. This configuration gives rise to a single free-ion term ^2D. This is particularly relevant to this work since it produces in the octahedral geometry an uncomplicated spectra with a single absorption band resulting from the $^2T_{2g} \leftarrow {}^2E_g$ electronic transition due to its single lone electron and therefore more prone to be shifted out of the visible, in the near-infrared by a weak ligand. Also, the *Jahn Teller* effect is strong for this configuration; one lone electron occupies the d_{z^2} orbital while all the other levels are occupied by pairs of electrons. This renders the degenerate e_g level very unstable, resulting in a split between the half occupied d_{z^2} and the fully occupied $d_{x^2-y^2}$ orbitals.

Cu^{2+} is therefore found in both tetragonally distorted octahedral geometry (where axial bonds are elongated with regard to the equatorial bonds) and elongated square pyramidal geometry (where the weaker apical bond is longer than the four equatorial bonds).

Iron(II)

This transition metal is the second most abundant metal, which makes it cheap and readily available [39]. It is non-toxic as well.

Its main oxidation states are +3 and +2, however for this particular study, iron(II) is more interesting. Indeed, iron(II) is a d^6 ion and can be either high-spin or low-spin. The high-spin free ion iron(II) has a ^5D ground term which splits in octahedral complex into a ground $^5T_{2g}$ and an excited ^5E_g term [35]. This configuration is similar to the Cu(II) ion and a *Jahn Teller* effect often broadens the single transition band found between 900 and 1000 nm, at the start of the near-infrared region.

1.4 Aims of the Thesis

Pigments have been widely developed for their colour and are present in a large variety of industrial applications. On the other hand, industries have only been recently interested in functional pigments; transparent inorganic pigments are virtually non-existent.

As for today, the modern market is focused on organic pigments. However their thermal, chemical and solar instability restricts their usage to short term applications and prevents the use in ceramic glazes and thermoplastics. The inorganic alternatives are not entirely colourless and alter the colour of substrate. Specialized inorganic pigments would therefore be the perfect choice.

The aim of this study is to discover a promising candidate for a functional transparent near-infrared absorber. Identification of suitable phases makes use of techniques such as powder X-ray diffraction, powder neutron diffraction, EXAFS, electron microscopy and UV/Visible/NIR spectroscopy. *Chapter 3* describes the preliminary work conducted to determine the route to follow, *Chapter 4* details some simple copper phosphates and describe their absorption mechanism, *Chapter 5* focuses on di-cation diphosphate with separated sites to accommodate the cations while *Chapter 6* investigates a particular mixed di-cation diphosphate and aim to understand the relationship between both metals in the shared site and the effect to the absorption in the near-infrared; Impact of the temperature of synthesis on the size of particles is also studied for this system. *Chapter 7* investigates an iron phosphate candidate and *Chapter 8* considers a copper silicate system. The results of this study are summarised in *Chapter 9*.

CHAPTER 2

EXPERIMENTAL TECHNIQUES

2.1 Introduction

The work described in this thesis is solely concerned with the synthesis and characterisation of materials in the solid state. More specifically, the synthetic techniques used produced polycrystalline materials, *i.e.* crystalline powders. The most important and useful characterisation technique for samples of this nature is powder X-ray diffraction (PXD). This non-destructive technique allows a fast initial phase identification and detailed structural characterisation, if necessary, on a routine basis. Another non-destructive method used for characterisation of some of the samples is powder neutron diffraction (PND). This technique is particularly adapted to obtain accurate oxygen positions. In parallel, one of the chemical compound series studied was analysed by extended X-ray absorption fine structure spectroscopy (EXAFS) in order to determine with precision the coordination spheres of the metal atoms. For the purpose of this work *i.e.* to determine the optical characteristics of the samples, the absorption properties in the visible to near-infrared regions of the electromagnetic spectrum have been investigated for each sample.

This chapter provides a summary of these experimental techniques, the background theory and their applications.

2.2 Synthetic Methods

2.2.1 High Temperature Solid State Reaction

The most widely used method for the preparation of polycrystalline solids is the direct reaction of a mixture of solid starting materials. Since both thermodynamic and kinetic factors are important for these kind of reactions [40], a suitable temperature has to be adopted to produce the desired phase at an acceptable reaction rate. Therefore, synthesis temperatures for the chemical systems investigated in this work are usually between 1000 and 1500 °C. The need for such a high temperature may be explained by the nature of the reactants, which are solid materials, and the structural reorganisation involved in the formation of the product; these higher temperatures increase greatly the ion diffusion, the main rate limiting step in the reaction.

A typical procedure for direct solid state reaction employs stoichiometric mixtures of solid starting materials, mainly finely ground oxides (but also carbonates or other oxo-salts can be used) to enhance reaction rates by maximising the surface area; these salts decompose in-situ into high surface area oxides. Mixing of the reactants is accomplished with an agate pestle and mortar; regrinding and/or pelletisation of the mixture can accelerate the rate of reaction by increasing the interfacial contact of the reacting species. The starting materials are then placed into a crucible to avoid contamination of the sample and fired at the desired temperature. A very common crucible material is high density alumina, but if the container is not chemically inert to the reactants, platinum or gold may be used. Controlling the atmosphere of a reaction can be crucial for adjustment of oxidation states of the metals present. It may be necessary to keep the reaction under oxygen, nitrogen, argon or hydrogen gas. Finally, the reaction is monitored at various stage by X-ray diffraction, an easy non-destructive technique to routinely check the formation of the targeted phase.

This solid state reaction method can also be called the ceramic method.

2.2.2 Sol-Gel Reaction

The sol-gel technique involves the production of ceramic materials by the preparation of a solution, gelation of the solution, then removal of the solvent [41].

Inorganic or organic precursors (*e.g.* nitrates or alkoxides) of metals are dissolved in a solvent to form a suspension in which gravitational forces are negligible and molecular species can exist in isolation. A gel forms when the sol is heated slowly to form macroscopic species as the solvent evaporates. The transformation from amorphous gel to crystalline solid occurs upon firing at higher temperatures (as with the ceramic method above).

Sol-gel based processes can aid the production of homogenous, pure materials at lower temperatures than with the ceramic method and, sometimes, the formation of new materials that cannot otherwise be made. This is due to several factors; as the starting materials are dissolved in solvents, atomic level mixing occurs; this in turn means that lower reaction temperatures may be used which can result in the stabilisation of low-temperature phases and often results in smaller particle sizes as well. However, sol-gel syntheses can be long and costly processes and at times retained precursors and/or by-products can pollute the final product.

2.3 Powder X-ray Diffraction (PXD)

2.3.1 Diffraction

When a wave encounters an obstacle, it is scattered in different directions. Diffraction is the interference of these secondary waves and addition of these waves gives rise to a series of maxima and minima which can be interpreted as diffraction patterns. X-ray radiation, being an electromagnetic radiation can be scattered by electrons of atoms in materials and diffraction can occur under certain circumstances.

In 1912, *Max von Laue* identified that atom spacings in crystals are of the same order of magnitude as the wavelength of X-ray radiation (*ca.* 10^{-10} m), thus crystals can act as three dimensional diffraction gratings for X-rays. Later that same year, with his assistants *Walter Friedrich* and *Paul Knipping*, he exposed a copper sulphate crystal to a beam of X-rays and recorded its diffraction on a photographic plate [42]. X-ray diffraction was born and is now the main tool for the study of crystalline structures.

2.3.2 X-ray Radiation

X-rays have a wavelength in the range of 10 to 0.01 nanometers and are usually produced by bombarding a metal target with high energy electrons. The incoming electrons colliding with the metal have sufficient energy to ionize some inner orbital electrons. The vacant inner orbital holes are immediately filled with electrons from an outer orbital. The energy released in the transition appears as X-ray photons.

2.3.3 X-ray Diffraction Theory

If one considers a scattering situation, in which a plane wave is incident on two parallel lattice planes, separated by a perpendicular distance d (Figure 2.1), for constructive interference the path difference between the two diffracted beams must correspond to an integral number of wavelengths. Simple trigonometry yields the *Bragg* equation (Equation (2.1)) [43].

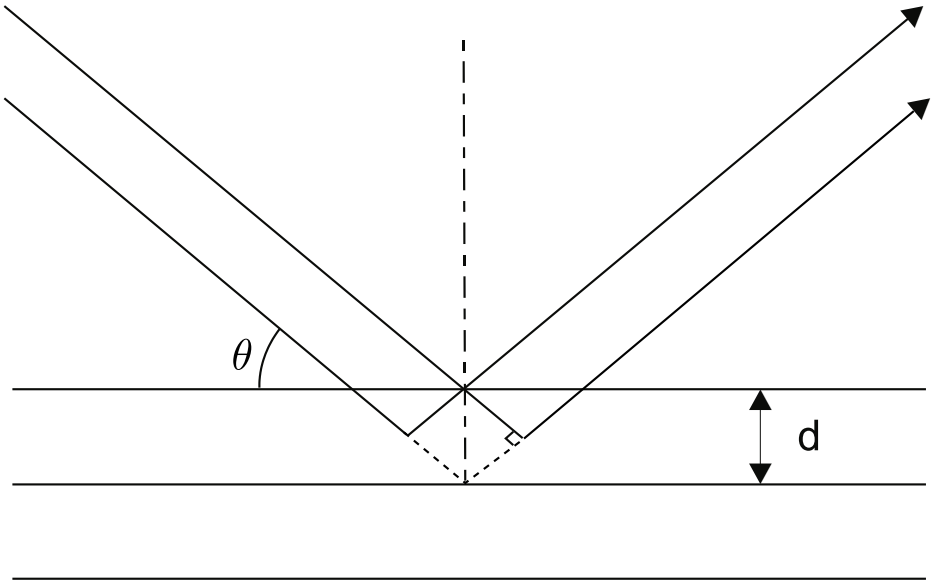

Figure 2.1: Schematic representation of diffraction from parallel lattice planes, dashed line represents the path difference.

$$n\lambda = 2d \sin\theta \tag{2.1}$$

where n is an integer, $1, 2, 3, \ldots$

λ is the wavelength of the incident X-rays,

d is the separation of lattice planes ('d-spacing'),

θ is the incident angle of the X-rays.

The angle θ is known as the *Bragg* angle. At angles other than the *Bragg* angle, the diffracted beams are out of phase and interfere destructively. The interplanar separations, d, in the crystal are calculated by measuring the diffraction maxima given by each set of planes. It is customary, however, to use the first order diffraction maxima $(n = 1)$ to determine the interplanar separation from the *Bragg's Law* to keep it simple. The crystal system can then be derived from these d values by identification of the planes involved. Planes are defined by their *Miller* indices, hkl, which are the reciprocal of the fractions of the positions where the plane intercepts the a, b and c axes

Table 2.1: Expressions for d-spacings in the different crystal systems in terms of lattice parameters a, b and c and *Miller* indices h, k and l [44]

Crystal System	Expression for d_{hkl}
cubic	$\frac{1}{d_{hkl}^2} = \frac{h^2+k^2+l^2}{a^2}$
tetragonal	$\frac{1}{d_{hkl}^2} = \frac{h^2+k^2}{a^2} + \frac{l^2}{c^2}$
orthorhombic	$\frac{1}{d_{hkl}^2} = \frac{h^2}{a^2} + \frac{k^2}{b^2} + \frac{l^2}{c^2}$
hexagonal	$\frac{1}{d_{hkl}^2} = \frac{4}{3}\left(\frac{h^2+hk+k^2}{a^2}\right) + \frac{l^2}{c^2}$
monoclinic	$\frac{1}{d_{hkl}^2} = \frac{1}{\sin^2\beta}\left(\frac{h^2}{a^2} + \frac{k^2\sin^2\beta}{b^2} + \frac{l^2}{c^2} - \frac{2hl\cos\beta}{ac}\right)$
triclinic	complex expression

respectively (Table 2.1).

In theory a crystal should display diffraction from each of its lattice planes giving rise to an observed maxima in the diffraction pattern. However, intensity is not always observed from every plane due to the existence of special reflection conditions or systematic absences. These result from symmetry elements of the structure and are *e.g.* determined by lattice types such as body centred (I) and face centred (F), as well as space group symmetry elements such as glide planes and screw axes [45, 46].

2.3.4 Powder X-ray Diffraction

The method developed by *Laue* and used extensively for characterisation of materials requires X-rays to be scattered by a single crystal. Unfortunately, most of the materials prepared by solid state chemistry are polycrystalline.

The principle of powder method is based on a monochromatic beam of X-rays which strikes a pollycrystalline sample containing, as the name suggests, a multitude of very small crystals randomly arranged in every possible orientation; the various lattice planes are therefore present in every possible orientation. The incident beam will be

scattered in every directions by these small crystals, however, many of these will be correctly inclined to satisfy the *Bragg*'s Law; thus, each lattice spacing in the crystal will give rise to a cone of diffraction which can then be detected by either a detector surrounding the sample or a movable detector. Each cone of diffraction intensity consists of a set of closely spaced dots, each one of which represents diffraction from a single crystallite within the powder sample. With a very large number of crystallites, these dots join together to form the diffraction cone.

It is therefore important to shine the X-ray beam on a sample with a statistically distributed orientation of the crystallites in order to observe all diffraction maxima showing their typical intensities. This is achieved by grinding the sample thoroughly prior to analysis.

2.3.5 Instrumentation

All powder X-ray diffraction patterns obtained during this work were collected on three machines: a Siemens D5000, a Bruker D8 and a Panalytical X'Pert PRO MPD. Both Siemens and Bruker diffractometers (Figure 2.2), use monochromatic copper $K_{\alpha 1}$ radiation ($\lambda = 1.5406$ Å) acquired by the use of a fine focus X-ray tube with a copper target coupled with a germanium single crystal monochromator. The monochromatic beam is then collimated through an aperture diaphragm and directed onto the sample which is previously mounted on a flat plastic or aluminium sample holder. The diffracted X-rays are detected by a standard scintillation counter. The sample is tilted at a constant angular velocity. The detector is correspondingly moved around the sample at precisely double the angular velocity ensuring that at all times the diffraction angle (2θ) is twice the glancing angle (θ). The incident beam, sample and detector are arranged according to *Bragg Brentano* geometry. Although using the same principle, the Panalytical diffractometer use both copper $K_{\alpha 1}$ and $K_{\alpha 2}$ radiations.

The data were collected and manipulated using a personal computer. Initial characterisation of the samples was performed by recording PXD patterns, typically over the 2θ range 10 - 80° with a step size of 0.02° for 30 minutes. These measurements were

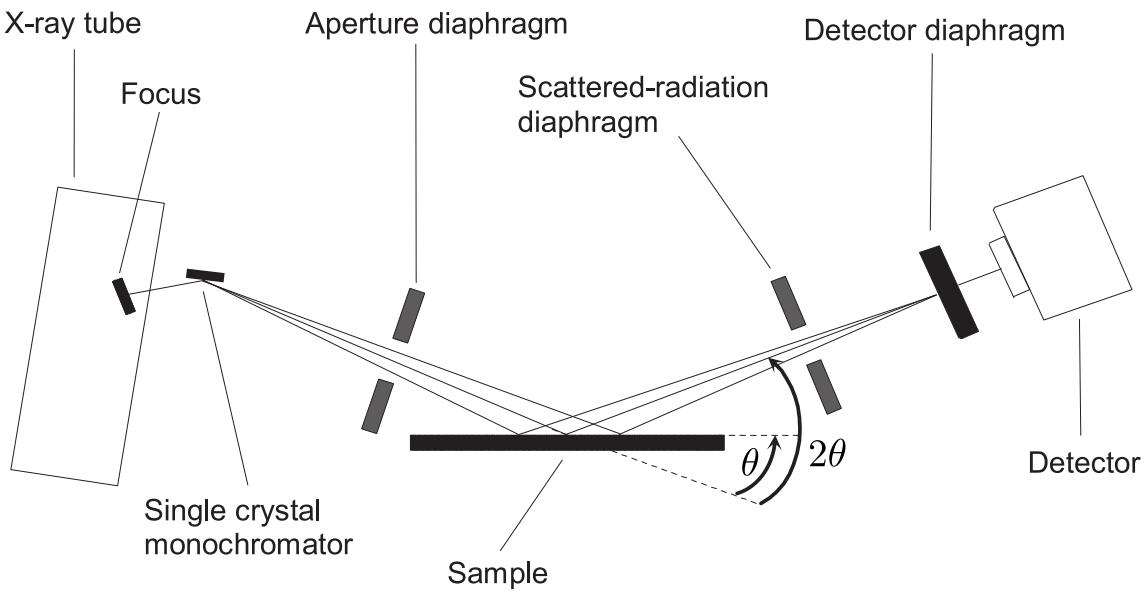

Figure 2.2: Schematic diagram of the powder X-ray diffractometers (D5000 and D8) where the lines represent the path of the X-ray beam

used for phase identification and indexing performed using the Diffrac^{plus} evaluation program (*EVA*) [47] and CELREF software [48] respectively.

To obtain more accurate values for lattice parameters, slower scans over wider 2θ ranges (typically 10 - 110°) were used. Further structural analysis from these data sets involved using the *Rietveld* method.

2.4 Powder Neutron Diffraction (PND)

2.4.1 Theory

Neutron diffraction was first performed in 1936 after the motion of neutrons was described in terms of wave mechanics [49].

The utility of neutron diffraction techniques compared to X-ray diffraction, is mainly due to the difference in the way these radiations are scattered. In X-ray diffraction, X-rays are scattered by the electrons surrounding the nucleus and the scattering power is a function of atomic number which makes this technique inefficient for identification of adjacent elements in the periodic table or light elements like oxygen, lithium or hydrogen in the presence of heavy metals. On the other hand, neutrons are scattered by nuclei and the scattering power is both related to potential scattering and resonance scattering. The fact that it is not directly related to atomic number, allows for some lighter elements to be more accurately positioned in the lattice and adjacent elements to be distinguished on mixed crystallographic sites. This is particularly important in this work since for some samples both zinc and copper are present.

Powder neutron diffraction techniques use two principal types of neutron radiation, a white beam (for time of flight) and constant wavelength. Only the latter has been used during this work and will be discussed here.

2.4.2 Instrumentation

In this work, data was collected on the high-resolution instruments D1A (Figure 2.3) and D2B at the high flux reactor Institut Laue Langevin (ILL) in Grenoble. Both instruments use a fixed neutron radiation wavelength; thus the diffraction principle is the same as previously discussed for PXD in subsection 2.3.3 with θ and d varying in the *Bragg* equation (Equation (2.1)).

D2B has incident white neutrons collimated and monochromated from a 300 mm to a 50 mm beam width with a take off angle of 135° using a germanium monochromator,

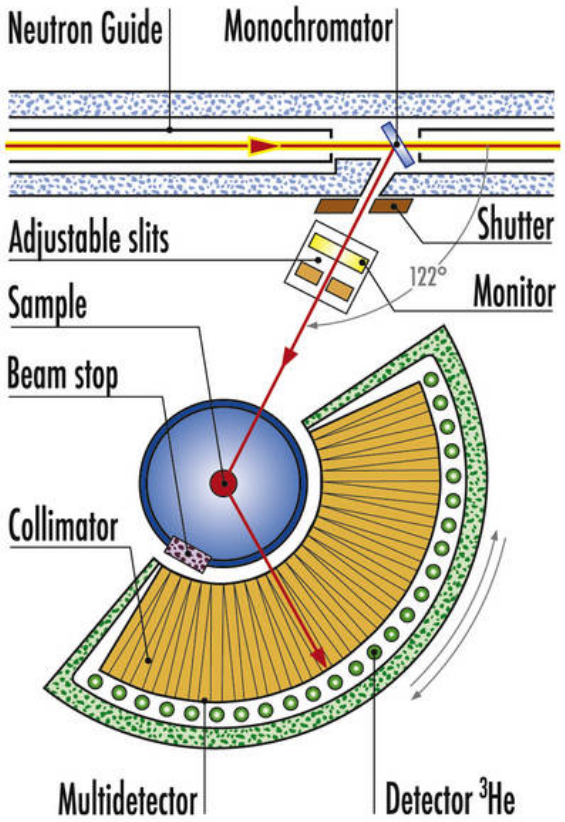

Figure 2.3: Powder neutron diffraction instrument: Schematic of D1A [50].

giving a resolution of $\Delta d/d \approx 5 \times 10^{-4}$. D1A has a lower resolution ($\Delta d/d \approx 2 \times 10^{-3}$) and a beam height of 150 mm. Samples run on these instruments were mounted in vanadium cans of 7 or 10 mm diameter, and the scattered neutrons were detected. D2B utilises a bank of 128 three inch collimators and ^{3}He counters at 2.5° intervals which sweep from 0-160° in 0.025° steps. A range of wavelengths are accessible, but the optimum wavelength of $\lambda = 1.594$ Å was used for this work. D1A is rather similar but employs a 60° bank of ^{3}He detectors (which sweep in 0.05° steps) and a longer wavelength of 1.909 Å. Data collections on both instruments were performed at room temperature over periods of 6-8 hours per sample.

2.5 Structural Refinement

2.5.1 Overview of the Structure

In order to characterise the prepared samples by identifying the chemical phases they contain, the patterns collected were compared against databases of reference materials, specifically the *Powder Diffraction File* distributed by the Joint Committee on Powder Diffraction Standards (JCPDS) [51], and the Inorganic Crystal Structure Database (ICSD).

Once the phases had been carefully identified, the first parameter which was examined was the unit cell. The unit cell of a crystal is the smallest imaginary parallel-sided region from which the entire crystal can be built up by translation. It is described by the lattice parameters a, b and c for the edge lengths and α, β and γ for the angles between the faces [17].

In this work, the determination of this first characteristic of each sample was done with CELREF [48], a refinement program for diffraction patterns which uses an iterative least square refinement method, the equation of which is shown below ((2.2)):

$$M = \sum_i W_i (\sin^2_i \theta^{obs} - \sin^2_i \theta^{calc})^2 \tag{2.2}$$

where W_i is a weighting factor,

M is a weighted minimised difference for observed 2θ data.

The raw data file is read and reflection peaks are selected for refinement against theoretical values for the reflections that are based upon the lattice parameters and space group obtained from a model found in the literature. This is a useful tool for confirming quickly if this is the expected phase, but for a complete structural refinement which takes into account any impurities it is necessary to do a full *Rietveld* refinement.

2.5.2 *Rietveld* Refinement

A powder diffraction pattern obtained from a crystalline material can be thought of as an array of individual reflection profiles where each one has a peak height, a peak position, a peak width, a peak shape and an integrated area proportional to the *Bragg* intensity, I_k, where k represents the *Miller* indices h, k and l [44]. The *Rietveld* method [52, 53] is a technique which was devised to utilise the full information content at each step of the powder pattern, and allowed structure determination using a method of profile refinement.

The procedure compares an experimental diffraction pattern with a theoretical model by refining and varying a number of structural / positional parameters *e.g.* lattice parameters, atomic co-ordinates, site occupancies *etc*. and also profile parameters *e.g.* peak shape, asymmetry, instrumental factors such as the diffractometer zero point *etc*. A least squares refinement is carried out to minimise the difference between the observed data and calculated profile and hence to obtain the best fit between the entire observed pattern and the entire calculated pattern based on simultaneously refined models for the structural and profile parameters.

In this thesis, complete structural refinements were performed using the computer package *General Structure Analysis System* (GSAS) built by *von Dreele* and *Larson* [54] using the EXPGUI suite [55].

2.5.3 Theoretical Considerations

For any regular array of stationary atoms, the structure factor F, is the sum of the contributions of the amplitude f and the phases ϕ of each atom [53], leading to this expression (Equation 2.3):

$$F = \sum_{j=1}^{N} f_j \exp[i\phi_j] \tag{2.3}$$

The total phase shift of an atom, j, in a unit cell at a point (x_j, y_j, z_j) from the origin, is the sum of the phase shifts in each direction. When the phase shift is evaluated, the

structure factor for one unit cell becomes (Equation 2.4):

$$F_{hkl} = \sum_{j=1}^{N} f_j \exp\left[2\pi i(hx_j + ky_j + lz_j)\right] \tag{2.4}$$

where h, k and l represent *Miller* indices defining the plane from which the reflection occurs.

For very small crystals, the intensity of the scattered beam can be considered proportional to the square of the structure factor (Equation 2.5):

$$I_{hkl} = kL^2|F_{hkl}|^2 \tag{2.5}$$

where k is the scaling constant,

L is the *Lorentz* factor, a geometric function related to the method of data collection and hence the instrument used.

In real crystals, the scattered intensity is modified by imperfections in the lattice structure. Defects and substitutional disorder cause local structural irregularities, particularly in non-stoichiometric materials. In addition, thermal motion causes a reduction in scattered intensity as a result of time dependent vibrations of the atoms about their mean positions, disrupting the in-plane behaviour of their combined scattering. The correction to a structure factor reflected by a plane, hkl, takes the form [56] (Equation 2.6):

$$T_{hkl} = \exp\left[-B_{hkl}\frac{\sin^2\theta}{\lambda^2}\right] \tag{2.6}$$

where T_{hkl} is the thermal motion correction and

B is equal to $8\pi^2U$, where U is the root mean square thermal displacement.

So for a unit cell, the structure factor becomes (Equation 2.7):

$$F_{hkl} = \sum_{j=1}^{N} f_j n_j \exp\left[-B_{hkl}\frac{\sin^2\theta}{\lambda^2}\right] \exp\left[2\pi i(hx_j + ky_j + lz_j)\right] \tag{2.7}$$

where n_j is the occupation factor of the j^{th} atom, equal to one in a structure free from defects.

However, it assumes that the displacements due to thermal motion are isotropic, which is rarely the case, except in some highly symmetric special positions of the cubic space groups. A more rigorous analysis [52] describes the anisotropy of thermal motion in the form of an ellipsoid, replacing the equation (2.7) by the following (Equation 2.8):

$$\begin{aligned} T_{hkl} = \exp\big[-1/4\,\big(&B_{11}h^2a^{*2} + B_{22}k^2b^{*2} + B_{33}l^2c^{*2} + 2B_{12}hka^*b^* \\ &+ 2B_{23}klb^*c^* + 2B_{13}hla^*c^*\big)\big] \end{aligned} \tag{2.8}$$

The intensity of the scattered beam is also dependent on the multiplicity of the particular hkl reflection. Therefore, for a specific hkl reflection at a particular point in a given crystal symmetry class, there can be a number of equivalent planes diffracting at the same angle to give an increased intensity.

2.5.4 Structure Refinement

The *Rietveld* method is known to be an invaluable tool for the structural analysis of the major classes of crystalline materials which cannot be synthesised as single crystals. There are a multitude of refinable parameters available while doing a refinement although many are not necessary for common refinement. The procedure described below references the most important variables that can be refined during a structure refinement using powder diffraction data.

- Determination of an approximate model of the structure, including unit cell,

space group and atomic positions by comparison with other known structures and their diffraction patterns.

- Refinement of the overall scale factor and background parameters.
- Refinement of the lattice parameters, zero point error and possible sample displacement correction in order to accurately locate the *Bragg* reflections. At this stage a preliminary refinement of the peak shape parameters is usually carried out.
- Location of accurate atom positions in the structure by allowing the fractional coordinates x, y and z to vary. This alters the peak intensities and allows the improvement of the peak shape.
- Variation of fractional occupancies yields information as to the distribution of each atom on shared crystallogaphic sites.
- Refinement of the isotropic temperature factors to define thermal motion of atoms.
- Full refinement of the peak shape parameters, in addition to any asymmetry or prefered orientation parameters which might be necessary.
- Anisotropic temperature factors should be refined if possible; this can lead to significant improvement of the fit, but typically it is not often possible with powder diffraction data.

The *Rietveld* refinement method was used for structural refinement using both PXD and PND data. Despite the fact that the radiation was different while collecting data, the refinement method is the same; in all cases the *best fit* sought is the best least squares fit to all the intensities at each step. The quantity minimised in the least squares refinement is the function M and is summed over all the data points (Equation 2.9):

$$M = \sum_i w_i \left(y_i^{obs} - y_i^{calc} \right)^2 \tag{2.9}$$

where w_i is a weighting factor given by $1/y_i^{obs}$,

y_i^{obs} is the observed intensity at point i ($2\theta_i$ for PXD),

y_i^{calc} is the calculated intensity point i.

The calculated intensities y_i^{calc} are determined from the structural model by summing the calculated contributions from neighbouring *Bragg* reflection (k) plus the background b_i (Equation 2.10):

$$y_i^{calc} = s \sum_k L_k |F_k|^2 \phi \left(2\theta_i - 2\theta_k\right) P_k A + y_{b_i} \tag{2.10}$$

where s is the scale factor,

L_k contains *Lorentz* polarisation and multiplicity factors,

ϕ is the reflection profile function,

F_k is the structure factor for the k^{th} *Bragg* reflection,

P_k is the preferred orientation function,

A is an absorption factor,

y_{b_i} is the background intensity at the i^{th} step.

Preferred orientation is due to the ordering of crystallites in one direction or set of directions. It results essentially in systematic distortions of the reflection intensities toward certain planes. Mathematical corrections can be made for this phenomenon and it is defined by the expression (Equation 2.11):

$$P_k = \left[G_2 + (1 - G_2) \exp\left(-G_1 \alpha_k^2\right)\right] \tag{2.11}$$

where G_1 and G_2 are refinable parameters and α_k is the angle between the presumed cylindrical symmetry axis and the preferred orientation axis direction.

The background intensity at $2\theta_i$ is obtained from a specified refinable background function, $[b_i]$ (Equation 2.12):

$$y_{b_i} = \sum_{m=0}^{5} B_m \left(\frac{2\theta_i}{BKPOS} - 1 \right)^m \tag{2.12}$$

where BKPOS is the background position that is user-specified in the input control file.

This simple approach was replaced by more sophisticated expressions such as cosine fourier series as the *Rietveld* methodology progressed, leading to a much more accurate fit for the background profile.

Since a comparison of intensities is performed at every point, it is essential for the construction of the calculated profile to accurately describe the shape of the *Bragg* reflections, *i.e.* peak shape. Peak shape is generally dictated by the instrument; for the Siemens D5000 and the Bruker D8, the peak shape is the pseudo-Voigt function which is a linear approximation to the convolution of the Gaussian and the Lorentzian components of the peaks and can be described by the function (Equation 2.13):

$$P_{\text{pseudo-Voigt}} = \eta L + (1 - \eta) G \tag{2.13}$$

where L and G are the Lorentzian and Gaussian contributions to the peak shape and η is the mixing parameter which can be refined as a linear function of 2θ (Equation 2.14):

$$\eta = N_A + N_B(2\theta) \tag{2.14}$$

where N_A and N_B are refinable parameters.

The Gaussian (G) and Lorentzian (L) contributions to the peak shape are represented by the equations (2.15) and (2.16):

$$G = \frac{(4 \ln 2)^{1/2}}{H_k \sqrt{\pi}} \exp\left(-4 \ln 2 \left(2\theta_i - 2\theta_k \right)^2 / H_k^2 \right) \tag{2.15}$$

and

$$L = \frac{2}{\pi H_k} 1 / \left[1 + 4 \frac{(2\theta_i - 2\theta_k)^2}{H_k^2} \right] \tag{2.16}$$

where $2\theta_k$ is the calculated position for the k^{th} *Bragg* peak corrected for the counter zero point,

H_k is the full-width-at-half-maximum (FWHM) of the k^{th} *Bragg* reflection.

As shown above, the FWHM, H_k of a Gaussian peak varies with the scattering angle θ_k [57] in a way accurately represented by the empirical expression (Equation 2.17):

$$H_k^2 = U\tan^2\theta_k + V\tan\theta_k + W \tag{2.17}$$

where U, V and W are refinement parameters and are all instrument and sample dependent. This formula takes into account the peak broadening resulting from the particle-size effect.

The Lorentzian expression is given as (Equation 2.18):

$$H_k = X\tan\theta_k + \frac{Y}{\cos\theta_k} \tag{2.18}$$

where the first term is associated with microscopic strain broadening and the second accounts for particle size broadening.

At low scattering angles, the detector and sample height can introduce some peak shape asymmetry resulting in a shift of the peak maximum to lower angles whilst the integrated peak area remains unchanged. This is corrected by the following semi-empirical correction factor (Equation 2.19):

$$k' = 1 - sP\frac{(2\theta_i - 2\theta_k)^2}{\tan\theta_k} \tag{2.19}$$

where P is the asymmetry parameter,

$s = +1, 0, -1$ when $(2\theta_i - 2\theta_k)^2$ is positive, zero or negative.

In the *Rietveld* method, for each least squares refinement, the least squares parameters fall into two distinct groups. The first group defines the profile parameters which represent the position, shape and FWHM of the peaks and consists of the unit cell pa-

rameters, U, V, W, zero point, asymmetry and preferred orientation correction. The second group defines both structural and thermal parameters, including the profile scale factor, the temperature factors, the coordinates and fractional occupancies for each atom.

2.5.5 Criteria of Fit

While using the GSAS program, one has to be careful not to be fooled by a local minimum (rather than a global minimum) which leads to false structural refinement. In order to follow the progress of the refinement, there are some criteria of fit, known as reliability factors (R-factors) which help to make a quantitative assessment of the agreement between observed and calculated profiles. These are defined as $R_{profile}$, $R_{expected}$ and $R_{weighted\ profile}$. The equation for the R_p and R_{exp} are given as (Equations (2.20) and (2.21)):

$$R_{profile} = R_p = 100 \left[\frac{\sum_i \left| y_i^{obs} - y_i^{calc} \right|}{\sum_i y_i^{obs}} \right] \tag{2.20}$$

$$R_{expected} = R_{exp} = 100 \left[\frac{(N - P + C)}{\sum_i w_i \left(y_i^{obs} \right)^2} \right]^{\frac{1}{2}} \tag{2.21}$$

where R_{exp} is defined by the statistics of the refinement,

N is the number of observations,

P is the number of refinable parameters,

C is the number of constraints.

But from a mathematical point, $R_{weighted\ profile}$ is the one which reflects the most the progress of the refinement, because the numerator is the residual being minimised (Equation 2.22):

$$R_{weighted\ profile} = R_{wp} = 100 \left[\frac{\sum_i w_i \left[y_i^{obs} - y_i^{cal} \right]^2}{\sum_i w_i \left[y_i^{obs} \right]^2} \right]^{\frac{1}{2}} \tag{2.22}$$

Finally, R_{exp} and R_{wp} can be expressed as a single criterion, chi-squared (χ^2) as (Equation 2.24):

$$\chi^2 = \left[\frac{1}{N - P + C}\right]^2 \sum_i w_i \left[y_i^{obs} - y_i^{cal}\right]^2 \tag{2.23}$$

$$= \left[\frac{R_{wp}}{R_{exp}}\right]^2 \tag{2.24}$$

which is the natural measure of the fit and is normally minimised in the refinement. For a good fit, the value of R_{wp} must approach the R_{exp} value, *i.e.* χ^2 should approach unity. The quality of fit can also be estimated visually by examining a plot of the profile fit; for a good fit the difference line between calculated and observed pattern should be as flat as possible with fluctuations consistent with noise.

2.6 UV Visible Near-Infrared Spectroscopy

UV Visible Near-infrared spectroscopy (UV/Vis/NIR) is a technique which involves the use of photons in the ranges adjacent to and including visible. In this region of the electromagnetic spectrum (150 nm to 3000 nm), molecules undergo electronic transitions.

2.6.1 Transmission Mode

This technique when used in transmission mode, is particularly useful for determination of the quantity of transition metal ions or conjugated organic compounds present in solution. It is basically the application of the *Beer-Lambert* law which states that the absorbance of a solution is directly proportional to the concentration of the absorbing species in the solution and the path length (Equation 2.25):

$$A = -\lg(\frac{I}{I_0}) = \epsilon c L \tag{2.25}$$

where A is the absorption,

I_0 is the intensity of the incident light at a given wavelength,

I is the transmitted intensity,

ϵ is the molar absorptivity,

c is the concentration of the absorbing species,

L is the pathlength through the sample.

2.6.2 Diffuse Reflectance Mode

For a solid sample, the transmission mode is impractical. The *Kubelka-Munk* theory allows the use of the diffuse reflectance mode to collect structural information on the absorbing species.

Kubelka-Munk Theory

In this theory, *Kubelka* and *Munk* define two constants, the absorption coefficient K and the scattering coefficient S to describe the optical properties of a film that absorbs and scatters light [58, 59].

Considering a layer on a substrate, when an incident beam hits the surface, two beams result, one is the diffuse incident light going through the layer, the other one is the light scattered by the layer and travelling away from the layer. However each beam is attenuated by absorption and scattering losses and reinforced by scattering losses of the respective opposite beam. These losses are determined quantitatively by two linked differential equations as followed (Equation 2.26):

$$\frac{di}{dx} = -(K+S)i + Sj \frac{dj}{dx} = (K+S)j - Sj \tag{2.26}$$

Integrating these equations for an infinitely thick opaque film gives the *Kubelka-Munk* function (Equation 2.27):

$$R_\infty = 1 + \frac{K}{S} - \sqrt{\left(1+\frac{K}{S}\right)^2 - 1} \tag{2.27}$$

where R_∞ is the reflectance for an infinite layer,

K is the absoption coefficient,

S is the scattering coefficient.

From this *Kubelka-Munk* function and within the range of validity of the theory, the reflectance, depends only upon the ratio of the absorption to scattering coefficients and not on their individual values.

By collecting the diffuse reflectance, the scattering part is lost and the reflectance is directly proportional to the absorbance.

2.6.3 Instrumentation

UV-Visible-NIR spectroscopy was performed using a Perkin Elmer UV/Vis/NIR lambda 19 spectrometer set up in diffuse reflectance mode (Figure 2.4). Spectra were collected in the range of 200 to 2500 nm.

Two sources are used to provide the desired wavelengths. A deuterium lamp covers the UV range and a halogen lamp covers the Vis to NIR range. This radiation is collimated by aperture slits onto a UV/Vis or NIR grating which disperses and selects a segment of the spectrum, sending it through the exit slit. This slit restricts the spectrum segment to a near monochromatic beam, which will hit the sample mounted between a quartz window and a plastic sample holder. The diffuse reflectance is then reflected by the integrating sphere onto the detector (photomultiplier for UV/Vis range or PbS detector for NIR range).

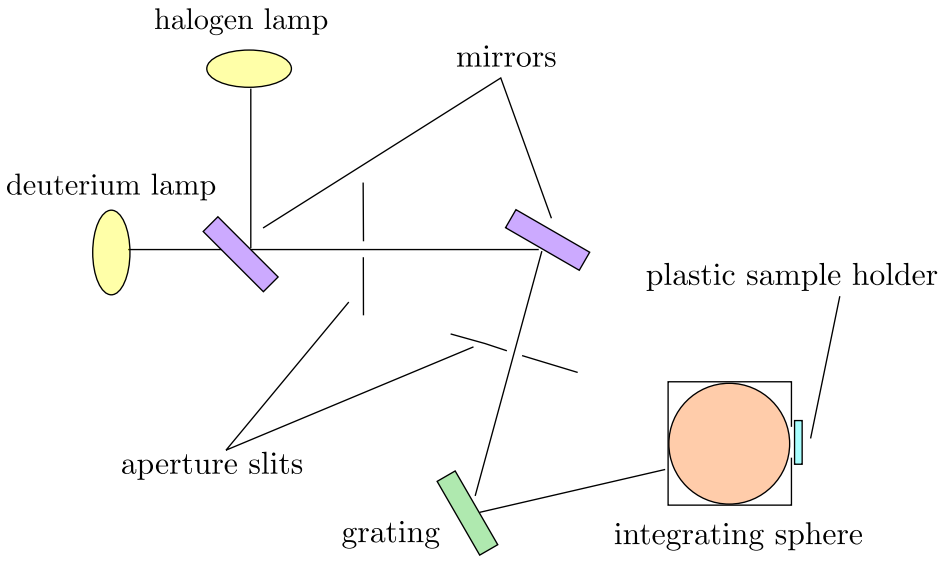

Figure 2.4: Optical path of Lambda 19 spectrophotometer.

A barium sulphate plate was used as a reference to obtain a background correction before commencing data collection.

2.7 Electron Microscopy

Electron microscopy has several applications, which can be divided into imaging, compositional analysis (via Energy Dispersive X-ray Spectroscopy (EDX)) and electron diffraction. The imaging facility was used in this work to examine the particle size of samples synthesised by different processes. EDX was used for semi-quantitative elemental analysis on various samples.

Electron optics are similar to light optics since electrons can be considered as both particles and waves. In terms of radiation, visible light has a wavelength of 380 - 780 nm while electron radiation has a wavelength of between 0.001 and 0.01 nm. Electrons are generated from thermionic emission and then accelerated through a potential in order to obtain a monochromatic beam [60]. This alters the wavelength of the electron beam according to the following equation (Equation 2.28):

$$\lambda = \left[\frac{1.5}{(V + 10^{-6}V^2)}\right]^{\frac{1}{2}} \tag{2.28}$$

where λ is the wavelength in nm,

V is the potential difference.

2.7.1 Electron Sample Interaction

Types of Interactions

When interacting with a sample, electrons can either be elastically or inelastically scattered.

- *Elastic scattering* is a process which leaves the energy of the primary electron unchanged.
- *Inelastic scattering* refers to any process which lead to a loss of a detectable amount of energy from the primary electron. This is employed in the generation of X-rays and secondary electrons used in imaging and elemental analysis.

Types of Electrons

Immediately after the electron-sample interaction, three types of electrons can be released as a result:

- *Secondary electrons*: They escape from the sample with energies below *ca.* 50 eV. These electrons are used in Scanning Electron Microscopy (SEM) imaging as they are abundantly produced.
- *Backscattered electrons*: These are primary electrons leaving the surface before having lost all their energy. Mainly used for imaging, but can be used for diffraction.
- *Auger electrons*: These originate from the expulsion of an excited electron due to the absorption of energy from the primary electron beam by an atom. This atom releases energy in the form of characteristic X-ray radiation or specific electron called Auger electron. Both emissions being distinctive for a particular atomic species, they are usually used for quantitative elemental analysis.

2.7.2 Scanning Electron Microscopy Imaging Experiments

In this work, Scanning Electron Microscopy (SEM) has been performed using a JEOL JSM-5910 machine. The microscope (Figure 2.5) consists of an electron gun which produces an electron beam from a heated tungsten filament (*ca.* 2800 K). The electrons are accelerated to an energy of 0.3 to 30 keV and travel through an evacuated optical path (*ca.* pressure $< 10^{-10}$ Pa) since electrons are strongly scattered by gases.

Along this optical path the beam is focused through pairs of electromagnetic condenser lenses and objective lenses which control subsequently the convergence angle and the diameter of the beam (typically 3.0 nm at 30 keV). Finally, scan coils are used to scan the collimated beam in a raster fashion over a rectangular area of the sample surface; the size of the area determines the magnification. The detector then monitors emission of secondary electrons or backscattered electrons to form the final image on screen.

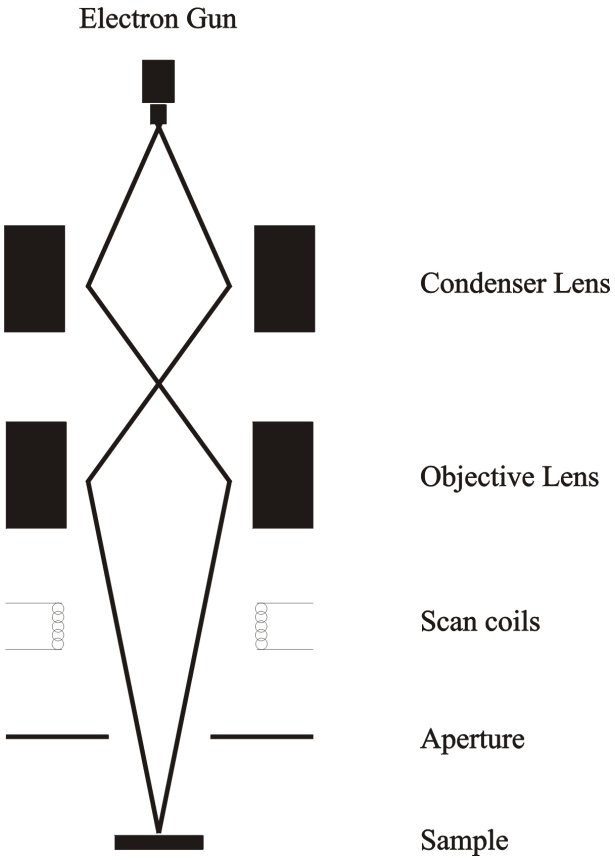

Figure 2.5: Schematic diagram of a scanning electron microscope. The solid lines represent the path of the electron beam.

2.7.3 Energy Dispersive X-ray Spectroscopy (EDX)

EDX is an analytical technique employed for elemental analysis. This technique relies on the analysis of emitted X-rays from a sample being hit with charged particles; bearing in mind that each element emits characteristic X-ray radiation, each peak can be attributed to a certain element.

This technique is usually seen in conjunction with SEM imaging. Indeed, the same electron beam source is necessary in both imaging and elemental analysis, the difference being the detector. In this work, this is a lithium-drifted silicon detector. When an X-ray strikes the detector, a number of electrons are excited to the conductance band of the silicon, generating electron-hole pairs. The electrons and holes are attracted to opposite ends of the detector due to a strong electric field. The size of the current pulse

thus generated depends on the number of electron-hole pairs created, which in turn depends on the energy of the incoming X-rays.

There are some limitations to EDX. Firstly, elements lighter than sodium are difficult to detect accurately enough for quantification with a standard detector. Secondly, the energy resolution of the detector is poor. Each X-ray line is not seen as a sharp line but as a broad peak, making it difficult to resolve closely-spaced lines. Finally, spurious peaks in the spectrum may be produced as the result of two identical photons arriving at the detector simultaneously. A detector will interpret this as a single photon of twice the energy and will produce what is known as a *sum peak*.

2.8 Extended X-ray Absorption Fine Structure Spectroscopy (EXAFS)

The X-ray absorption fine structure is the modulation of the X-ray absorption coefficient at energies near and above the core-level binding energies of an atom. It is thus very useful for investigation of the local environment of a specific element which could otherwise be impossible to separate from other atoms by conventional analytical methods. This technique is especially sensitive to the formal oxidation state, coordination chemistry, and the distances, coordination number and species of the atoms surrounding the selected element.

The advantage of this technique is that it can be used on nearly any kind of material, from biological to inorganic, from crystalline to amorphous and even in solution, and since X-rays are fairly penetrating, trace elements can also be studied. The measurement is straightforward but the main drawback is the necessity of an intense and energy-tunable source of X-ray radiation, like a synchrotron source, due to the weakness of this phenomenon.

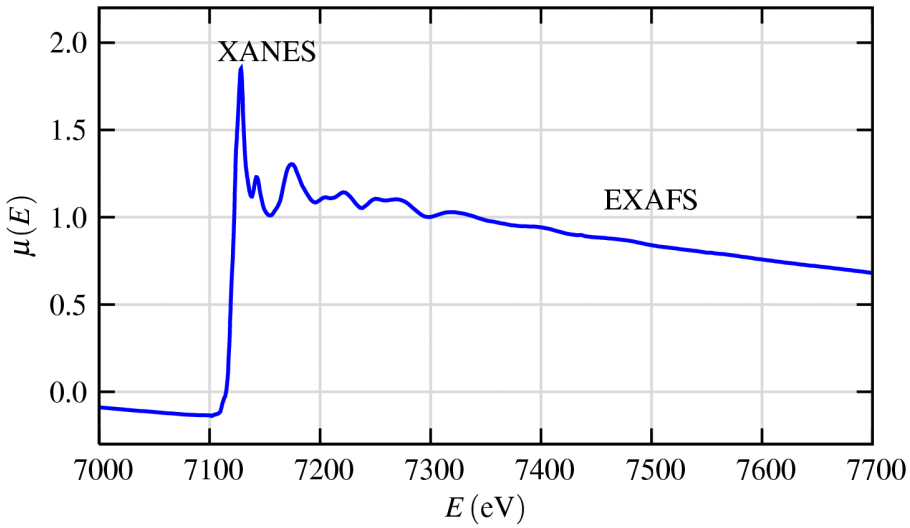

Figure 2.6: Typical X-ray absorption spectrum [61].

The X-ray absorption spectrum can be broken in two parts (Figure 2.6), X-ray absorption near-edge spectroscopy, known as XANES and the extended X-ray absorption fine-structure spectroscopy (EXAFS). It is more a convention than a physical separation, since both have the same origin; but XANES is more sensitive to formal oxidation state and coordination chemistry while EXAFS can describe the distances, coordination number and species of the neighbours of the absorbing atom.

When an X-ray beam travels through matter, it is absorbed due to the *photo-electric effect*. This is in fact the result of an interaction between the X-ray photon and an electron in a quantum core level of an atom (Figure 2.7).

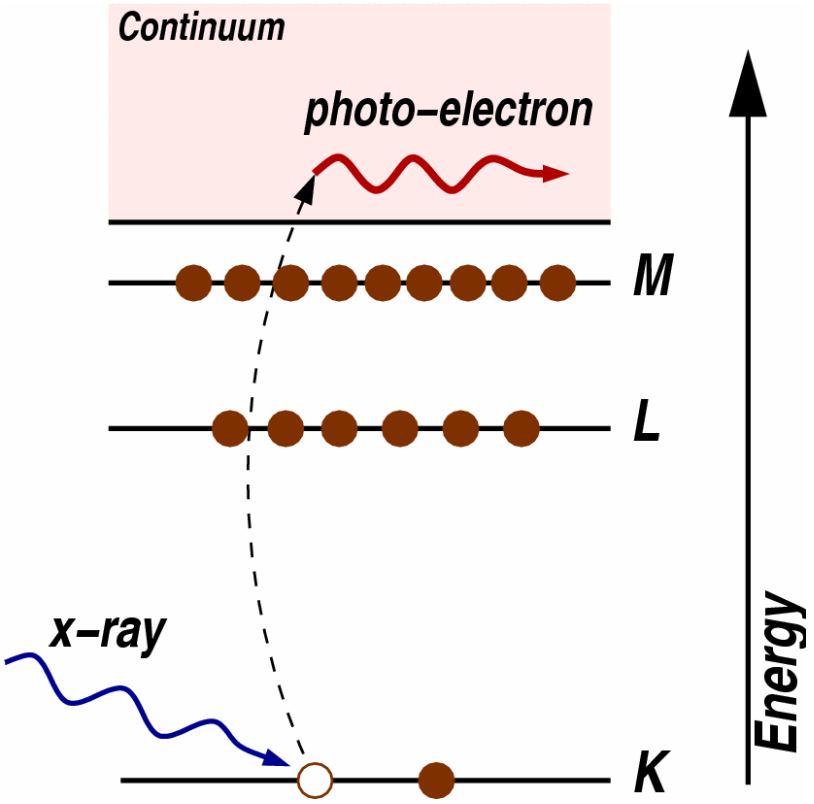

Figure 2.7: Photo-electric effect representation [61].

For a particular electron to be excited, the incident energy of the X-ray has to be greater than the binding energy, but due to the nature of X-ray, it is strongly dependent on the atomic number Z as suggested by this equation (Equation 2.29):

$$\mu = \frac{\rho Z^4}{A E^3} \tag{2.29}$$

where μ is the absorption coefficient,

ρ is the sample density,

Z is the atomic number of the absorber,

A is the atomic mass of the absorber,

E is the X-ray energy.

When the incident X-ray energy matches the binding energy of a core level electron, the absorption rises greatly; it is called the *absorption edge*. EXAFS is the measure of variation of the absorption coefficient μ in function of the energy, just above this edge. Since every atom has core-level electrons with well defined binding energies, it allows this technique to be element specific.

2.8.1 Theory

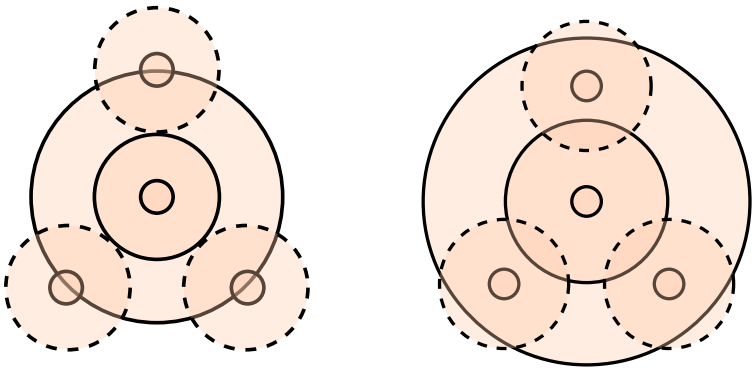

(a) *(b)*

Figure 2.8: Schematic representation of a constructive interference *(a)* and a destructive interference *(b)* between outgoing and backscattered waves.

Once the X-ray quantum is absorbed, a photo-electron with wave-number k is released. As this excited atom has neighbouring atoms, the photo-electron, which can be seen as an outgoing spherical wave, can scatter from the electrons of neighbouring

atoms which will produce a backscattered wave. Outgoing and backscattered waves can interfere and these interferences will vary between constructive (Figure 2.8, (a)) and destructive (Figure 2.8, (b)) [62].

It is these interferences which can be seen as oscillation in the EXAFS part of the XAFS spectrum. Quantum mechanically, the photo-electron wavenumber is expressed as (Equations (2.30) and (2.31)):

$$k = \sqrt{\frac{2m(E - E_0)}{\hbar^2}} \tag{2.30}$$

where k is the wavenumber of the photo-electron,

m is electron mass,

E is the x-ray energy,

E_0 is the absorption edge energy,

$\hbar$ is Plank's constant.

and

$$\lambda = \frac{2\pi}{k} \tag{2.31}$$

In a nutshell, since the path lengths of both outgoing and backscattered waves define the nature of these intereferences, it implies that the oscillation pattern is dependent of the distance to the neighbouring atoms. The EXAFS can thus be defined as a function $\chi(E)$ (Equation 2.32):

$$\chi(E) = \frac{\mu(E) - \mu_0(E)}{\Delta\mu_0(E_0)} \tag{2.32}$$

where $\mu(E)$ is the observed absorption coefficient for a photon energy E,

$\mu_0(E)$ is the smooth *bare atom* background,

$\Delta\mu_0(E_0)$ is the edge step.

For practical purposes, $\chi(E)$ is plotted as $\chi(k)$ instead. Since the oscillations decrease rapidly with k, the EXAFS is often weighted by k^2 or k^3 to amplify the oscillation at high k prior to any Fourier transformation.

The Fourier transform is a powerful tool for the interpretation of EXAFS. By changing the oscillation into the interatomic distance between the absorber and the scatterer (R-space), it gives clear indication about the different coordination spheres around the absorbing atom. Broad peaks visibly correspond to the shell of backscattering atoms, but there is no direct quantification possible since a scattering phase-shift of 0.5 Å is usually present.

To obtain quantitative information, a theoretical model is used to fit the experimental data. Many models have been developed for the EXAFS but the simplest theory is the plane wave theory of Lee and Pendry [63] (Equation 2.33):

$$\chi(k) = \sum_{j=1}^{\text{shells}} \frac{N_j}{kR_j^2} S_0^2 F_j(k) \exp -2k^2\sigma_j^2 \exp \frac{-2R_j}{\lambda k} \sin\left(2kR_j + 2\phi_{abs}(k) + \phi_{scat}(k)\right) \quad (2.33)$$

where N_j is the number of equivalent backscatterers in each shell,

S_0^2 is an amplitude reduction factor accounting the absorber multi-excitations,

$F_j(k)$ is the element specific backscattering amplitude,

R_j is the interatomic distance between the absorber and the scatterer,

σ_j^2 is the mean square variation of R_j,

λ is the mean-free path,

$\phi_{abs}(k)$ is the phase shift from the absorber,

$\phi_{scat}(k)$ is the phase shift from the scatterer.

This model assumes that the outgoing spherical wave can be treated as a plane wave. This approximation considers the backscattering atom to be small compared to the interatomic distance, which is true for most materials.

Another assumption which is made is that all backscattering pathways are independent and do not interfere with others. In the EXAFS region, this can be assumed since only a few percent of the total scattering is due to multiple scattering.

2.8.2 Instrumentation

The EXAFS spectra were collected on Station 7.1 (Figure 2.9) in transmission mode at Daresbury Laboratory SRS (Synchrotron Radiation Source). The X-ray radiation used at Station 7.1 is produced by excited electrons accelerated to the near speed of light and injected into a storage ring which holds the energy close to 2 GeV with powerful bending magnets. The electrons whilst cycling, lose some energy tangentially to their path, as synchrotron radiation. Ports are disposed around the storage ring and direct this radiation along beamlines to the experimental stations. Each station is specifically arranged to use a defined range of energy.

The X-ray beam is monochromated by a harmonic rejecting double crystal Si(111) monochromator in the range of 4 keV to 10 keV.

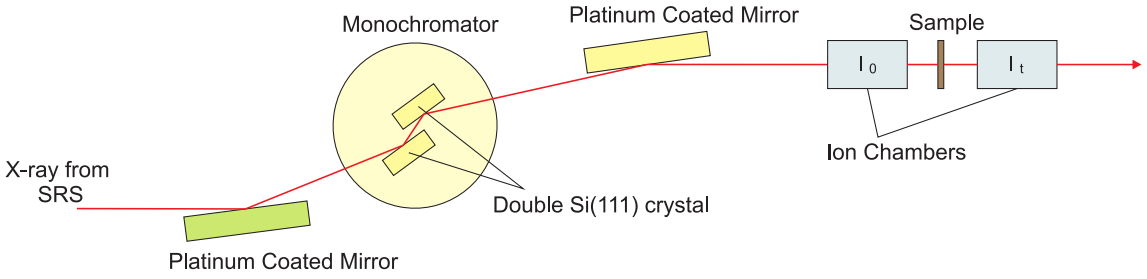

Figure 2.9: Schematic representation of XAFS station 7.1 at Daresbury Laboratory SRS

Sample Preparation

The samples studied were diluted with an X-ray non-absorbing material, polyvinyl acetate (PVA), in the ratio of 10% by weight, specific to the element of which the K-edge was to be considered. The prepared disc is mounted between the two ion chambers (Figure 2.9) and then data was collected over the XAFS range for each sample and each target element. Eight scans per sample were performed in order to reduce the signal to noise ratio.

2.8.3 Data Analysis

Data analysis of EXAFS is a two step process:

- *Background substraction*: It is necessary to separate the XANES part of the spectrum from the EXAFS and remove any absorption due to the machine or other elements present. In this work, PAXAS [64] is the program of choice. It removed any artefacts and converts the data from absorption versus monochromator angle (millidegree) to absorption versus energy (eV) using the relevant monochromator d-spacing.

- *EXAFS refinement*: In order to describe the environment of a specific element, fitting of the experimental absorption to a theoretical model is required. It has been achieved through EXCURV98 [65].

EXCURV98 program uses the phase shifts, the type and number of atoms, the distance from absorbing nucleus and thermal motion parameters to generate a theoretical absorption spectrum. These parameters are subsequently varied in a least square refinement process to minimise the following equation and subsequently fit the experimental absorption (Equation 2.34):

$$FI = \sum_{i} \left[k_i^3 \left(\chi_i^T(k) - \chi_i^E(k) \right) \right]^2 \tag{2.34}$$

where $\chi_i^T(k)$ and $\chi_i^E(k)$ are theoretical and experimental EXAFS respectively,

FI (Fit Index) is the weighted minimised sum for the theoretical and experimental EXAFS.

The criteria of fit to ascertain that the correct global minimum is used, is described as followed (Equation 2.35):

$$R = \frac{\int \left| \chi^T(k) - \chi^E(k) \right| k^3 \, dk}{\int |\chi^E(k)| \, k^3 \, dk} \times 100 \tag{2.35}$$

CHAPTER 3

PRELIMINARY WORK

3.1 Introduction

The mechanism of light absorption is a very well understood topic in chemistry, as seen in Chapter 1. However it is a vast subject and many possible solutions are conceivable to accomplish the goal of this thesis. Some previous successfull studies about transparent conducting oxides such as tin doped indium oxide [66] and thermochromic thin films such as tungsten doped vanadium oxide [67], showed a few examples exhibiting absorption in the near-infrared region of the electromagnetic spectrum and relatively light colour; therefore as a starting point, this specific route was investigated.

As the aim of the preliminary study was to determine possible candidates for further investigation, a lot of effort was directed to produce a large pool of samples. The synthesised samples were characterised using powder X-ray diffraction in order to identify the produced phases by comparison with the structure database implemented in the software EVA [47]. In order to assess the suitability of the compounds for the thesis project their absorption properties were evaluated by UV to near-infrared spectroscopy.

The most significant results were obtained while doping semi-conducting metal oxides with copper, and therefore these samples are discussed in this chapter.

3.2 Synthesis and analysis

Samples were prepared by mixing MO (M = Mg, Zn) with different amounts of CuO in order to achieve molar metal atom fractions of the doping element between 1 and 5%. The mixtures were ground using a pestle and mortar then pressed into a pellet and heated up to 1000 °C in a box furnace for 24 hours. The light coloured materials obtained were then removed from the furnace, left to cool down to room temperature in the air and ground to a fine powder for further analysis.

For every sample, powder X-ray diffraction data was collected and compared with the parent samples, MgO and ZnO respectively, using the software EVA to detect if copper was incorporated in the structure. This was done by looking for extra peaks due to the CuO phase. Lattice parameters were obtained using the CELREF program as described in Chapter 2. While ionic radii of the involved metal ions are quite similar (Cu^{2+} 0.73 Å, Mg^{2+} 0.72 Å and Zn^{2+} 0.74 Å [68]), a systematic change along the a axis can be seen for both doped system proving that copper has been perfectly introduce into the lattice (Tables 3.1 and 3.2).

Table 3.1: Unit cell parameters of copper doped magnesium oxide (e.s.d.s given in parenthesis).

Space group $Fm\bar{3}m$.

Compounds	a / Å
MgO undoped	4.2210(2)
MgO:Cu doped 1 at%	4.2215(2)
MgO:Cu doped 3 at%	4.2220(5)
MgO:Cu doped 5 at%	4.2241(3)

Table 3.2: Unit cell parameters of copper doped zinc oxide (e.s.d.s given in parenthesis).

Space group $P6_3mc$.

Compounds	a / Å	c / Å
ZnO undoped	3.2430(3)	5.1977(4)
ZnO:Cu doped 1 at%	3.2437(2)	5.1978(3)
ZnO:Cu doped 3 at%	3.2439(5)	5.1978(3)
ZnO:Cu doped 5 at%	3.2442(4)	5.1979(2)

UV to near-infrared absorption data (200 to 2500 nm range) were collected on undiluted samples according to the method outlined in Chapter 2. The spectra of the samples with 3 at% Cu are compared in Figure 3.1.

For both samples, the absorption spectra show an absorption edge in the UV to the blue region of the visible, depending on the parent oxide. Also both spectra include a second absorption band in the red region of the visible to the near-infrared. However, the position and intensity of this second absorption band is rather different. Despite the very small quantity of copper introduced into the structure, this absorption band is assumed to be induced by a *d* - *d* transition.

3.3 Results and discussion

3.3.1 Copper doped magnesium oxide

For copper doped magnesium oxide, MgO crystallises in the rocksalt structure type (like NaCl), with the space group being the cubic $Fm\bar{3}m$. Copper oxide is known to occur within the same cubic structure under certain circumstances [69]. In this type of structure, the metal atoms are present in a perfectly octahedral surrounding (Fig-

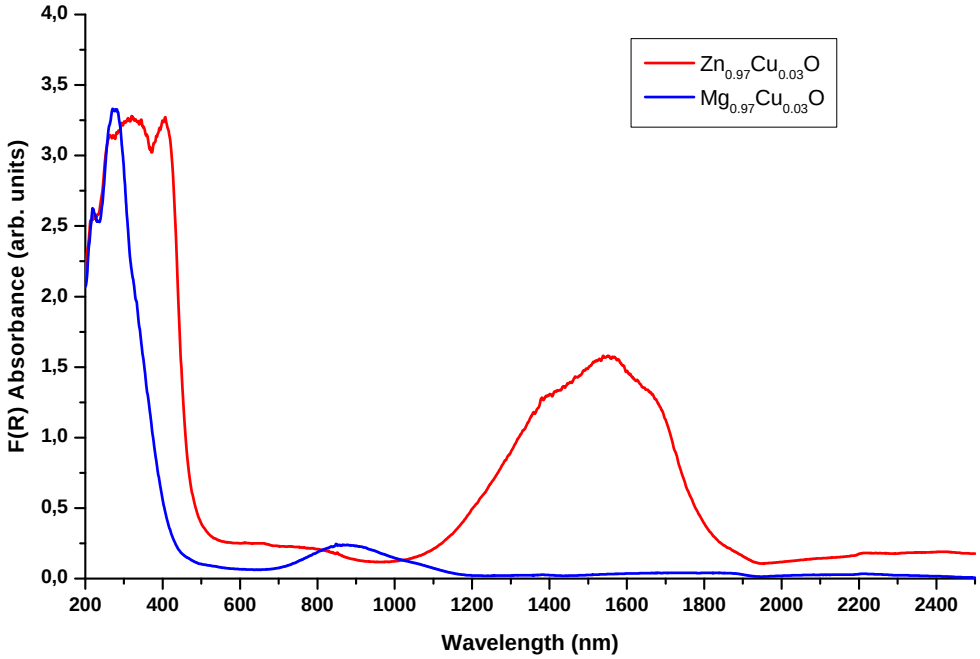

Figure 3.1: UV near-infrared spectrum of ZnO:Cu and MgO:Cu doped 3 at%.

ure 3.2).

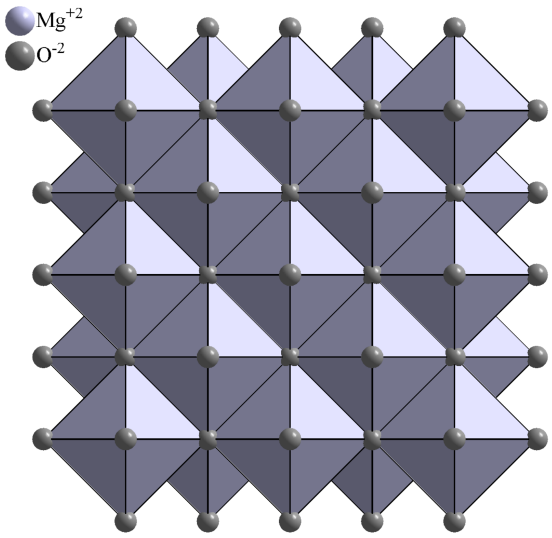

Figure 3.2: Projection along a of the MgO structure. The MgO_6 units are shown as purple octahedra.

The free ion term Cu^{2+} is ^2D and in a perfect octahedral crystal field it splits into ^2E_g and $^2T_{2g}$ energy levels [70]. The absorption band centered at 880 nm (Figure 3.3) is the physical evidence of the *d* - *d* transition and can be attributed to $^2E_g \leftarrow {}^2T_{2g}$. The low intensity of the absorption band is explained by the position of copper in a perfect octahedron. Due to the centre of symmetry and using the selection rule, it gives a *Laporte* forbidden character to this transition resulting in a low ϵ_{max} (Chapter 1, Table 1.2).

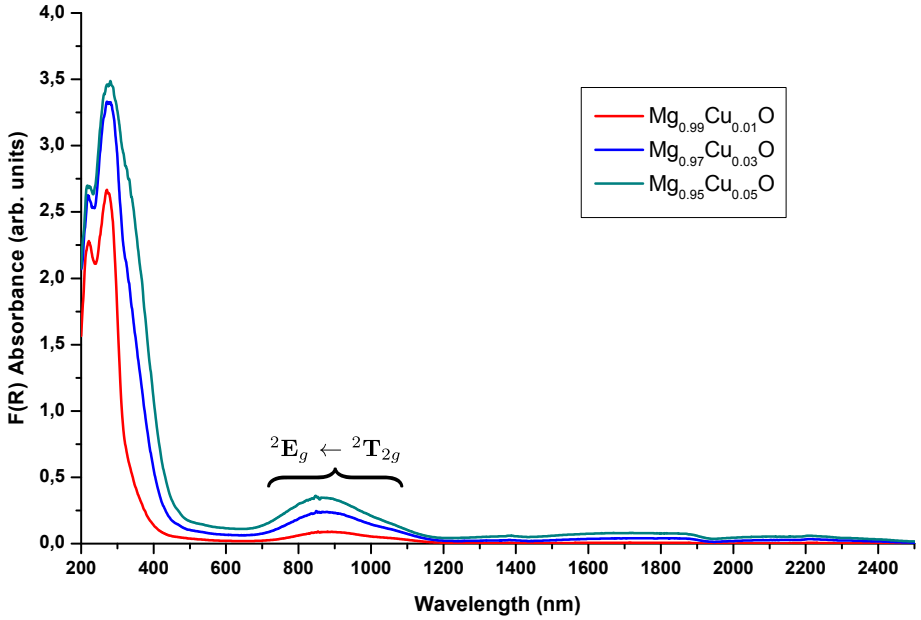

Figure 3.3: UV near-infrared spectrum of MgO:Cu doped 1, 3 and 5 at% respectively.

3.3.2 Copper doped zinc oxide

In the case of copper doped zinc oxide, attribution of the absorption bands is less straight forward. Indeed, zinc oxide crystallises in the wurtzite structure type (like ZnS) and the space group is the hexagonal $P6_3mc$, where the zinc atom is found to be situated in tetrahedrally surrounded cavities (Figure 3.4).

It is very unusual for copper to be found in this type of coordination unless it is

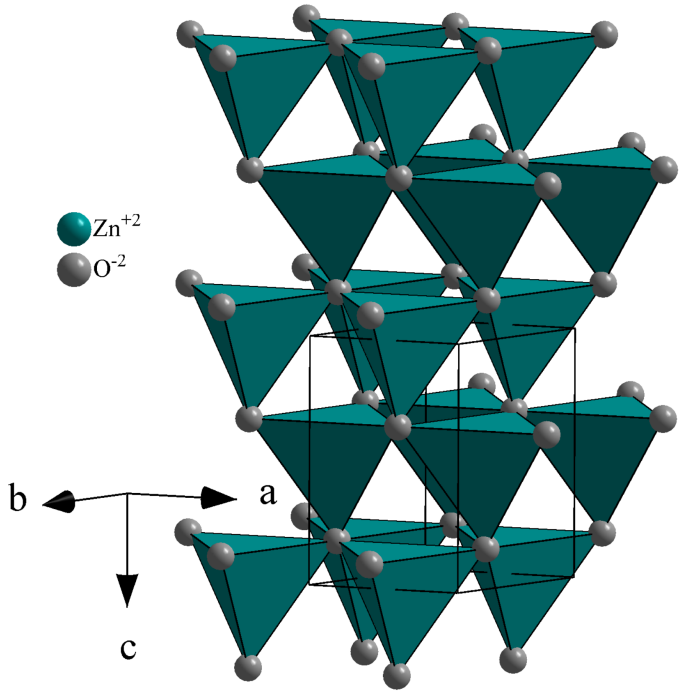

Figure 3.4: Projection of the ZnO structure. The ZnO_4 units are shown as teal tetrahedra.

distorted. In a study carried out by Solomon *et al.* [71] on blue copper proteins, it is assumed that a distorted tetrahedral surrounding of copper ions leads to a broad absorption band centred at 1560 nm, which consist of three overlapping bands (Figure 3.5). These three bands derive from three different *d* - *d* excitations, arising from $^2E \leftarrow {}^2B_2$, $^2B_1 \leftarrow {}^2B_2$ and $^2A_1 \leftarrow {}^2B_2$ respectively, with $^2B_2$ being the ground state of Cu(II) in that environment. The intensity of the absorption band is particularly high when compared to copper doped magnesium oxide spectroscopic data. The absence of a centre of symmetry in this structure shows the importance of *Laporte* selection rule.

The band at 775 nm may be attributed to the band gap of cupric oxide (1.2 eV [72]) indicating that, althought it is not visible in the PXD data, a very small quantity of dopant metal oxide did not react with the ZnO phase. However, the most probable hypothesis is the presence of a discrete level of energy close to the conduction band created by the replacement of zinc atoms by copper atoms. Electrons from the conduc-

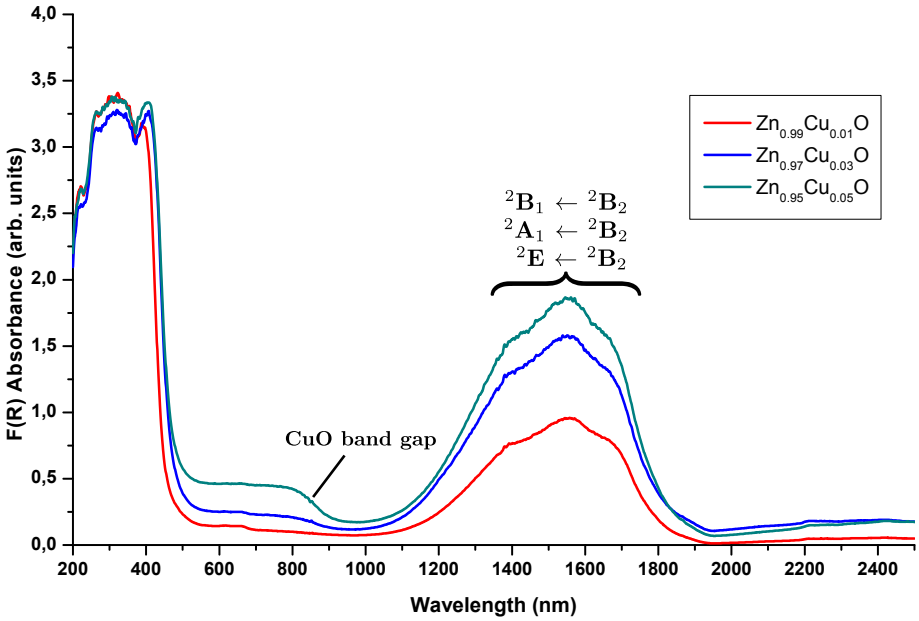

Figure 3.5: UV near-infrared spectrum of ZnO:Cu doped 1, 3 and 5 at% respectively.

tion band once excited can therefore jump into the empty discrete level resulting in this absorption band.

3.4 Conclusion

Simple metal oxides have been doped with diverse elements in order to discover light coloured candidate materials with high absorption in the near-infrared.

This preliminary work was focused on introducing discrete levels of energy in the band gap of semiconductors in order to induce the emergence of absorption bands in the near-infrared. While this idea was proven to be unsuccessfull, this study emphasize the role of *d* - *d* transitions as a mean to obtain the desired absorption band.

In the case of copper doped magnesium oxide it has been underlined that the absorption band can be adequatelly situated just outside the visible region, whereas in the case of copper doped zinc oxide, the position was not ideal but the intensity was

perfect.

The combination of both of these properties into one material will be the aim of the next Chapters.

CHAPTER 4

SIMPLE COPPER PHOSPHATE PIGMENTS

4.1 Introduction

The materials chemistry of copper compounds has been widely developed for the past three decades due to their unusual electronic and magnetic properties. In particular, compounds with copper in the oxidation state +2 and +3, where this element exhibits a *Jahn Teller* distortion, have been extensively studied to discover new high temperature superconducting compounds such as $YBa_2Cu_3O_7$ [73].

Furthermore, phosphate pigments were the focus of scientific interest in the past for their chemical resistance and their non-toxicity. One example for the useful application of phosphate pigments is the protection of metal surfaces against rust. In addition, transition metal phosphate pigments have been synthesised and characterised for their decorative colour. Such pigments include the violet $Co_3(PO_4)_2$ and the blue $Co_2P_2O_7$ [74].

Traditionally, copper compounds are used as blue pigments, *e.g.* Egyptian blue ($CaCuSi_4O_{10}$), and some blue copper phosphates are known from nature, *e.g.* the mineral turquoise, which is a hydrated copper aluminium phosphate $CuAl_6(PO_4)_4(OH)_8{\cdot}5(H_2O)$. In the former, copper is in a perfect square planar environment while in turquoise it is in an elongated rhombic octahedron [75]. These examples already give an idea about the structural versatility of copper(II) ions, which occur in

rather different coordination spheres.

Many synthetic copper phosphates have been structurally described *e.g.* $Cu_2P_2O_7$, $Cu_4P_2O_9$, $Cu_5P_2O_{10}$, $Cu_3(PO_4)_2$, $Cu_2P_4O_{12}$, *etc* and also their magnetic properties are often known. However none of them has been spectroscopically analysed.

In this section, the synthesis of several copper phosphates and their characterisation has been carried out using PXD and UV to near-infrared spectroscopy in an attempt to discover candidate materials with promising near-infrared absorption properties for further studies.

4.2 Synthesis

A range of copper phosphate pigments were synthesized ($Cu_2P_2O_7$, $Cu_4P_2O_9$, $Cu_5P_2O_{10}$, $Cu_3(PO_4)_2$ and $Cu_2P_4O_{12}$) using the conventional solid state reaction technique. CuO and $(NH_4)_2HPO_4$ were ground together with respect to the stoichiometry of the aimed pigment. The mixture produced was then heated up slowly (ramp 0.5 °C min^{-1}) to 900 °C. The resulting powder was allowed to cool in the air and was then homogenized with a pestle and mortar.

Analysis of the first synthesis attempts of this series showed the presence of significant amounts of Cu_2O, which could not be removed. The Cu_2O was derived from CuO at high temperatures, indicating that part of this starting material was not consumed by the formation of the aimed product. Therefore another method was used to produce the desired phosphate powders.

The starting materials were ground together, however instead of heating the mixture directly up to 900 °C, it was first heated slowly (ramp 0.5 °C min^{-1}) to 450 °C and then cooled and reground. Then a new pellet was pressed and fired up to 900 °C for 48 hours. The resulting powder was allowed to cool in the air and was then homogenized with a pestle and mortar. Several cycles were necessary to obtain pure powders.

The obtained products were all studied using PXD and near-infrared spectroscopy. In the following sections $Cu_2P_2O_7$ and $Cu_2P_4O_{12}$ are discussed in detail.

4.3 Structural Refinement

Room temperature PXD data were collected on a Siemens D5000 diffractometer according to the method outlined in Chapter 2. Each sample represented the respective desired pigment, which was confirmed by comparison of the peak positions with the d-spacing values listed in the literature [76–81].

Rietveld refinements were performed using the GSAS suite of programs [54] in conjunction with the graphical interface EXPGUI [55]. The initial model was taken from *Lukaszewicz* for α-$Cu_2P_2O_7$ [76] and from *Laugt and Durif* for $Cu_2P_4O_{12}$ [80]. For both data sets, the background was manually modelled and lattice parameters were refined to match the experimental reflection positions. The peak profiles were refined using function two, followed by the atomic positions. Isotropic thermal factors were the last introduced. Once the refinement was smoothly converging, the background was left to refine using the shifted Chebyschev function with four terms.

Some impurity peaks were found in both structural refinements, however, they could not be assigned to a known phase due to their low intensities. The refinement profile fit of $Cu_2P_2O_7$ is presented in Figure 4.1 and tables of refined crystallographic data follow (Table 4.1 and Table 4.2).

Each of the structures is built up with phosphate groups (PO_4) in a nearly perfect tetrahedral shape (the average P-O bond distance is close to 1.54 Å, the average O-P-O angle is close to 110°), with copper occupying either an octahedral site (CuO_6) or a square pyramidal site (CuO_5).

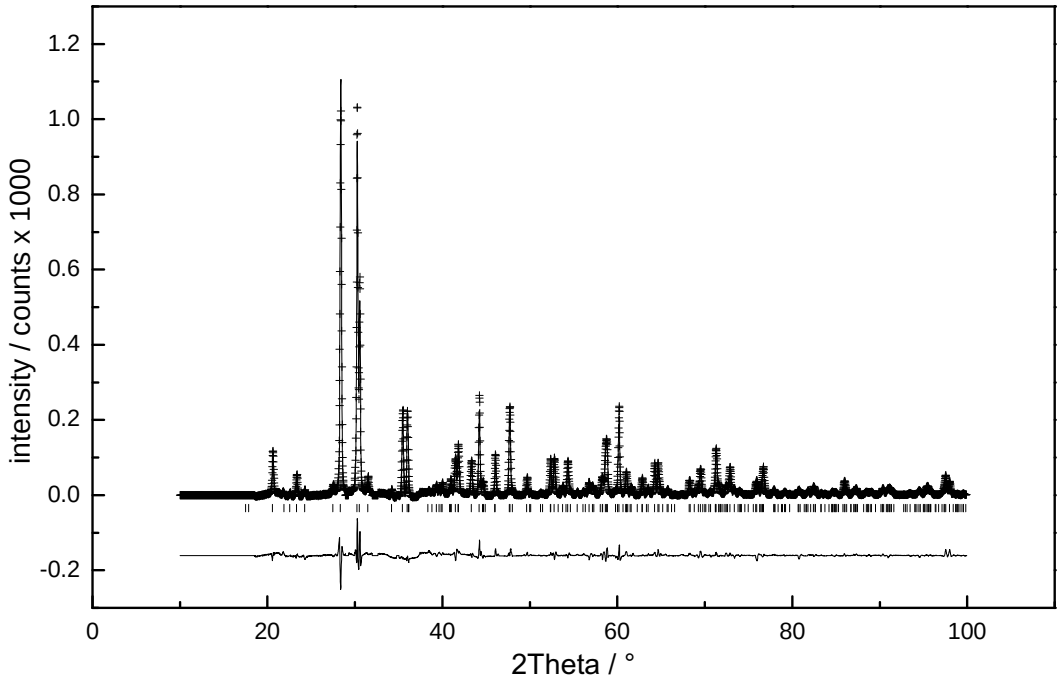

Figure 4.1: *Rietveld* refinement profile fit of $Cu_2P_2O_7$. Observed data points are shown as crosses and the calculated pattern is shown as a solid line. The difference between the calculated and observed patterns is shown underneath. The position of the peaks are marked by the row of vertical lines.

Table 4.1: Crystallographic data for $Cu_2P_2O_7$ (e.s.d.s in parentheses).

Space group *C2/c*.
Lattice parameters a = 6.8810(1) Å, b = 8.1086(1) Å, c = 9.1575(2) Å, β = 109.569(1) °

Atom	x	y	z	U_{iso} / Å^2*100
Cu1	-0.0162(3)	0.3132(2)	0.5073(2)	1.56(3)
P1	0.1991(3)	0.0068(4)	0.2050(3)	1.29(6)
O1	0	0.0475(9)	1/4	1.33(8)
O2	0.3794(7)	-0.0004(10)	0.3589(6)	1.33(8)
O3	0.2197(10)	0.1482(8)	0.1144(7)	1.33(8)
O4	0.1817(10)	-0.1598(9)	0.1194(7)	1.33(8)

Final fit parameters: $R(F^2)$ = 6.23%, R_{wp} = 10.38%, R_p = 7.71%

Table 4.2: Crystallographic data for $Cu_2P_4O_{12}$ (e.s.d.s in parentheses).

Space group *C2/c*.
Lattice parameters a = 12.5406(5), b = 8.0825(7), c = 9.5712(9) Å, β = 118.541(4) °

Atom	x	y	z	U_{iso} / Å^{2}*100
Cu1	1/4	1/4	0	2.44(4)
Cu2	0	0.5557(6)	1/4	2.44(4)
P1	0.3090(5)	0.5059(7)	0.2940(7)	2.53(6)
P2	0.5076(5)	0.7371(8)	0.4822(8)	2.53(6)
O1	0.4178(8)	0.6230(12)	0.3462(12)	1.22(6)
O2	0.3697(9)	0.3642(12)	0.4266(8)	1.22(6)
O3	0.2706(10)	0.4256(10)	0.1388(9)	1.22(6)
O4	0.2196(10)	0.5941(9)	0.3304(11)	1.22(6)
O5	0.5481(9)	0.2217(12)	0.4117(10)	1.22(6)
O6	0.4661(10)	0.1142(10)	0.5971(7)	1.22(6)

Final fit parameters: $R(F^2)$ = 9.53%, R_{wp} = 11.93%, R_p = 9.42%

4.4 UV to Near-Infrared Spectroscopy

UV to near-infrared absorption data (200 to 2500 nm range) were collected on undiluted samples according to the method outlined in Chapter 2. The spectra are compared to each other in Figure 4.2.

The absorption spectra tend to be rather similar for all samples, with an absorption band centred at roughly ~1000 nm with the exception of $Cu_2P_4O_{12}$ which presents two maxima. Depending on the compound and thus the coordination state of copper, the absorption band is shifted towards higher or lower wavelengths. As the phosphate units, which are the ligands through oxygen bonding, are very similar for all the struc-

tures, the change in crystal field stabilisation energy is only due to the copper being in a differently shaped coordination environment.

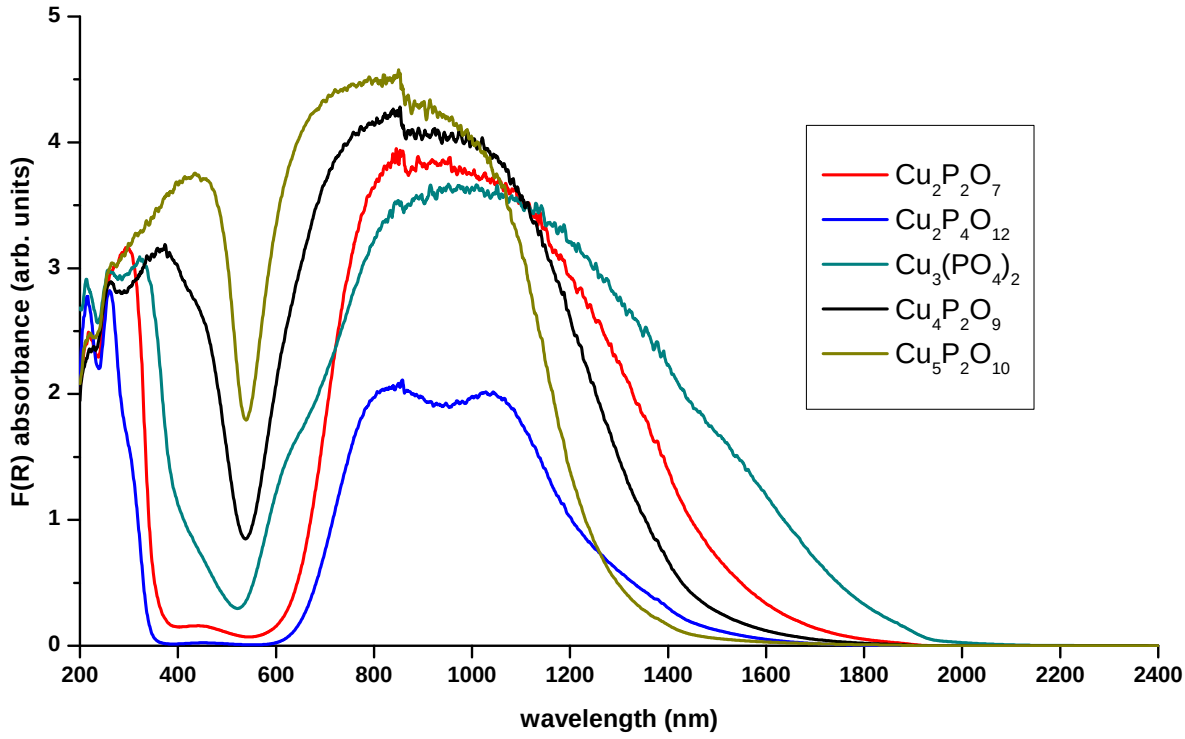

Figure 4.2: UV to near-infrared spectra of the copper phosphates synthesised in this section.

4.5 Results

In order to explain the absorption properties of the compound it is necessary to thoroughly examine the coordination sphere of the copper ions. They directly influence the energy levels of *d*-orbitals of the Cu^{2+} ions through crystal field splitting and therefore have a large impact on the related electron transitions which are responsible for the absorption behaviour.

4.5.1 $Cu_2P_2O_7$

In the structure of $Cu_2P_2O_7$, copper occupies a five-fold coordinated site (Figure 4.3).

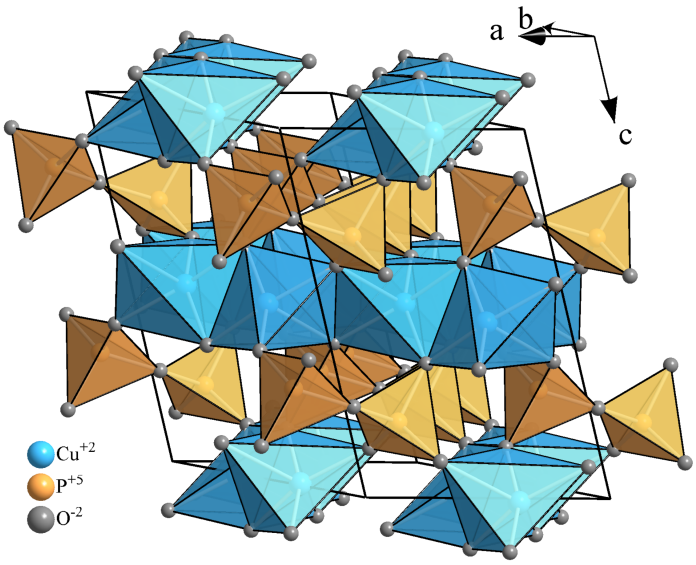

Figure 4.3: Projection of the $Cu_2P_2O_7$ structure. The PO_4 units are shown as orange tetrahedra, the five-fold arrangement around the Cu atoms is shown in blue.

From the bond distance information obtained through *Rietveld* refinement of X-ray data (Table 4.3), one bond is significantly elongated compared to the others which are very similar (Figure 4.4). It is therefore evident that this is a distorted square pyramidal site. For a perfect square-based pyramidal geometry, the symmetry would be C_{4v}.

From a molecular orbital point of view, assuming that all ligands are the same (ML_5), the molecular orbital diagram for this geometry is as described in Figure 4.5 (a). The deviation from this idealised geometry, with the apical ligand further away from the metal and distortion of the basal plane (Figure 4.5 (b)) induces a destabilisation of the d_{xz} and d_{yz} orbitals, while d_{z^2} is stabilised since there is less repulsion along the z axis. For a d^9 transition metal and using the hole formalism, the expected electronic transitions are $^2A_1 \leftarrow {}^2B_1$, $^2E \leftarrow {}^2B_1$ and $^2B_2 \leftarrow {}^2B_1$. However, the difference between these energy levels is negligible and the electronic spectrum shows only a broad single band (Figure 4.6).

Table 4.3: Derived bond distances and angles for the coordination sphere of copper in $Cu_2P_2O_7$ (e.s.d.s in parentheses).

Bond	Distance / Å	Bond Angle	Angle / °
Cu1_O2	1.998(7)	O2_Cu1_O2	80.2(2)
Cu1_O2	1.979(7)	O2_Cu1_O3	95.9(3)
Cu1_O3	1.987(7)	O2_Cu1_O4	154.6(3)
Cu1_O3	2.357(5)	O2_Cu1_O3	164.4(3)
Cu1_O4	1.876(7)	O2_Cu1_O4	93.6(3)
		O3_Cu1_O4	96.1(2)

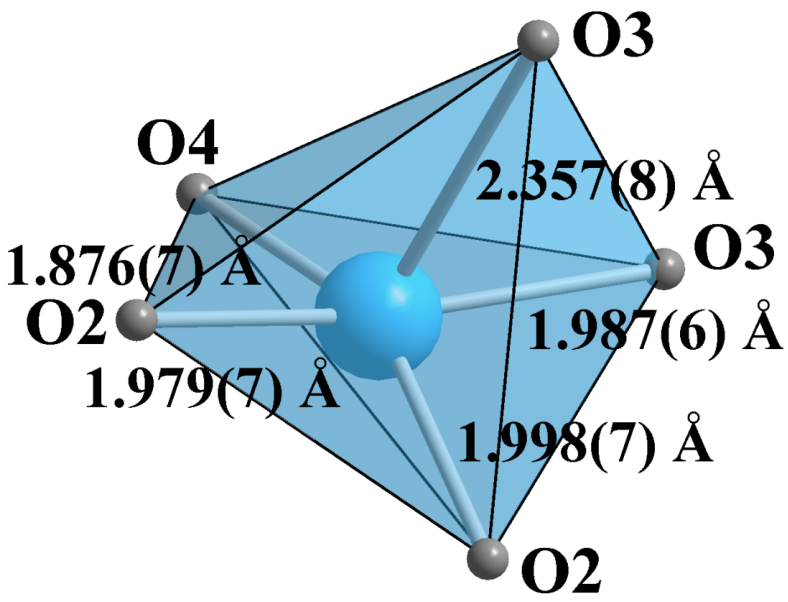

Figure 4.4: CuO_5 distorted square pyramidal site in $Cu_2P_2O_7$.

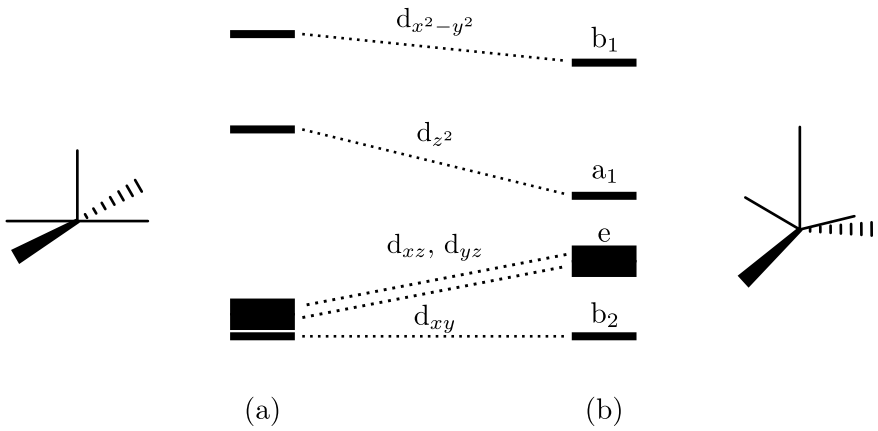

Figure 4.5: The orbital correlation diagram for (a) a square pyramid (C_{4v}) and (b) a distorted square pyramid (C_{2v}).

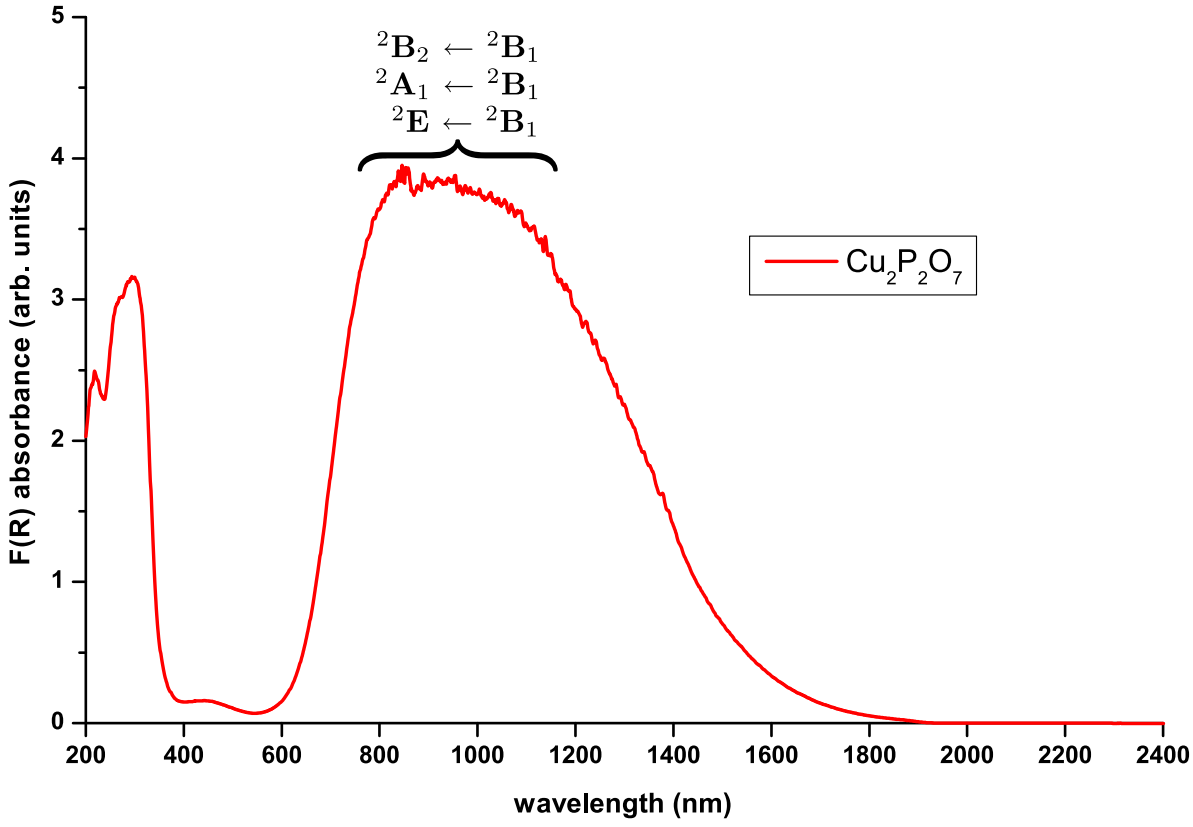

Figure 4.6: UV near-infrared spectrum of $Cu_2P_2O_7$

4.5.2 $Cu_2P_4O_{12}$

In this compound, copper is coordinated to six oxygen atoms forming an octahedron (Figure 4.7). As expected from the *Jahn Teller* effect [15, 16], this octahedral site is tetragonally distorted; the axial bonds are elongated while the equatorial bonds are slightly shortened (Table 4.4).

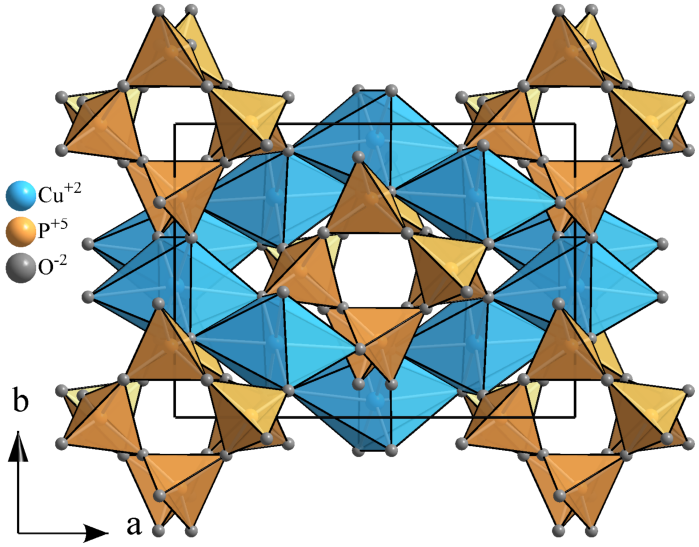

Figure 4.7: Projection along the c axis of the $Cu_2P_4O_{12}$ structure. The PO_4 units are shown as orange tetrahedra, the tetragonally distorted octahedral arrangements around the Cu atoms is shown in blue.

The symmetry of a perfect octahedron is O_h with only two resulting energy levels for a d^9 configuration: the ground state ^2E_g and the excited state $^2T_{2g}$. The tetragonal distortion lowers the geometry to D_{4h} and is accompanied by additional splitting of these two levels (Figure 4.9). Excitation can occur from the ground state $^2B_{1g}$ to the excited levels $^2A_{1g}$, ^2E_g and $^2B_{2g}$. This would account for the broadening of an absorption band or a shoulder due to two overlapping bands, but not for the two distinct bands centred at 800 nm and 1100 nm, respectively.

The fact that two distinct bands are present in the spectrum can be explained using the refined X-ray data. In the structure, the copper atom is situated in two separate positions with quite distinctive bond lengths (Table 4.4). For the first position, the oc-

Table 4.4: Derived bond distances and angles for the coordination spheres of copper in $Cu_2P_4O_{12}$ (e.s.d.s in parentheses).

Bond	Distance / Å	Bond Angle	Angle / °
Cu1_O3	1.875(5)	O3_Cu1_O3	179.9(0)
Cu1_O3	1.875(5)	O3_Cu1_O4	90.3(5)
Cu1_O4	1.942(4)	O3_Cu1_O4	89.7(5)
Cu1_O4	1.942(4)	O3_Cu1_O4	89.7(5)
Cu1_O5	2.266(7)	O3_Cu1_O4	90.3(5)
Cu1_O5	2.266(7)	O4_Cu1_O4	180.0(0)
Cu2_O4	2.499(8)	O5_Cu2_O5	91.1(6)
Cu2_O4	2.499(8)	O5_Cu2_O6	90.9(5)
Cu2_O5	1.915(5)	O5_Cu2_O6	175.2(7)
Cu2_O5	1.915(5)	O5_Cu2_O6	175.2(7)
Cu2_O6	1.900(7)	O5_Cu2_O6	90.9(5)
Cu2_O6	1.900(7)	O6_Cu2_O6	87.5(6)

tahedral coordination sphere is less distorted than for the second one, the axial copper oxygen bond lengths are 2.27 Å compared to 2.50 Å while the averaged equatorial bond lengths are 1.91 Å for both sites. Energetically speaking, that means ^2E_g and $^2T_{2g}$ split more readily for copper in the second site than in the first (Figure 4.10).

From this observation, three electronic transitions are expected for each crystallographical copper site. The band at 800 nm is attributed to the $^2E_g \leftarrow {}^2B_{1g}$ transition of Cu2; the energy difference between these two levels is higher due to the strong tetragonal distortion. The band at 1100 nm derives from the $^2E_g \leftarrow {}^2B_{1g}$ transition of Cu1 and the $^2B_{2g} \leftarrow {}^2B_{1g}$ and $^2A_{1g} \leftarrow {}^2B_{1g}$ transitions from Cu2. Both of these Cu2 electronic transitions are probably indistinguishable since they are too close in energy. The shoulder at 1350 nm comes probably from the $^2A_{1g} \leftarrow {}^2B_{1g}$ and the $^2A_{1g} \leftarrow {}^2B_{1g}$ transi-

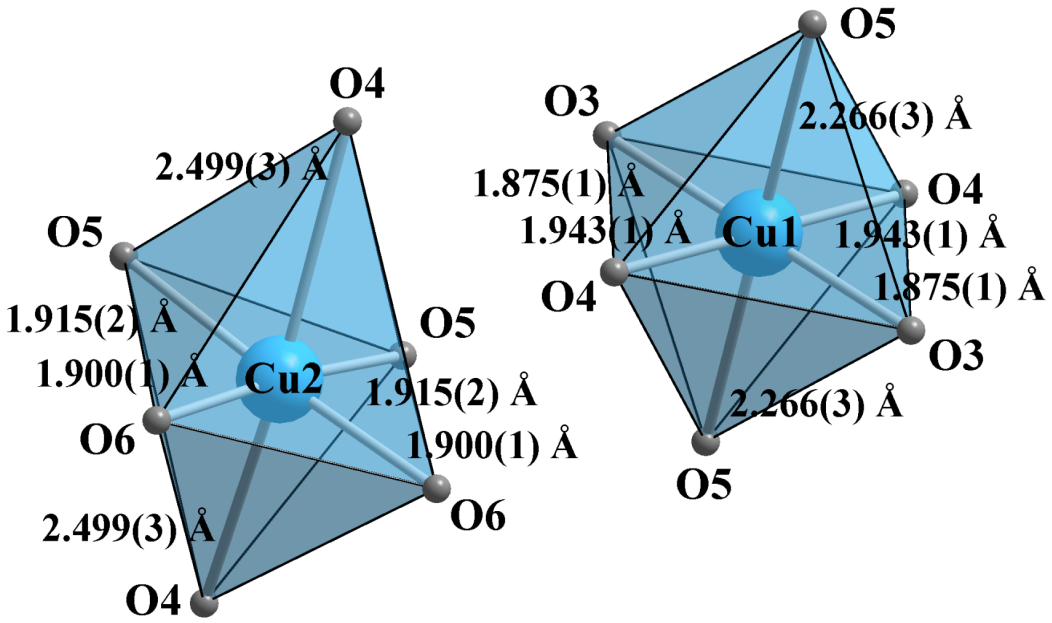

Figure 4.8: CuO_6 distorted octahedral sites in $Cu_2P_4O_{12}$.

tion of Cu1 (Figure 4.11).

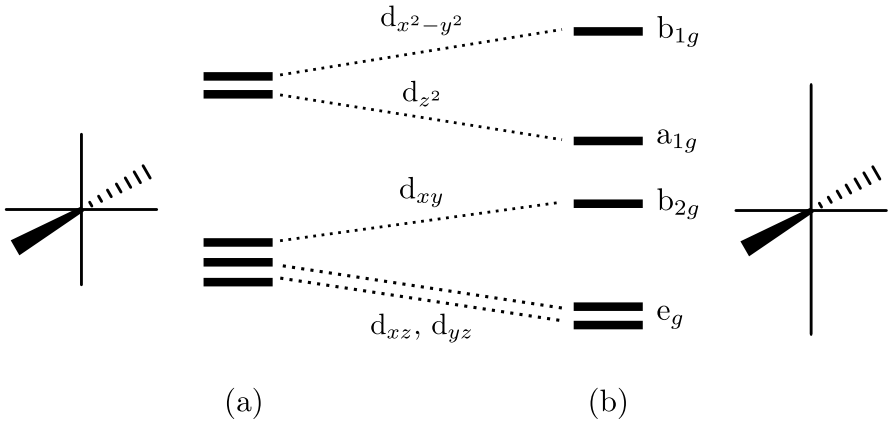

Figure 4.9: The orbital correlation diagram for (a) a regular octahedral arrangement (O_h) and (b) a tetragonally distorted octahedral site (D_{4h}).

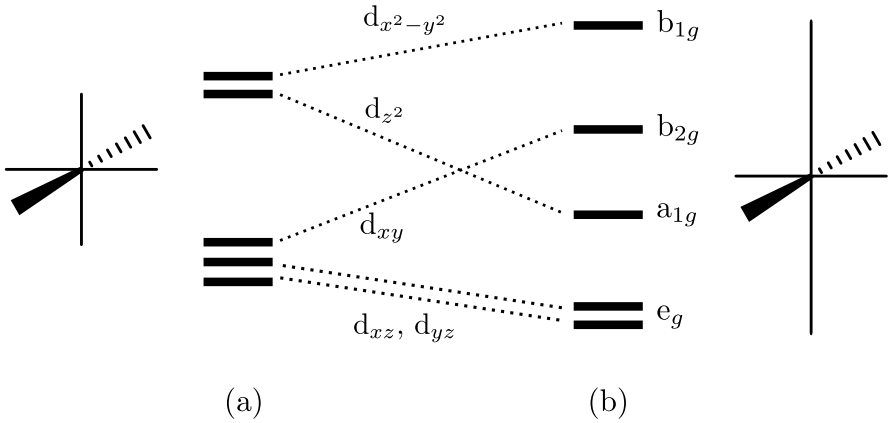

Figure 4.10: The orbital correlation diagram for (a) a regular octahedral arrangement (O_h) and (b) a strongly tetragonally distorted octahedral site (D_{4h}).

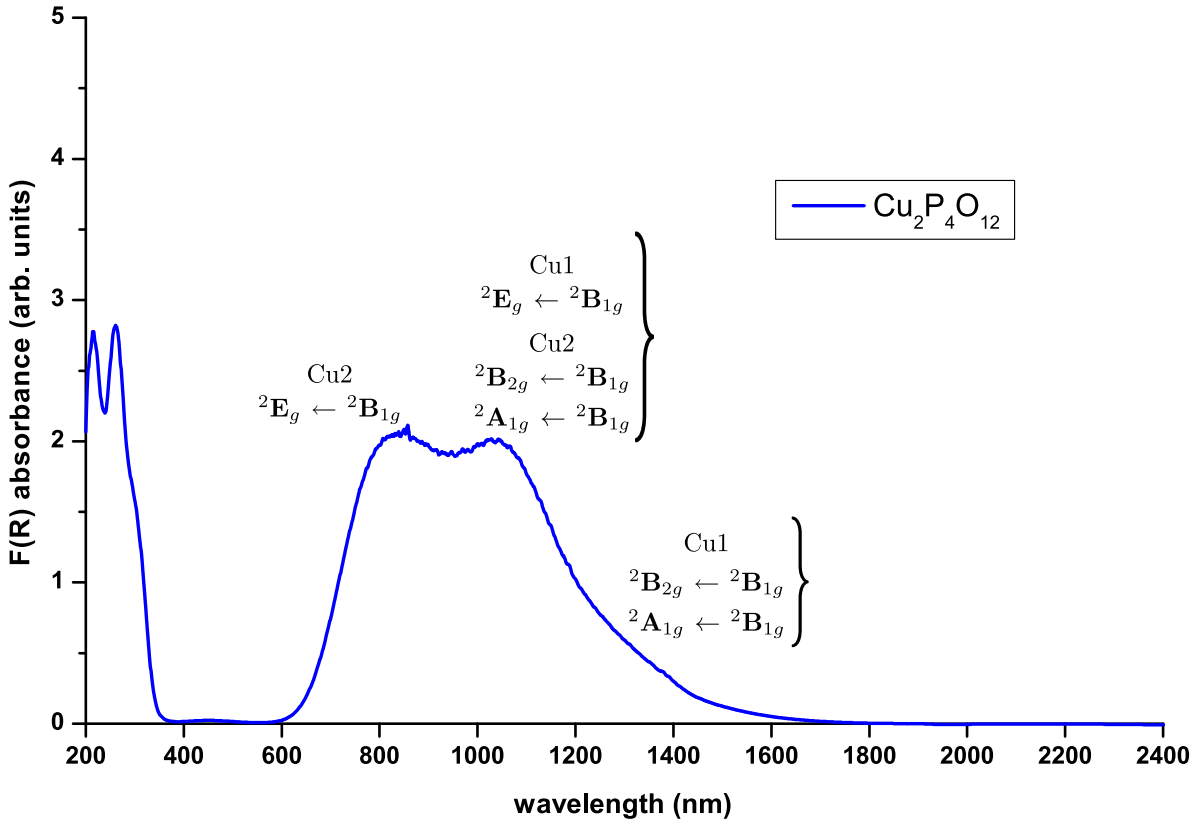

Figure 4.11: UV near-infrared spectrum of $Cu_2P_4O_{12}$

4.6 Discussion

Absorption maximum

The absorption maximum is strongly dependent of the crystal field stabilisation energy. Phosphate ligands are weak field ligands which gives the copper(II) ion the ability to have its *d* - *d* transitions lying in the red region of the visible and the near-infrared. By altering the environment of copper through phosphate units linking or cationic mixing, the absorption can be adjusted to the desired wavelength. One example of this effect is seen in the $Cu_2P_4O_{12}$ material where two distinct octahedral sites are present giving rise to two separate bands.

In a perfect octahedral site, the crystal field splitting energy (Δ_o) is given by the wavelength of the absorption maximum for a d^9 ion. Because of the *Jahn Teller* effect, it is not possible to determine this term for copper(II) in $Cu_2P_4O_{12}$. However, since copper is situated in two different sites in the same environment and considering the position of the absorption maximum is proportional to the *Jahn Teller* elongation, it is possible to extrapolate the optimal tetragonal elongation for an absorption maximum at 1000 nm in a phosphate material which was estimated at 2.40 Å.

Intensities

For all of these pigments, the absorption mechanism is due to *d* - *d* transitions. As seen in Chapter 1 they are spin allowed but symmetry forbidden (*Laporte* forbidden) because they involve no change in the inversion properties of the electron. The fact that these pigments show strong absorption bands means that selection rules are partially broken.

For $Cu_2P_2O_7$ the *Laporte* restriction cannot take place since there is no centrosymmetric environment in a square pyramidal geometry. The distortion here only shifts the position of the absorption maximum.

The *Jahn Teller* effect is a distortion which does not destroy the centre of symmetry. Therefore, it does not account for any increase in absorption intensities. However, it

is often accompanied by vibrational modes which are seen as angle variations from perfect symmetry [13]. In the solid state, these vibrational mode are static, the atoms are connected to each other with definite bond distances and angles due to the close packing of atoms in a crystal. The small angle distortion of the sites in $Cu_2P_4O_{12}$ is enough to partially relax the *Laporte* rule, giving rise to these absorptions. The Cu2 octahedral site is slightly more distorted than the Cu1 site. The absorption band derived from Cu2 should be more intense than the absorption band from Cu1. However, the same absorption intensity is described for both of them. It is suspected that this is the effect of the addition of the $^2E_g \leftarrow {}^2B_{1g}$ transition of Cu1 and the $^2B_{2g} \leftarrow {}^2B_{1g}$ and $^2A_{1g} \leftarrow {}^2B_{1g}$ transitions from Cu2.

4.7 Conclusion

$Cu_2P_2O_7$ and $Cu_2P_4O_{12}$ have been studied using UV to near-infrared spectroscopy and powder X-ray diffraction.

The electronic properties of these pigments has been fully characterised and some selection criteria for identifying the perfect near-infrared absorbing candidate material have been isolated.

A good pigment candidate with infrared absorbing properties would therefore have copper ions in octahedral sites strongly distorted through *Jahn Teller* effect with a large vibronic coupling or in a five-fold geometry to remove the centre of symmetry.

This would then allow strong electron transitions in the desired region of the energy spectrum.

CHAPTER 5

CALCIUM AND STRONTIUM COPPER(II) PYROPHOSPHATES

5.1 Introduction

One way to tune the shape of the copper coordination is to form a material from one of the simple copper phosphates described previously but implementing two different types of cations.

The first candidate materials investigated here were the divalent alkaline earth metal ion diphosphates $CaCuP_2O_7$ and $SrCuP_2O_7$ described by *Boukhari et al.* [82].

In these mixed cation phosphates, copper is situated in a five coordinate oxygen environment made up by regular PO_4 tetrahedra forming $P_2O_7^{4-}$ tetrahedral pairs. The calcium or strontium atoms occupy seven-fold coordinated sites within the structure (Figure 5.1).

This section describes the synthesis and characterisation of both $CaCuP_2O_7$ and $SrCuP_2O_7$ materials.

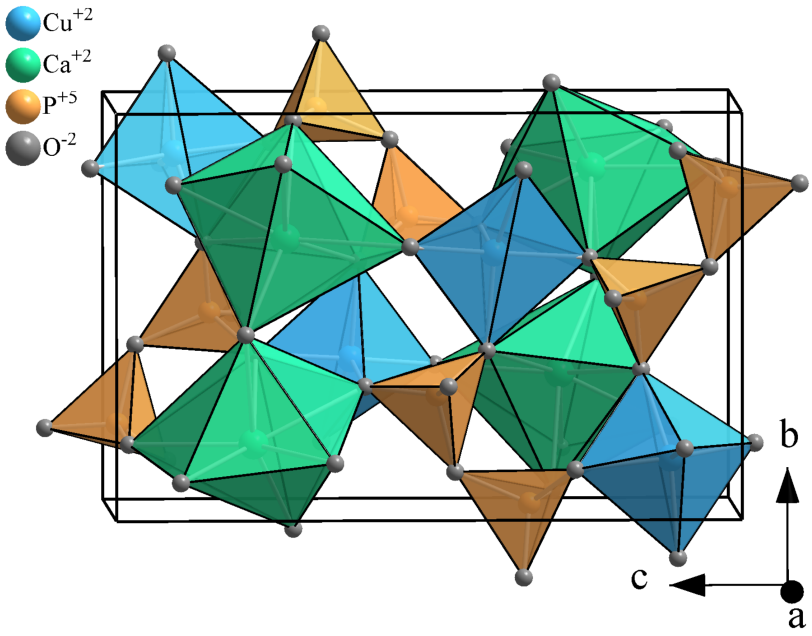

Figure 5.1: Projection along the a axis of the $CaCuP_2O_7$ structure. The PO_4 units are shown as orange tetrahedra, the distorted square pyramidal arrangement around the Cu atoms is shown in blue and the isolated site for Ca atom is shown in green.

5.2 Synthesis

Polycrystalline samples of $CaCuP_2O_7$ and $SrCuP_2O_7$ were prepared using conventional solid state synthesis methods. $CaCO_3$ or $SrCO_3$ respectively, was ground with $(NH_4)_2HPO_4$ and CuO in the relevant molar ratio, using a pestle and mortar. The resulting mixture was slowly heated up to 500 °C (ramp 0.4 °C min^{-1}) and kept at this temperature for 15 hours. Pressed into a pellet, the resulting products were further sintered at 900 °C in a box furnace for 24 hours. The light blue coloured materials obtained were then removed from the furnace, left to cool down to room temperature in the air and ground to a fine powder for further analysis.

The preliminary PXD data showed some unreacted CuO starting material for both of these samples. Further cycling did not improve the quality, therefore, instead of a

conventional solid state method, a wet method was used.

$CaCO_3$ or $SrCO_3$ respectively and CuO were dissolved in the minimum of water/HNO_3 until a clear solution was obtained. This solution was precipitated by introduction of an aqueous solution of $Na_2P_2O_7$. The precipitate was then filtered, washed with cold water and heated up slowly to 500 °C (ramp 0.4 °C min^{-1}) and kept at this temperature for 15 hours. The powder was ground and sintered at 900 °C for another 24 hours. The light blue coloured materials obtained were then removed from the furnace, left to cool down to room temperature in the air.

These samples were analysed by powder X-ray diffraction and UV to near-infrared spectroscopy. The preliminary PXD data showed the presence of the main phase $CaCuP_2O_7$ or $SrCuP_2O_7$ with some calcium phosphate or strontium phosphate impurities respectively. As these impurities were colourless, no further purification was attempted.

5.3 Powder X-ray Diffraction

PXD data were collected overnight on a Bruker D8 diffractometer using the method outlined in Chapter 2. *Rietveld* structural refinements were performed using the GSAS program.

The starting model for the $CaCuP_2O_7$ refinement was taken from *Riou et al.* [83]. The first step was to model the background and fit the peak profiles and lattice parameters using a *Le Bail* fit on the main phase. The background was manually fitted in order to limit the number of terms used. Once the R factors and χ^2 values were sensible as well as the profile parameters, atom positions were varied. Isotropic thermal factors followed, with a constraint on the same atom type to limit any substantial variations. When all parameters could be refined altogether, $Ca_2P_2O_7$ was added as a second phase and refined with the same profile parameters as the main phase. Finally the phase fraction was obtained.

The refinement of $SrCuP_2O_7$ follows the same procedure using the structural model

Table 5.1: Refined crystallographic data for $SrCuP_2O_7$ (e.s.d.s in parentheses).

Space group $P\,2_1/n$.
Lattice parameters a = 12.4555(4) Å, b = 8.1385(3) Å, c = 5.3733(2) Å, β = 90.586(2) °

Name	x	y	z	U_{iso} / Å^{2*}100
Sr1	0.2191(2)	0.1544(3)	0.2123(5)	2.24(7)
Cu1	0.3853(3)	0.3511(6)	0.7053(7)	2.40(12)
P1	0.0098(6)	0.1896(9)	0.6806(16)	3.52(18)
P2	0.1566(6)	0.4653(11)	0.7546(15)	3.52(18)
O1	0.0950(12)	0.0918(16)	0.8353(27)	1.30(16)
O2	0.0243(11)	0.1864(17)	0.3909(27)	1.30(16)
O3	-0.1017(10)	0.1684(20)	0.7780(27)	1.30(16)
O4	0.0402(12)	0.3912(15)	0.7269(31)	1.30(16)
O5	0.2271(10)	0.3732(18)	0.5517(25)	1.30(16)
O6	0.1985(11)	0.4336(17)	0.0128(29)	1.30(16)
O7	0.1464(11)	0.6333(19)	0.6710(26)	1.30(16)

Final fit parameters: $R(F^2)$ = 7.28%, R_{wp} = 8.88%, R_p = 5.92%

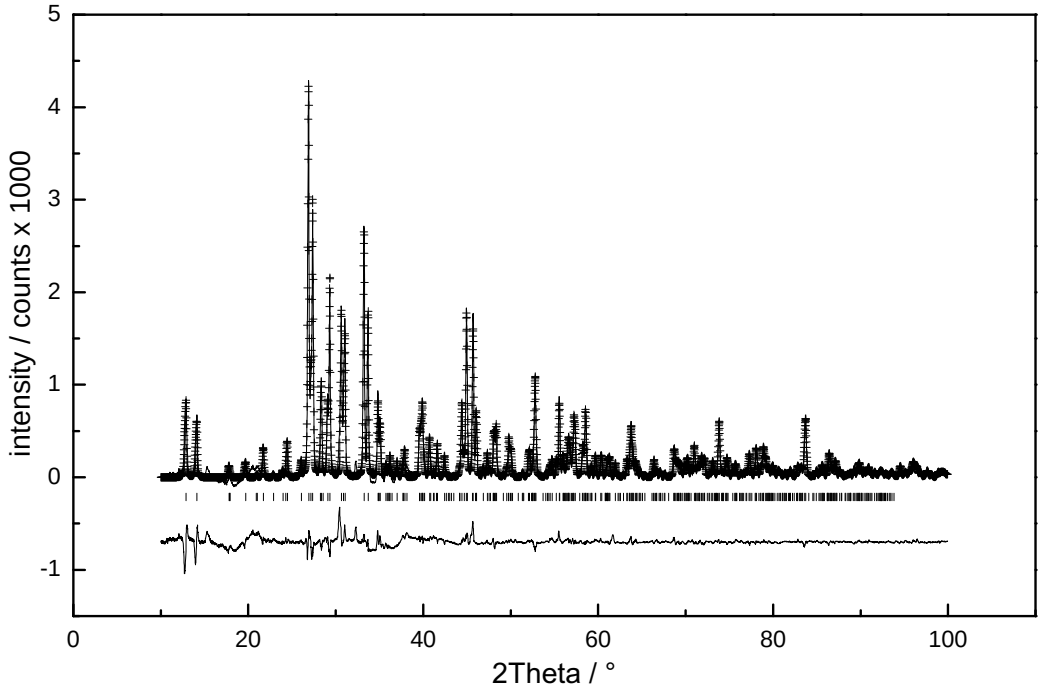

Figure 5.2: *Rietveld* refinement profile fit of $SrCuP_2O_7$. Observed data points are shown as crosses and the calculated pattern is shown as a solid line. The difference between the calculated and observed patterns is shown underneath. The position of the peaks are marked by the row of vertical lines.

from *Moqine et al.* [84]. The second phase was fitted as $Sr_2P_2O_7$. Table 5.1 lists the unit cell parameters and refinement information for this copper-mixed diphosphate.

Both refined structures are isomorphous to the α-$Ca_2P_2O_7$ structure [85]. The volume of $CaCuP_2O_7$ is smaller than the volume of $SrCuP_2O_7$ which is due to the difference in size of these cations (ionic radii for Sr^{2+}, Ca^{2+} and Cu^{2+} are 1.26 Å, 1.12 Å and 0.73 Å respectively [68]). The alkaline earth metal atom has a coordination number of seven while the copper atom is situated in a five-coordinate square pyramidal site (Tables 5.2 and 5.3). This square pyramidal site presents the same distortion discussed in Section 4.5.1 for $Cu_2P_2O_7$ with a notable difference for the elongated apical bond length; it is shorter for both $CaCuP_2O_7$ and $SrCuP_2O_7$ compared to $Cu_2P_2O_7$. If com-

Table 5.2: Derived bond distances and angles for $SrCuP_2O_7$ (e.s.d.s in parentheses).

Bond	Distance / Å	Bond Angle	Angle / °
Cu1_O1	1.988(10)	O1_Cu1_O2	93.3(5)
Cu1_O2	1.973(10)	O1_Cu1_O5	90.3(5)
Cu1_O3	2.295(11)	O1_Cu1_O7	165.4(5)
Cu1_O5	2.128(10)	O2_Cu1_O5	170.2(4)
Cu1_O7	1.917(12)	O2_Cu1_O7	82.3(5)
		O5_Cu1_O7	92.0(4)

Table 5.3: Derived bond distances and angles for $CaCuP_2O_7$ (e.s.d.s in parentheses).

Bond	Distance / Å	Bond Angle	Angle / °
Cu1_O1	1.923(10)	O1_Cu1_O2	93.3(5)
Cu1_O2	1.977(10)	O1_Cu1_O5	90.3(5)
Cu1_O3	2.040(11)	O1_Cu1_O7	167.4(5)
Cu1_O7	2.202(12)	O2_Cu1_O5	171.3(4)
Cu1_O5	1.994(10)	O2_Cu1_O7	79.3(5)
		O5_Cu1_O7	92.5(4)

pared to one another, the bond distance is longer for the heavier alkaline earth. The electronegativities of the strontium and calcium atoms are very similar (*i.e.* 0.95 and 1, respectively), this elongation difference is therefore likely to be the result of the differing sizes of these cations, although sitting in a different coordination sphere, they are adjacent to the coordination sphere of copper and thus influence it.

5.4 UV to Near-infrared Spectroscopy

Solid state UV to near-infrared data were collected on undiluted samples according to the method outlined in Chapter 2.

The broad transition bands observed in the visible to near-infrared region result from *d* - *d* transitions as expected from copper(II) situated in a distorted square pyramidal geometry. Both transitions occur at near identical wavelength at *ca.* 790 nm for the $^2E \leftarrow {}^2B_1$ transition and at *ca.* 1050 nm for the $^2A_1 \leftarrow {}^2B_1$ transition (Figure 5.3) in accordance to Section 4.5.1 and the selection rules [12]. A slight blue shift is observed for $SrCuP_2O_7$ which correlates to the apical bond length difference in the square pyramidal coordination sphere of the Cu^{2+} ions.

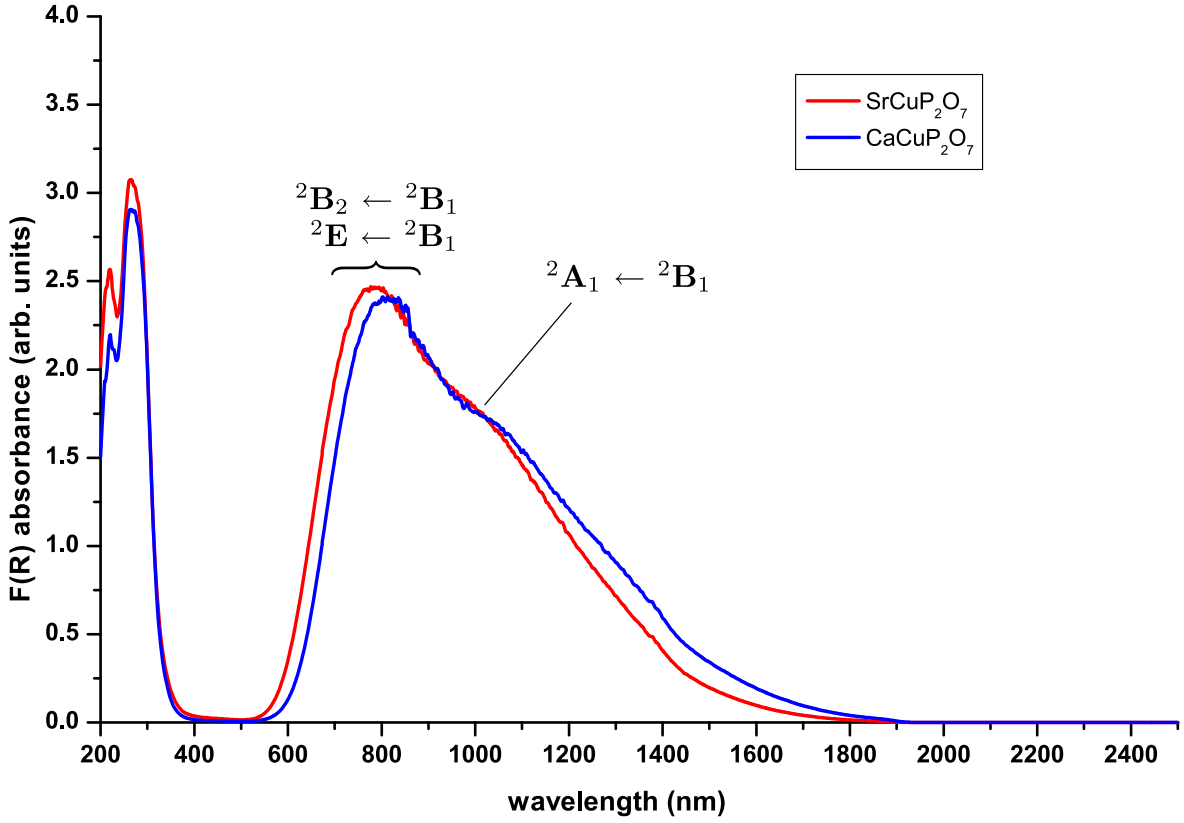

Figure 5.3: UV near-infrared spectra of $SrCuP_2O_7$ and $CaCuP_2O_7$

5.5 Discussion

In these related structures, the alkaline earth metals strontium and calcium are located in cages coordinated to the free apex of the phosphate tetrahedra. Alkaline earth metals have a strong ionic character and due to their lower charge/size ratio, strontium and calcium ionic strength is further enhanced [35].

Since copper atoms were coordinated to diphosphate groups through corner sharing, the influence of Ca^{2+} and Sr^{2+} ions could affect the ligand field splitting of phosphate groups and indirectly push the *d* - *d* transitions further into the near-infrared region. However, from Figure 5.3, this effect is overwhelmed by the distortion of the

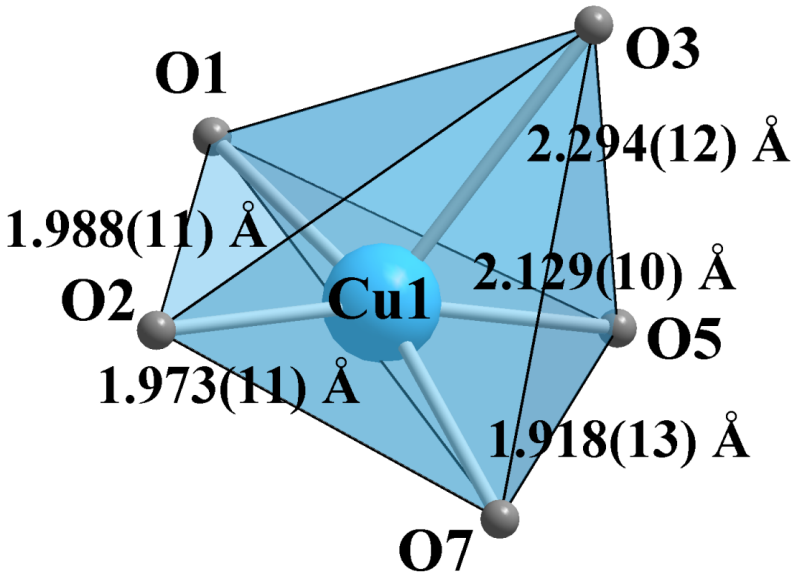

Figure 5.4: CuO_5 distorted square pyramidal sites in $SrCuP_2O_7$.

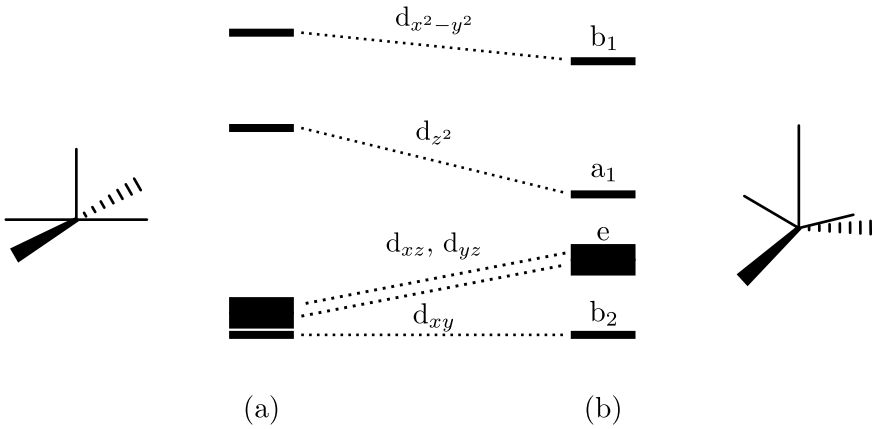

Figure 5.5: The orbital correlation diagram for (a) a square pyramid (C_{4v}) and (b) a distorted square pyramid (C_{2v}).

copper square pyramidal sites. Indeed, the apical elongation and angle distortion are less pronounced than in the $Cu_2P_2O_7$ structure, as illustrated by Figure 5.4. The five-fold site is closer to C_{4v} symmetry than C_{2v} symmetry (Figure 5.5). The d_{z^2} orbital is therefore destabilised while $d_{x^2-y^2}$ is only slightly destabilised. The d_{xy}, d_{xz} and d_{yz} orbitals see their energy leveled with each other. Consequently, ^2E and $^2B_1$ split further

apart while $^2A_1$ and $^2B_1$ come closer, giving the split bands observed.

5.6 Conclusion

Both $SrCuP_2O_7$ and $CaCuP_2O_7$ have been characterised and their absorption properties have been described.

As suspected from the previous section, copper in five-fold sites gives rise to an intense absorption due to the lack of inversion symmetry in the coordination polyhedron. The absorption band could be shifted related to the second cation situated in the structure. It became clear that the change of the shape of the coordination sphere of the Cu^{2+} ions has a strong influence on the absorption properties, and could be influenced by neighbouring structural changes due to the Sr^{2+} or Ca^{2+} ions. Such effects could be even stronger if the second metal element is located on the same crystallographical site as the Cu ions.

Therefore in the following sections, systems forming solid solutions are investigated.

CHAPTER 6

DI-CATION PYROPHOSPHATES

In general phosphates have great capacity to form solid solutions and accept substitute elements [86–88].

In addition to $SrCuP_2O_7$ and $CaCuP_2O_7$, where the two different cation types occupy two crystallographically different sites, another structure type was observed for $MgCuP_2O_7$ [82]. In this alternative structure, copper and magnesium form a solid solution with both metal ions situated on the same crystallographical site, in a distorted octahedron. Although *d-d* transitions resulting from octahedrally surrounded metal ions are sensibly weaker compared to their counterparts resulting from metal ions in five-fold surroundings, their absorption intensities are remarkably influenced by the vibration of the site. This phenomenon has been described in the previous chapters.

Introducing another metal ion into the same crystallographical site as copper should therefore have a beneficial effect on the absorption intensities.

In this chapter, $(Mg,Cu)_2P_2O_7$ and $(Zn,Cu)_2P_2O_7$ solid solutions are studied to investigate the effect of the two different additional cations on the copper site.

6.1 Magnesium Copper Pyrophosphate

6.1.1 Introduction

This divalent metal ion diphosphate series has been studied by *Boukhari et al.* [82] and was described as structurally related to the *thortveitite* structure discussed in Chapter 1.

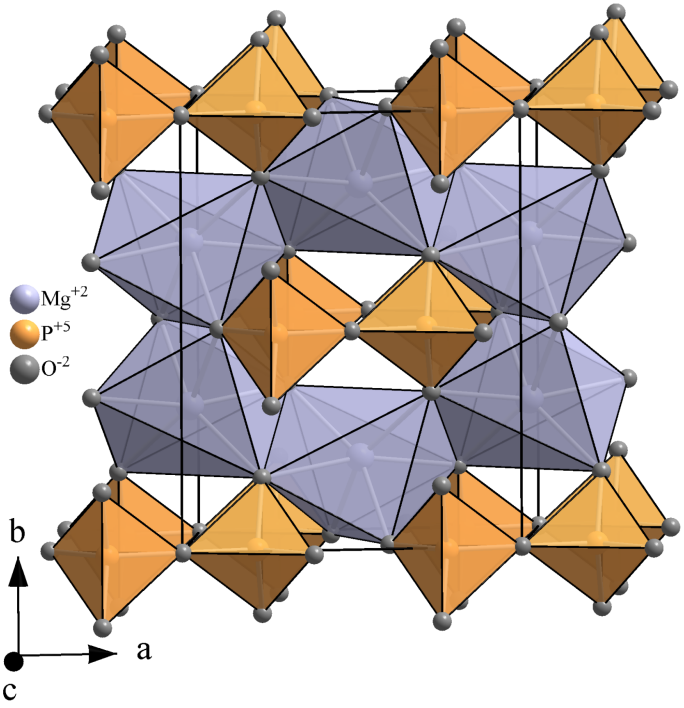

Figure 6.1: Projection along the c axis of the β-$Mg_2P_2O_7$ structure. The PO_4 groups are shown as orange tetrahedra and the octahedral arrangement around the Mg atoms is shown in purple [89].

By comparison with the heavier alkaline metal ions previously discussed, $Mg_2P_2O_7$ and $Cu_2P_2O_7$ adopt the same high temperature β-forms with a monoclinic cell ($C2/m$) (Figure 6.1) and the cations are situated in octahedral sites. The phosphate ligands are similar to those described in $SrCuP_2O_7$ and $CaCuP_2O_7$ and are constituted by two PO_4 units connected through one shared oxygen to form $P_2O_7^{4-}$ tetrahedral pairs.

Although the solid solution has been described, it is not known how distorted the

octahedral site is. It is therefore valuable to obtain more information on these materials to determine the effect of solid solution on the behaviour of copper(II) *d* - *d* transition.

6.1.2 Synthesis

The $Mg_{(2-x)}Cu_xP_2O_7$ (x = 0.4, 0.8, 1, 1.2 and 1.6) solid-solutions were prepared using stoichiometric amounts of $(NH_4)_2HPO_4$, MgO and CuO. These oxides were ground with a pestle and mortar. The mixture was thoroughly homogenized using a pestle and mortar and heated up slowly in an alumina crucible from room temperature to 500 °C (ramp 0.4 °C min^{-1}, temperature held for 15 hours) to allow the decomposition of diammonium phosphate. Taken out and pressed into a pellet, each sample was sintered at 900 °C in a box furnace for 24 hours. The light blue coloured pellets were then removed from the furnace, allowed to cool in the air and ground to a fine powder.

The pellets obtained from the described procedure showed some patches of differing colours. Several cycles of regrinding, forming pellets and reheating did not improve the homogeneity of the samples and the powder X-ray diffraction patterns evidenced the presence of unreacted MgO.

Another attempt to produce the $Mg_{(2-x)}Cu_xP_2O_7$ solid-solutions, used dried $MgCO_3$ as reactant instead of MgO. The mixtures were heated up slowly from room temperature to 500 °C (ramp 0.4 °C min^{-1}) and held at this temperature for 24 hours. Allowed to cool to room temperature, each sample was ground and pressed into a pellet, then fired at 900 °C in a box furnace for a further 24 hours. Pellets obtained through this procedure presented an homogeneous colour.

These samples were analysed by powder X-ray diffraction and UV to near-infrared spectroscopy. The PXD data showed presence of the main $Mg_{(2-x)}Cu_xP_2O_7$ phase.

6.1.3 Powder X-ray diffraction

PXD data were collected overnight on a Philips PANalytical X'Pert PRO MPD diffractometer using the method outlined in Chapter 2.

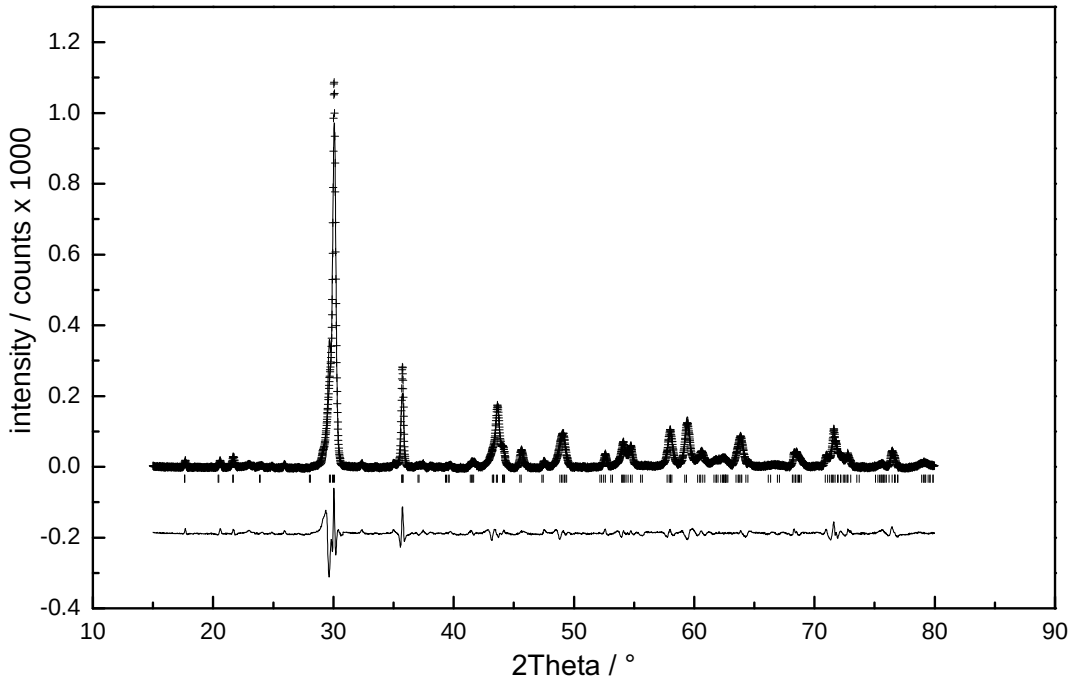

Figure 6.2: *Le Bail* fit of $MgCuP_2O_7$. Observed data points are shown as crosses and the calculated pattern is shown as a solid line. The difference between the calculated and observed patterns is shown underneath. The position of the peaks are marked by the row of vertical lines.

For all samples, the main reflection at around $2\theta = 30^\circ$ shows an intense and broad peak while other reflections are undefined. This problem prevents a full *Rietveld* refinement. However, *Le Bail* fits were performed for each sample in order to investigate the phases. Using β-$Mg_2P_2O_7$ from *Calvo* [89] as the starting model, the unit cell parameters were allowed to refine to match the reflections. The peak shapes were refined at the same time. Two impurities phases were fitted as well: $Mg_3(PO_4)_2$ for the phase with the highest content of magnesium (Figure A.2) and $Cu_3(PO_4)_2$ for the phase with

Table 6.1: Unit cell parameters and refinement statistics for the $Mg_{(2-x)}Cu_xP_2O_7$ series (e.s.d.s given in parenthesis).

Space group $C2/m$.

Compounds	a	b	c	β	R_p	R_{wp}
$Mg_{0.4}Cu_{1.6}P_2O_7$	6.77298(31)	8.1439(5)	4.55058(27)	108.349(5)	2.62	4.01
$MgCuP_2O_7$	6.6425(8)	8.1919(6)	4.5276(5)	106.529(5)	3.08	5.42
$Mg_{1.6}Cu_{0.4}P_2O_7$	6.57159(29)	8.2676(5)	4.50673(25)	105.263(4)	2.48	3.85

the highest content of copper (Figure A.1). The cell parameters (Table 6.1) were found to respect the trend described by *Boukhari et al.* proving the presence of the wanted phase.

6.1.4 UV to Near-infrared Spectroscopy

Solid state UV to near-infrared data were collected on undiluted samples according to the method outlined in Chapter 2. Each member of this series shows a single absorption band centred at 920 nm (Figure 6.3) which is attributed to the $^2E_g \leftarrow {}^2B_{1g}$ electronic transition of copper in a tetragonally distorted octahedral environment. However, the intensity of absorption is low with a maximum of 1.5 units which tends to prove that the vibronic coupling is not strong enough to totally overcome the *Laporte* rule. From this low intensity of the absorption band, it appears that copper is situated in a nearly perfect square planar surrounding formed by the equatorial oxygen atoms of a tetragonally distorted octahedron with elongated bonds perpendicular to this plane [90]. It is assumed that the strong ionic character of magnesium stabilises the P_2O_7 units, which could explain the position of copper in a nearly perfect tetragonally distorted octahedron.

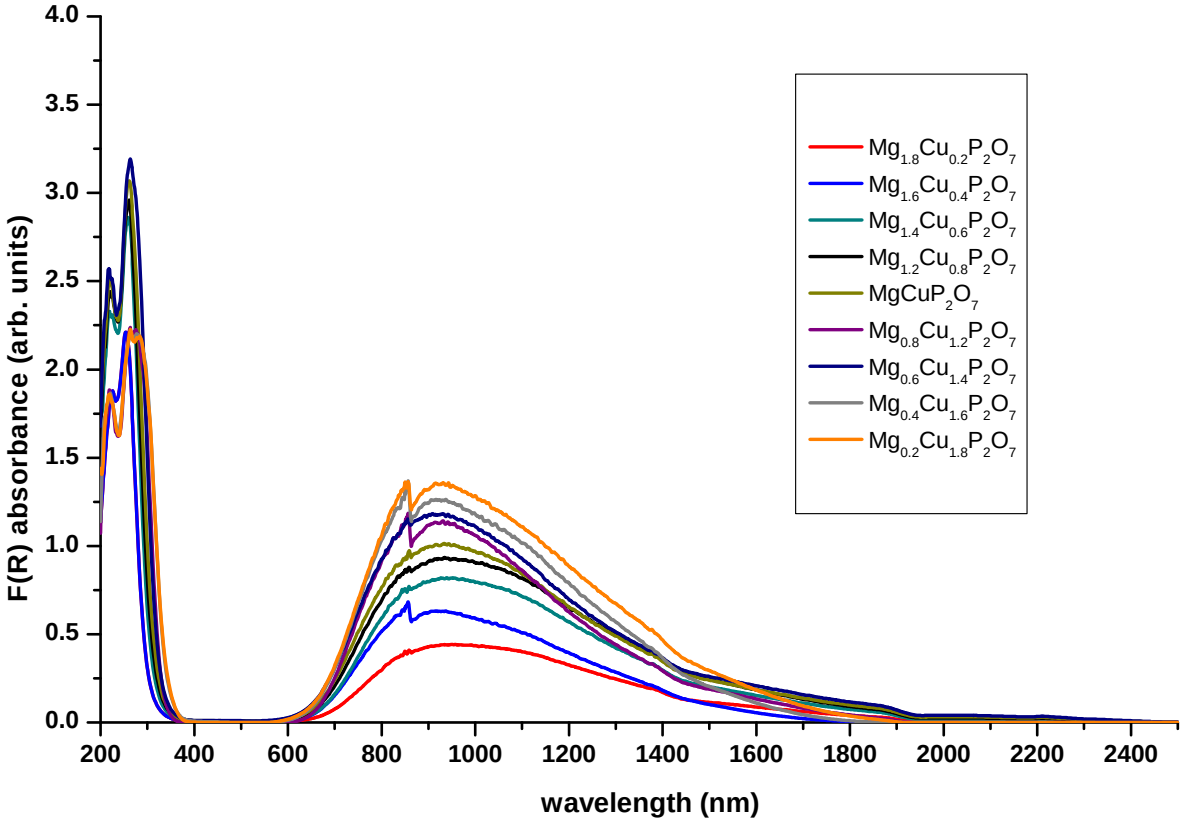

Figure 6.3: UV to near-infrared spectra of the magnesium copper pyrophosphate series

6.1.5 Conclusion

The relatively low absorption of this series is not interesting for further study regarding applications, therefore a full structural examination was not conducted. However, it confirmed the behaviour of copper(II) in an octahedral site connected to phosphate ligands and the effect of distortion of this site.

Although the choice of a structure exhibiting six fold oxygen coordination around the copper ions and in addition forming a solid solution with Mg^{2+} on the copper site shows promising results with the absorption band lying essentially in the near-infrared, the intensity of the absorption band is still too low. Therefore it seems necessary to have copper in a more strongly distorted surrounding to generate a vibronic

coupling large enough to bypass the selection rules.

6.2 Zinc Copper Pyrophosphate

6.2.1 Introduction

A pigment like zinc phosphate (*e.g.* $Zn_2P_2O_7$) which has a white colour with low opacity, will be of interest as an additive to paint or plastics without degrading their colour properties or their transparencies. This low opacity was one of the main interests in using phosphate pigments since the functional pigment developed had to be transparent to visible light.

Zinc copper diphosphate was structurally studied by *El Maadi et al.* [91]. They found that the solid solution $Zn_{(2-x)}Cu_xP_2O_7$ is stable for $0.15 \leqslant x \leqslant 1.95$ and crystallises in the *thortveitite* type structure.

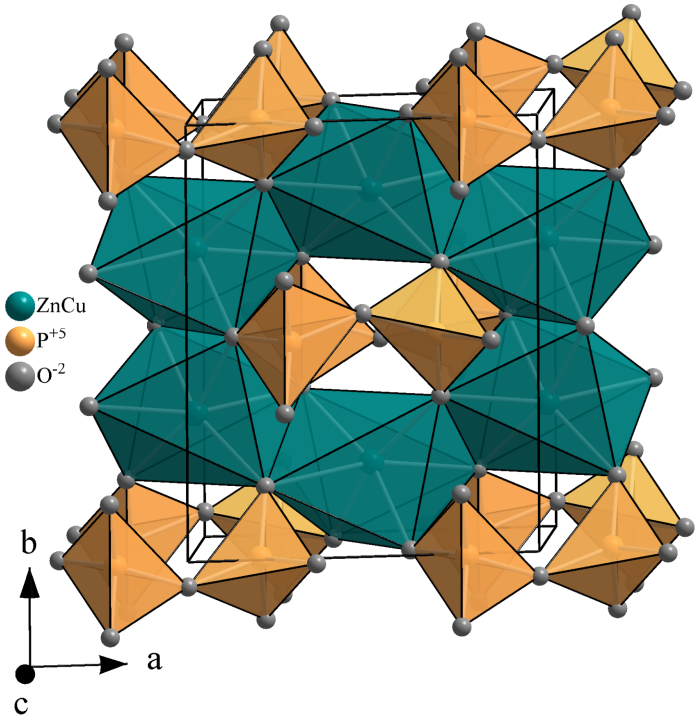

Figure 6.4: Projection along the c axis of the $ZnCuP_2O_7$ structure. The P_2O_7 groups are shown as orange tetrahedra and the octahedral arrangement around the Zn/Cu atoms is shown in dark green.

The main difference from the structure of $Sc_2Si_2O_7$ discussed in Chapter 1 is the

oxygen linking both PO_4 tetrahedral groups. In the *thortveitite* structure, it is recognised that this oxygen is aligned with the phosphorus atoms situated in these tetrahedra [34]. In the $(Zn,Cu)_2P_2O_7$ solid solution, this alignment is broken and the bridging oxygen is found randomly situated between two positions. This is described crystallographically by an half occupied oxygen position which has been drawn in Figure 6.4 in an arbitrary way.

The distortion of these P_2O_7 units from a symmetrically aligned arrangement should contribute to a more distorted basal plane of the MO_6 octahedra compared to the previously discussed $(Mg,Cu)_2P_2O_7$, resulting in a more intense absorption band. It was therefore of interest for this study to investigate this series.

6.2.2 Synthesis

A range of samples of the series of $Zn_{(2-x)}Cu_xP_2O_7$ (x = 0, 0.2, 0.4, 0.6, 0.8, 1, 1.2, 1.4, 1.6, 1.8 and 2) was prepared using a conventional solid state synthesis method. ZnO was ground with $(NH_4)_2HPO_4$ and CuO in the relevant molar ratio, with a pestle and mortar and slowly heated up to 500 °C (at a ramp rate of 0.4 °C min^{-1}) and held at that temperature for 15 hours. Pressed into pellets the samples were then sintered at 900 °C in a box furnace for 24 hours. The obtained light blue coloured materials were then removed from the furnace, left to cool down to room temperature in the air and ground into a fine powder.

The samples obtained from this direct route were not homogeneous. The preliminary PXD data showed the presence of a single phase but the samples exhibited differently coloured crystallites. The high crystallinity of this material (Figure 6.5) using this route was supposed to cause the disturbance. A sol-gel route was thus used instead to prepare homogeneous samples.

The starting materials ($(NH_4)_2HPO_4$, ZnO and CuO) were dissolved separately in the minimum of water/HNO_3 until a clear solution was obtained. Solutions were mixed together and heated up to 60 °C until a gel was formed. This gel was main-

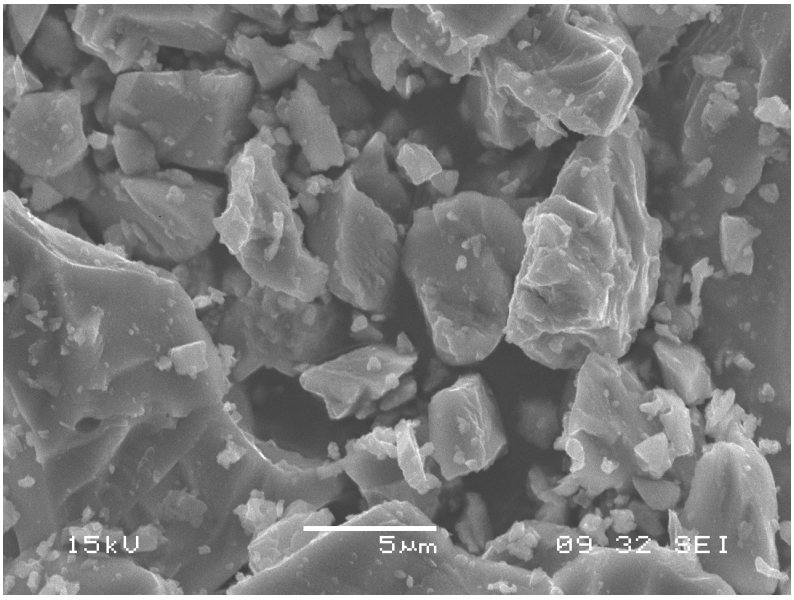

Figure 6.5: SEM images of $ZnCuP_2O_7$ synthesized using the conventional solid state method.

tained at this temperature for an hour and then allowed to dry out. The mixture was heated up to 350 °C and kept at that temperature overnight for complete decomposition and evaporation of NO_2. The light blue powder obtained was heated up slowly to 500 °C (ramp 0.4 °C min^{-1}), kept at this temperature for another 15 hours and then was ground and sintered at 900 °C in an open box furnace. With this method the homogeneity of the material with regard to the colour was much better with visibly much smaller crystal size.

These samples were analysed by powder X-ray diffraction and powder neutron diffraction, EXAFS, UV-Visible spectroscopy and microscopy. Preliminary PXD data showed that the obtained single phase is isostructural to $ZnCuP_2O_7$ [91] or β-$Cu_2P_2O_7$ [92], called the high temperature form.

6.2.3 Structural Refinement

Powder X-ray diffraction

PXD data were collected overnight on a Siemens D5000 diffractometer using the method outlined in Chapter 2. *Rietveld* structural refinements were performed using the GSAS program.

The starting model employed in the refinements was taken from *El Maadi et al.* [91]. First the background was modelled, then lattice parameters were refined in order to match the peak positions. Peak profiles were also refined and atomic positions varied. Finally, isotropic thermal factors and site occupancies for zinc and copper were added to the refinement. Since no impurity phases could be detected, linear constraints over

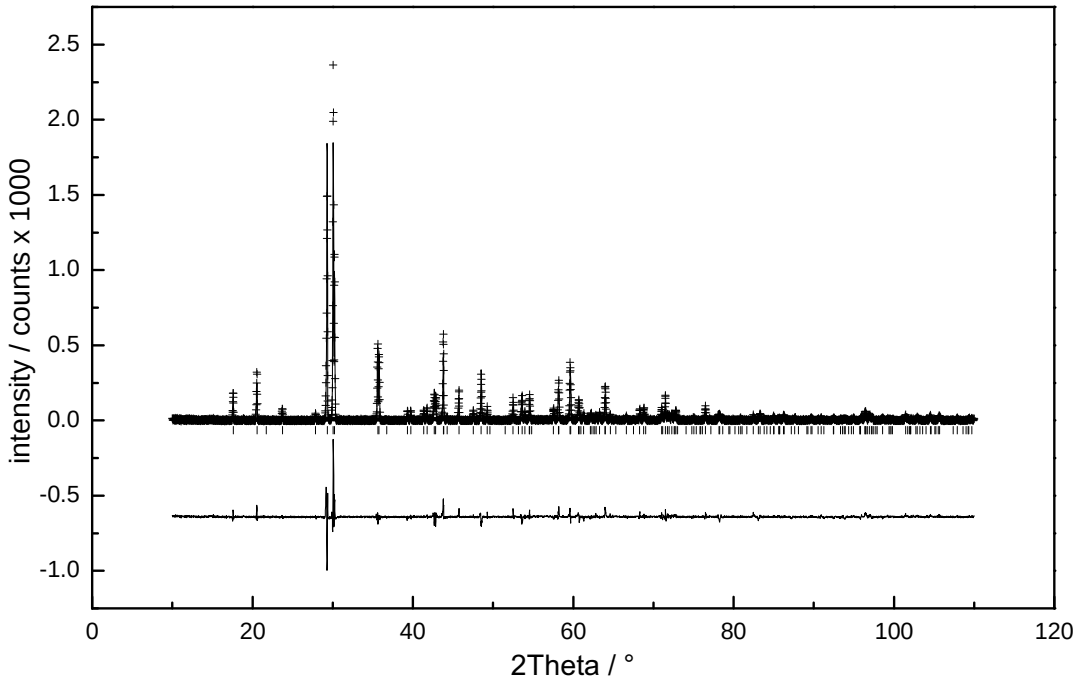

Figure 6.6: *Rietveld* refinement profile fit of $ZnCuP_2O_7$. Observed data points are shown as crosses and the calculated pattern is shown as a solid line. The difference between the calculated and observed patterns is shown underneath. The position of the peaks are marked by the row of vertical lines.

the stoichiometry of these two elements were added.

For each sample of this series, the peak intensities were incorrect to a certain extent (Figure 6.6), although the peak positions were matching suggesting that a second phase might be present.

This suggestion was investigated. Since no reflections other than the peaks of the main phase were detected from the pattern, to exist, the second phase would have to have a similar or related space group. Zinc phosphate related phases ($Zn_2P_2O_7$, $Zn_3(PO_4)_2$, $Zn(PO_3)_2$) and copper phosphate related phases ($Cu_2P_2O_7$, $Cu_2P_4O_{12}$, $Cu_3(PO_4)_2$) were added in turn into the refinement, but none of these phases would account for the difference in intensities between the calculated and experimental pattern without adding other peaks.

Preferred orientation was addressed through careful regrinding and a rotating sample holder; none of the reflections had a significant change in intensity therefore ruling out this suggestion.

Another possibility which may be wise to explore is the anisotropic thermal displacement of the atoms in this structure, in particular the oxygen atoms. However, due to the limitation of X-ray powder diffraction with regard to the light elements, further studies were caried out using neutron powder diffraction.

Powder neutron diffraction

PND data were collected on D1A at the Institut Laue-Langevin on *ca.* 5 g samples at room temperature over a period of 7 hours for each sample. *Rietveld* structural refinement was carried out using the structural model obtained from the X-ray diffraction data. Zero correction, background coefficients and peak profiles were first evaluated then lattice parameters were refined. The refinement converged nicely, atom positions were allowed to vary with a linear constraint on the Zn/Cu shared site. Isotropic thermal factors were added finally and the best refinement was achieved once all parameters could be varied altogether without diverging. Similarly to X-ray powder diffraction, intensities were not modelled correctly. On the other hand, introducing

anisotropic thermal factor seems to efficiently lower the R-factors and the fit improved matching all intensities (Figures 6.7 and B.1 to B.9). Full refined crystallographic data can be found in the appendix (Tables B.1 to B.9).

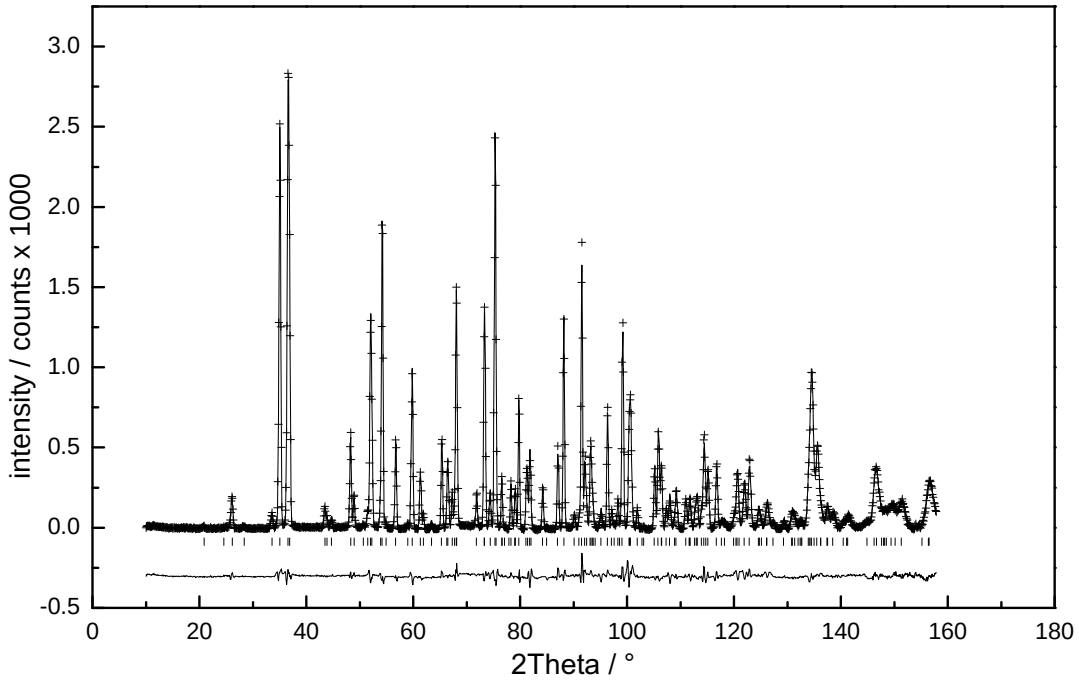

Figure 6.7: *Rietveld* refinement profile fit of $ZnCuP_2O_7$. Observed data points are shown as crosses and the calculated pattern is shown as a solid line. The difference between the calculated and observed patterns is shown underneath. The position of the peaks are marked by the row of vertical lines.

Table 6.2: Unit cell parameters and refinement statistics for the $Zn_{(2-x)}Cu_xP_2O_7$ series (e.s.d.s given in parenthesis).

Space group $C2/m$.

Compounds	a	b	c	β	Cell Volume (Å^3)	χ^2	R(F^2)	R_p	R_{wp}
$Zn_{0.2}Cu_{1.8}P_2O_7$	6.84171(10)	8.13761(10)	4.57254(6)	109.0312(8)	240.662(6)	6.588	4.90	3.45	4.46
$Zn_{0.4}Cu_{1.6}P_2O_7$	6.81279(12)	8.15452(14)	4.56640(7)	108.6513(8)	240.364(7)	7.339	4.22	3.44	4.48
$Zn_{0.6}Cu_{1.4}P_2O_7$	6.78572(15)	8.17068(17)	4.56013(9)	108.2762(10)	240.078(9)	10.330	4.46	3.46	4.72
$Zn_{0.8}Cu_{1.2}P_2O_7$	6.75802(17)	8.18649(20)	4.55309(11)	107.8859(12)	239.723(10)	13.520	5.68	4.22	5.75
$ZnCuP_2O_7$	6.73404(18)	8.20543(20)	4.54834(11)	107.4967(12)	239.694(11)	8.067	5.49	3.66	4.72
$Zn_{1.2}Cu_{0.8}P_2O_7$	6.71006(23)	8.22309(26)	4.54329(15)	107.0944(17)	239.612(14)	14.960	4.86	4.56	6.32
$Zn_{1.4}Cu_{0.6}P_2O_7$	6.68532(22)	8.24006(25)	4.53785(14)	106.6827(16)	239.457(13)	14.220	4.66	4.65	6.27
$Zn_{1.6}Cu_{0.4}P_2O_7$	6.66383(23)	8.25685(28)	4.53426(16)	106.2831(18)	239.478(15)	12.310	4.67	4.72	6.25
$Zn_{1.8}Cu_{0.2}P_2O_7$	6.6596(5)	8.2711(4)	4.53607(28)	106.049(4)	240.119(27)	6.263	11.45	6.43	8.28

Table 6.3: Derived bond distances (Å) for the $Zn_{(2-x)}Cu_xP_2O_7$ series (e.s.d.s given in parenthesis).

M = Zn/Cu.

Distances	$Zn_{0.2}Cu_{1.8}$	$Zn_{0.4}Cu_{1.6}$	$Zn_{0.6}Cu_{1.4}$	$Zn_{0.8}Cu_{1.2}$	ZnCu	$Zn_{1.2}Cu_{0.8}$	$Zn_{1.4}Cu_{0.6}$	$Zn_{1.6}Cu_{0.4}$	$Zn_{1.8}Cu_{0.2}$
M_M	3.061(3)	3.063(3)	3.081(3)	3.080(4)	3.088(4)	3.108(5)	3.111(6)	3.120(7)	3.115(14)
M_O1	1.991(1)	1.995(1)	2.006(2)	2.008(2)	2.015(2)	2.027(3)	2.031(3)	2.037(3)	2.044(7)
M_O1	1.991(1)	1.995(1)	2.006(2)	2.008(2)	2.015(2)	2.027(3)	2.031(3)	2.037(3)	2.044(7)
M_O2	2.592(2)	2.569(1)	2.550(2)	2.527(2)	2.509(2)	2.488(2)	2.459(3)	2.441(3)	2.442(6)
M_O2	2.592(2)	2.569(1)	2.550(2)	2.527(2)	2.509(2)	2.488(2)	2.459(3)	2.441(3)	2.442(6)
M_O2	1.933(2)	1.942(1)	1.949(2)	1.957(2)	1.966(2)	1.976(3)	1.988(3)	1.995(3)	2.010(7)
M_O2	1.933(2)	1.942(1)	1.949(2)	1.957(2)	1.966(2)	1.976(3)	1.988(3)	1.995(3)	2.010(7)

6.2.4 UV to Near-infrared spectroscopy

Solid state UV visible data were collected on undiluted samples according to the method outlined in Chapter 2. As expected from a Cu^{2+} ion in a distorted octahedral site, a single absorption band is present, centred at 950 nm (Figure 6.8). With the increasing quantity of copper in the structure, absorption increases steadily with virtually no shift of the absorption peak to a lower or higher wavelength. This observation is correlated to the colour of the samples being light bluish through the entire series, becoming slightly more vivid at higher copper content.

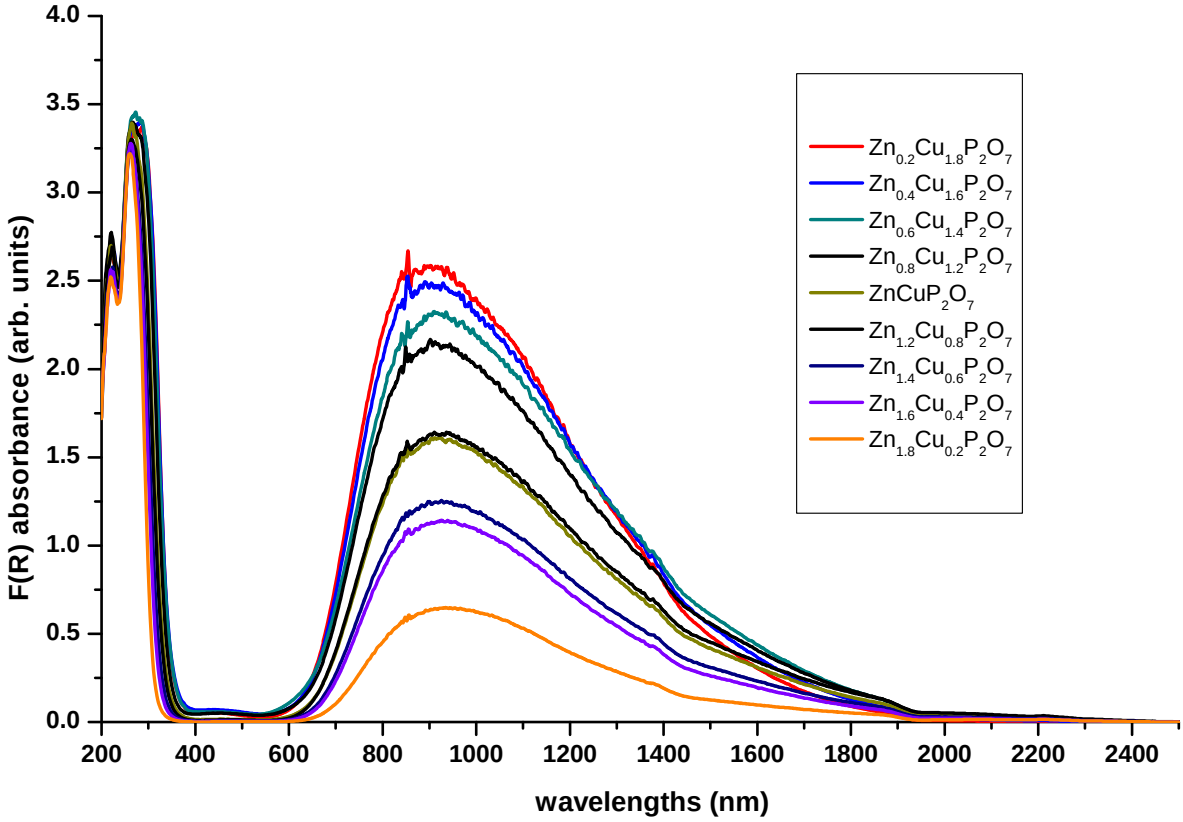

Figure 6.8: UV to near-infrared spectra of zinc copper pyrophosphate series

Quantitative interpretation of UV to near-infrared spectra should be undertaken with care, notably because the size of the particles plays a certain role. However, it is noteworthy to observe the trend (Figure 6.9). Compared to the $Mg_{(2-x)}Cu_xP_2O_7$ se-

ries which is known to be structurally related to the *thortveitite* family, the absorption band is identically situated, centred at 950 nm. However in the case of Zn/Cu it is much more intense.

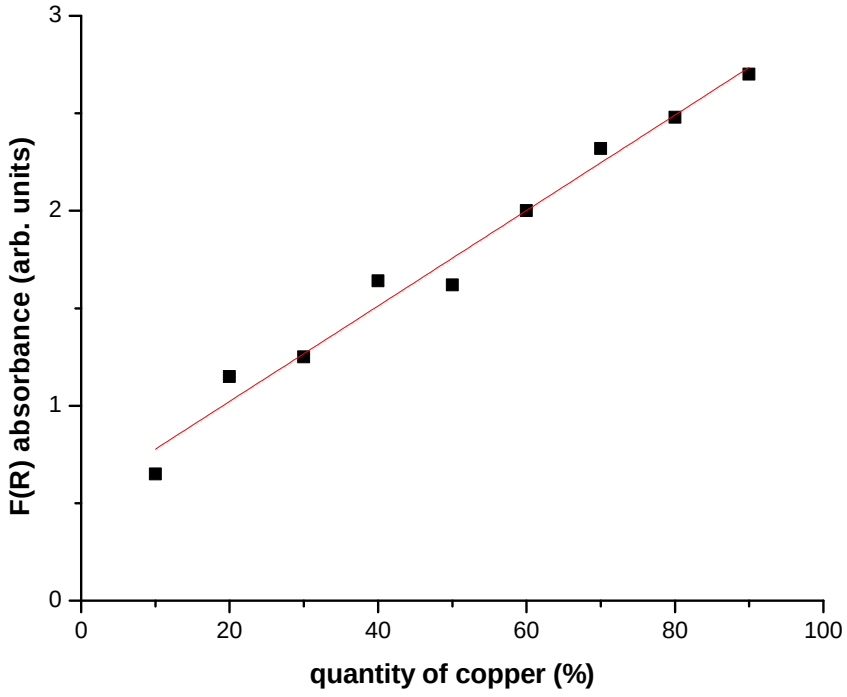

Figure 6.9: F(R) Absorbance versus quantity of copper in the structure

6.2.5 EXAFS

Zinc and copper are very difficult to differentiate using either X-ray or neutron diffraction. Indeed, X-ray powder diffraction is a technique whereby X-rays interact with the electrons surrounding the nucleus of an atom. Zinc and copper being neighbours in the Periodic Table, the difference of one electron is not enough to differentiate them. In the case of neutron diffraction, it is necessary to compare the scattering lengths of these atoms which is 5.680 fm for zinc and 7.718 fm for copper [93]. Althought these values show they should be fully distinguished, being situated at the same position prevent

any reflections to give any idea of the local environment.

In order to obtain further information about their respective average local environment, the EXAFS technique was therefore the method of choice. Zinc and copper K-edge data were collected on diluted samples (*ca.* 10 wt.% in PVA) in transmission mode on Station 9.1 at the Daresbury laboratories as described in Chapter 2. Three scans were performed for each sample and averaged to improve the signal to noise ratio.

Copper K-edge

The initial EXAFS model was taken from parameters obtained from the powder neutron diffraction refinement. The first shell to be modelled was the one consisting of four equatorial oxygen atoms. Then the two axial oxygen atoms were taken into account, introducing the *Jahn Teller* distortion undergone by the copper octahedral centred site into the model. A third shell was then added to the model to describe the Cu-M (M = Zn/Cu) interaction. Addition of a fourth shell did not improve the quality of fit.

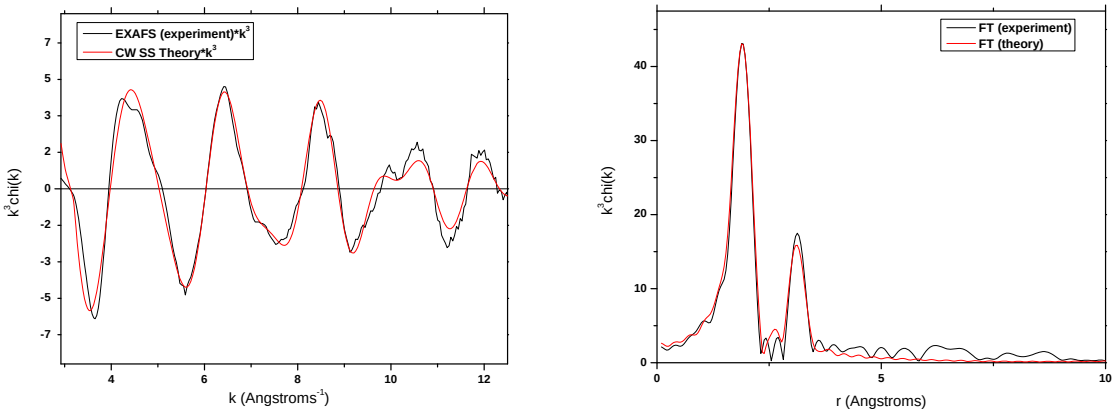

(a) *(b)*

Figure 6.10: EXAFS plot *(a)* and Fourier Transform EXAFS plot *(b)* for the $ZnCuP_2O_7$ copper K-edge.

The refinement was carried out for each sample with a good fit. An example of the observed and calculated background subtracted EXAFS and Fourier transformed EXAFS is shown in figure 6.10.

Table 6.4 displays bonds lengths for Cu–O_{ax}, Cu–O_{eq}. As suspected from the neutron refinement, the octahedral distortion is conspicious, but the difference between the Cu–O_{ax} and Cu–O_{eq} bond lengths remains constant through the entire series (approximately ~0.3 Å).

Table 6.4: Copper K-edge EXAFS refinement for $Zn_{(2-x)}Cu_xP_2O_7$ series (e.s.d.s given in parenthesis).

	Shell	CN	Distance / Å	Debye-Waller factor	EXAFS R factor
$Zn_{0.2}Cu_{1.8}$	Cu–O_{eq}	4	1.952(2)	0.015(1)	25.35
	Cu–O_{ax}	2	2.346(8)	0.028(5)	
$Zn_{0.4}Cu_{1.6}$	Cu–O_{eq}	4	1.963(2)	0.015(1)	23.2
	Cu–O_{ax}	2	2.314(6)	0.027(4)	
$Zn_{0.6}Cu_{1.4}$	Cu–O_{eq}	4	1.966(2)	0.016(1)	25.11
	Cu–O_{ax}	2	2.312(7)	0.026(4)	
$Zn_{0.8}Cu_{1.2}$	Cu–O_{eq}	4	1.967(3)	0.015(1)	23.76
	Cu–O_{ax}	2	2.313(6)	0.026(4)	
ZnCu	Cu–O_{eq}	4	1.968(2)	0.015(1)	22.81
	Cu–O_{ax}	2	2.315(7)	0.027(4)	
$Zn_{1.2}Cu_{0.8}$	Cu–O_{eq}	4	1.977(3)	0.016(1)	23.4
	Cu–O_{ax}	2	2.308(6)	0.025(4)	
$Zn_{1.4}Cu_{0.6}$	Cu–O_{eq}	4	1.972(3)	0.016(1)	28.09
	Cu–O_{ax}	2	2.322(8)	0.026(5)	
$Zn_{1.6}Cu_{0.4}$	Cu–O_{eq}	4	1.968(3)	0.016(1)	25.29
	Cu–O_{ax}	2	2.320(8)	0.028(5)	
$Zn_{1.8}Cu_{0.5}$	Cu–O_{eq}	4	1.966(3)	0.011(1)	22.71
	Cu–O_{ax}	2	2.295(11)	0.037(9)	

Zinc K-edge

Similarly to the copper K-edge refinement, the initial model was taken from powder neutron diffraction. However the model of a 4+2 distorted octahedral arrangement did not fit the EXAFS data correctly resulting in too high Debye-Waller factor values. The number of oxygen atoms in both shells were refined. The resulting stable model was a 5+1 configuration which matched perfectly the Fourier Transformed EXAFS (Figure 6.11).

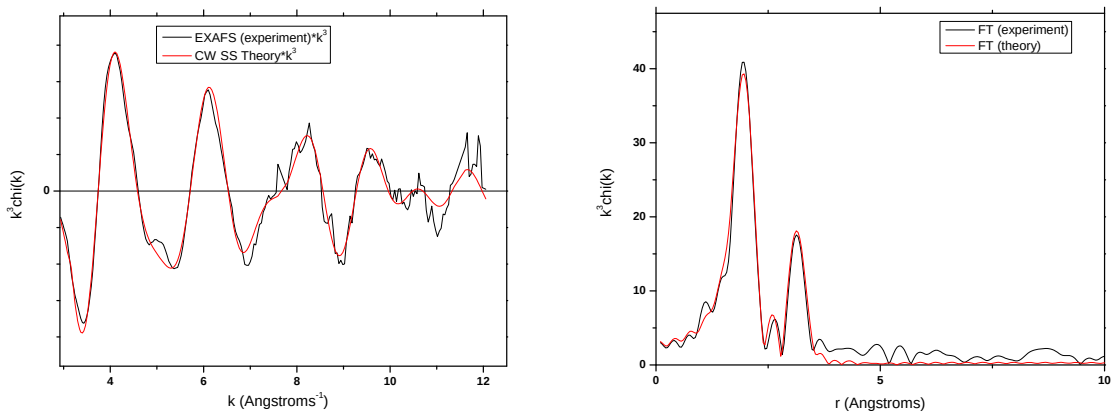

(a) *(b)*

Figure 6.11: EXAFS plot *(a)* and Fourier Transform EXAFS plot *(b)* for $ZnCuP_2O_7$ zinc K-edge.

The bond length for Zn–O_{ax} and Cu–O_{eq} are shown in Table 6.5.

Table 6.5: Zinc K-edge EXAFS refinement for $Zn_{(2-x)}Cu_xP_2O_7$ series (e.s.d.s given in parenthesis).

	Shell	CN	Distance / Å	Debye-Waller factor	EXAFS R factor
$Zn_{0.2}Cu_{1.8}$	$Zn–O_{eq}$	5	2.013(3)	0.020(1)	14.18
	$Zn–O_{ax}$	1	2.315(12)	0.028(7)	
$Zn_{0.4}Cu_{1.6}$	$Zn–O_{eq}$	5	2.024(3)	0.019(1)	16.03
	$Zn–O_{ax}$	1	2.357(11)	0.021(4)	
$Zn_{0.6}Cu_{1.4}$	$Zn–O_{eq}$	5	2.030(3)	0.021(1)	15.83
	$Zn–O_{ax}$	1	2.356(9)	0.021(3)	
$Zn_{0.8}Cu_{1.2}$	$Zn–O_{eq}$	5	2.038(2)	0.021(1)	16.75
	$Zn–O_{ax}$	1	2.340(5)	0.011(2)	
ZnCu	$Zn–O_{eq}$	5	2.042(3)	0.022(1)	17.10
	$Zn–O_{ax}$	1	2.368(7)	0.015(3)	
$Zn_{1.2}Cu_{0.8}$	$Zn–O_{eq}$	5	2.043(3)	0.022(1)	17.81
	$Zn–O_{ax}$	1	2.352(6)	0.012(2)	
$Zn_{1.4}Cu_{0.6}$	$Zn–O_{eq}$	5	2.053(3)	0.027(1)	21.63
	$Zn–O_{ax}$	1	2.380(7)	0.014(2)	
$Zn_{1.6}Cu_{0.4}$	$Zn–O_{eq}$	5	2.058(3)	0.027(1)	18.48
	$Zn–O_{ax}$	1	2.394(7)	0.015(3)	
$Zn_{1.8}Cu_{0.5}$	$Zn–O_{eq}$	5	2.055(3)	0.022(1)	15.39
	$Zn–O_{ax}$	1	2.372(7)	0.016(3)	

6.2.6 Discussion

The values for the unit cell parameters from the X-ray and neutron data refinement correlate perfectly which confirms that the intensity difference between the observed and calculated pattern was solely due to the thermal motion, and in particular the thermal motion of the bridged oxygen linking the two PO_4 units as described by *Calvo*

for β-$Zn_2P_2O_7$ [94]. Indeed, concerning the X-ray experiment, the anisotropic thermal factors cannot be modelled.

The unit cell expands along the a axis and slightly less along the c axis (Figure 6.12), with addition of copper to the system. This is consistent with the axial distortion of the octahedral site extending in a direction parallel to the a axis with a small component on the c axis.

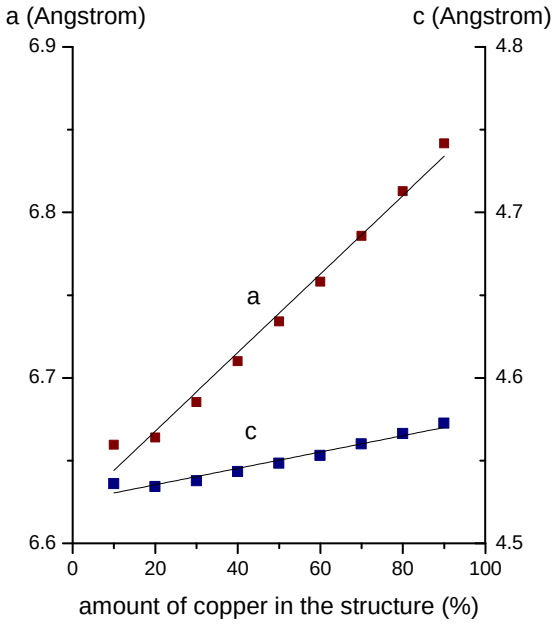

Figure 6.12: Dependence of a and c cell parameters from neutron powder diffraction of $(Zn,Cu)_2P_2O_7$ against the amount of copper incorporated in the structure.

Figure 6.13 shows the relative distortion of the octahedral mixed metal site. This is due to the *Jahn Teller* effect which is often the case for copper(II). On the other hand, such a distortion is unusual for zinc(II) which, having a d^{10} electron configuration, has all its orbitals fully occupied.

The spectroscopic data shows an absorption band centred at 950 nm. This confirms the presence of copper(II) in a distorted octahedral site, the band being attributed to the electronic transition $^2E_g \leftarrow {}^2B_{1g}$. However, the derived Cu–O_2 axial bond lengths (the axial bond distances) from neutron powder diffraction, indicate an elongation

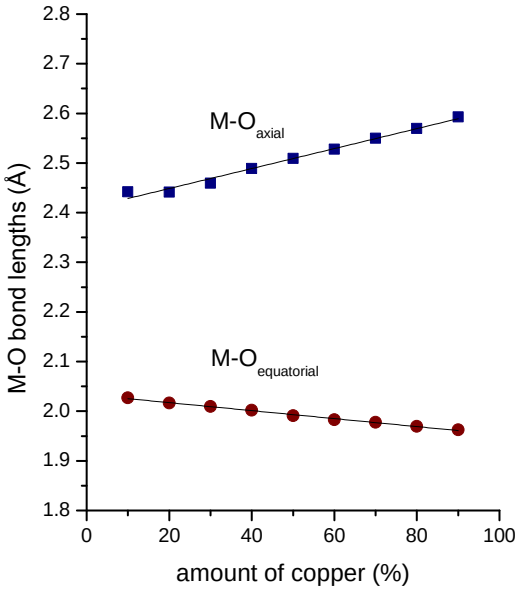

Figure 6.13: Variation of axial and equatorial bond distances, taken from neutron powder diffraction, in the mixed metal site against the amount of copper incorporated in the structure (M = Zn, Cu).

from 2.44 Å to 2.59 Å depending on the amount of copper introduced in the structure (Figure 6.13). The crystal field stabilisation is strongly dependent on the transition metal ion to ligand distance [95], the energy necessary for an electron to move from the ground state to the excited state increases with the tetragonal distortion. This elongation of the octahedron would be seen in the spectrum as a shift of the maximum of absorption towards lower wavelengths (blue shift). Since the absorption band is not shifted, the difference between axial bond length and equatorial bond length should remain constant.

Axial and equatorial bond distances derived from the copper K-edge corroborate this hypothesis with a constant difference of 0.3 Å across the entire series (Figure 6.14).

Bond distance values derived from the zinc K-edge on the other hand are very different, with a zinc atom found irregularly coordinated to six oxygen atoms, with five zinc oxygen bonds averaged through the series to ~2.04 Å while one zinc oxygen bond

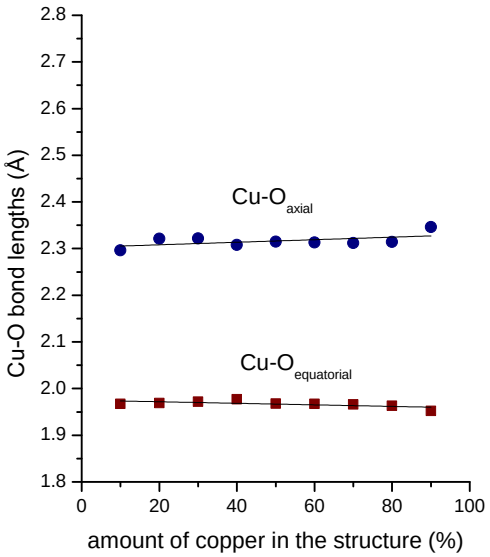

Figure 6.14: Variation of axial and equatorial bond distances in the mixed metal site against the amount of copper introduced into the structure, derived from the copper K-edge.

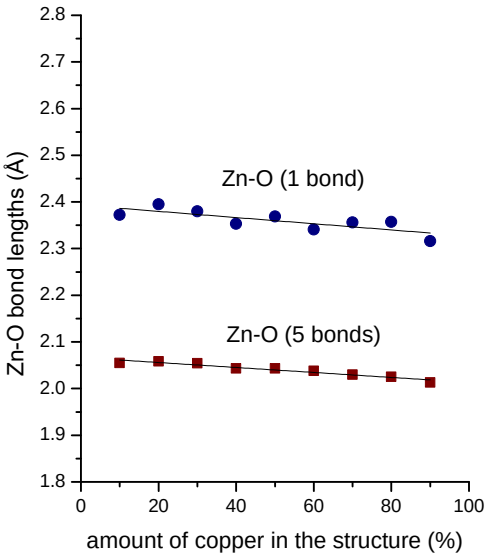

Figure 6.15: Variation of axial and equatorial bond distances in the mixed metal site against the amount of copper introduced into the structure, derived from the zinc K-edge.

distance is averaged to ~2.36 Å (Figure 6.15). From these values it can be assumed that the zinc atoms are situated in distorted octahedral sites with one axial bond length shorter than the other. This is consistent with a previous study on β-$Zn_2P_2O_7$ where Zn^{2+} was found displaced by about 0.3 Å from the middle of a line joining O_{ax} to its symmetrically equivalent atom generated by the two fold axis [94].

The $(Zn,Cu)_2P_2O_7$ solid solution is therefore more complex than described by *El Maadi et al.* [91]. Although the zinc and copper atoms share the same crystallographic site, their bonding situation is totally different. The behaviour of zinc atoms has been explained for β-$Zn_2P_2O_7$ by the constraints placed upon the position of the oxygen atoms by the requirements of their bonding to the phosphorus atom [94]. Copper atoms on the other hand are seen in the β-$Cu_2P_2O_7$ structure to accommodate this requirement by substantial deviation from a perfect octahedral coordination sphere

through the *Jahn Teller* effect and additional distortion of the square plane formed by the equatorial oxygen atoms [92]. This distortion of the basal plane is confirmed by the strong absorption intensity of the band centred at 950 nm.

In the $(Zn,Cu)_2P_2O_7$ structure, being closely related to both β-$Zn_2P_2O_7$ and β-$Cu_2P_2O_7$, the behaviour of both atom types is kept from these phases. The fact that no ordering is found is due to their similar ionic radii (0.73 Å for Cu^{2+} and 0.74 Å for Zn^{2+}) and chemical hardness (8.3 eV for Cu^{2+} and 10.8 eV for Zn^{2+} [96]).

6.2.7 Influence of Temperature of Synthesis on the Particle Size

As this study was driven toward the synthesis of a transparent pigment, investigation of the particle size has been conducted on the $ZnCuP_2O_7$ series.

In a polycrystalline material such as an inorganic pigment, the optical transparency is limited by the scattering of visible light due mostly to the size of the grain boundaries which separate tiny regions of crystalline order. To avoid any scattering of visible light to occur, the size of the grain boundaries has to be smaller than the wavelength of the transparent region. Since the size of the grain boundaries is directly related to the size of particles, a reduction of particle size below the wavelength of visible light should result in a translucent to transparent material. It has been commonly reported that the size of particles should be smaller than 50 nm [3].

In order to determine the influence of the synthesis temperature on the crystal size, one sample of $ZnCuP_2O_7$ was prepared following the procedure described earlier but for each 100 °C, starting at 200 °C, a small portion of this sample was collected for analysis. X-ray powder diffraction, UV Visible spectroscopy and microscopy techniques were used to monitor each step of the reaction.

According to the X-ray data collected (Figures 6.17 and 6.18), nucleation starts as early as 200 °C with small crystals formed considering the broadening of the diffraction lines. Then, from 200 °C to 500 °C the peak shapes remain the same suggesting that the product is formed without increase of the particle size. From 600 °C onwards, growth is starting as the diffraction lines sharpened until 800 °C. This observation is

supported by microscopy. At 700 °C, crystals are very small and aggregated while at 800 °C crystals are much more defined (Figure 6.16).

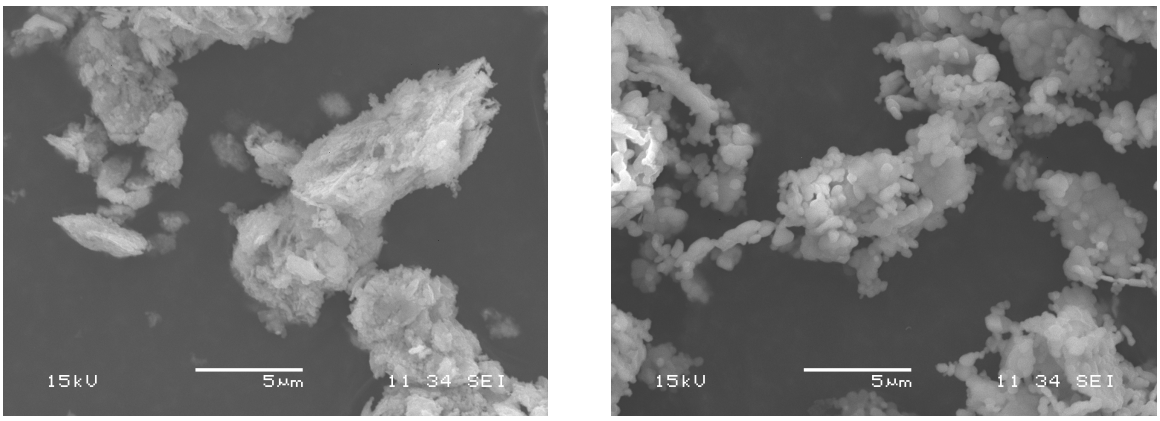

(a) *(b)*

Figure 6.16: SEM micrograph of $ZnCuP_2O_7$ sintered at *(a)* 700 °C and *(b)* 800 °C.

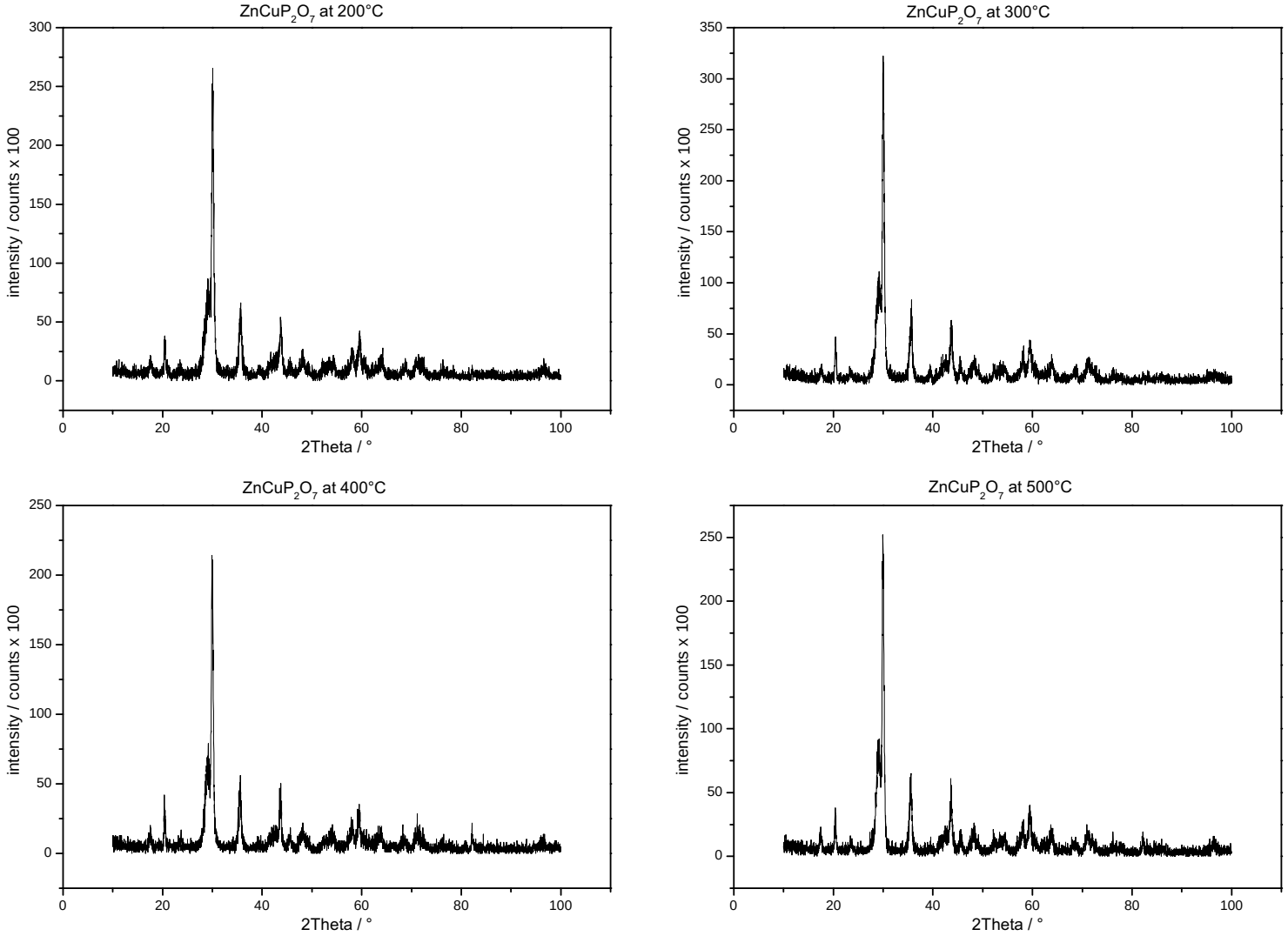

Figure 6.17: $ZnCuP_2O_7$ X-ray pattern from 200 °C to 500 °C.

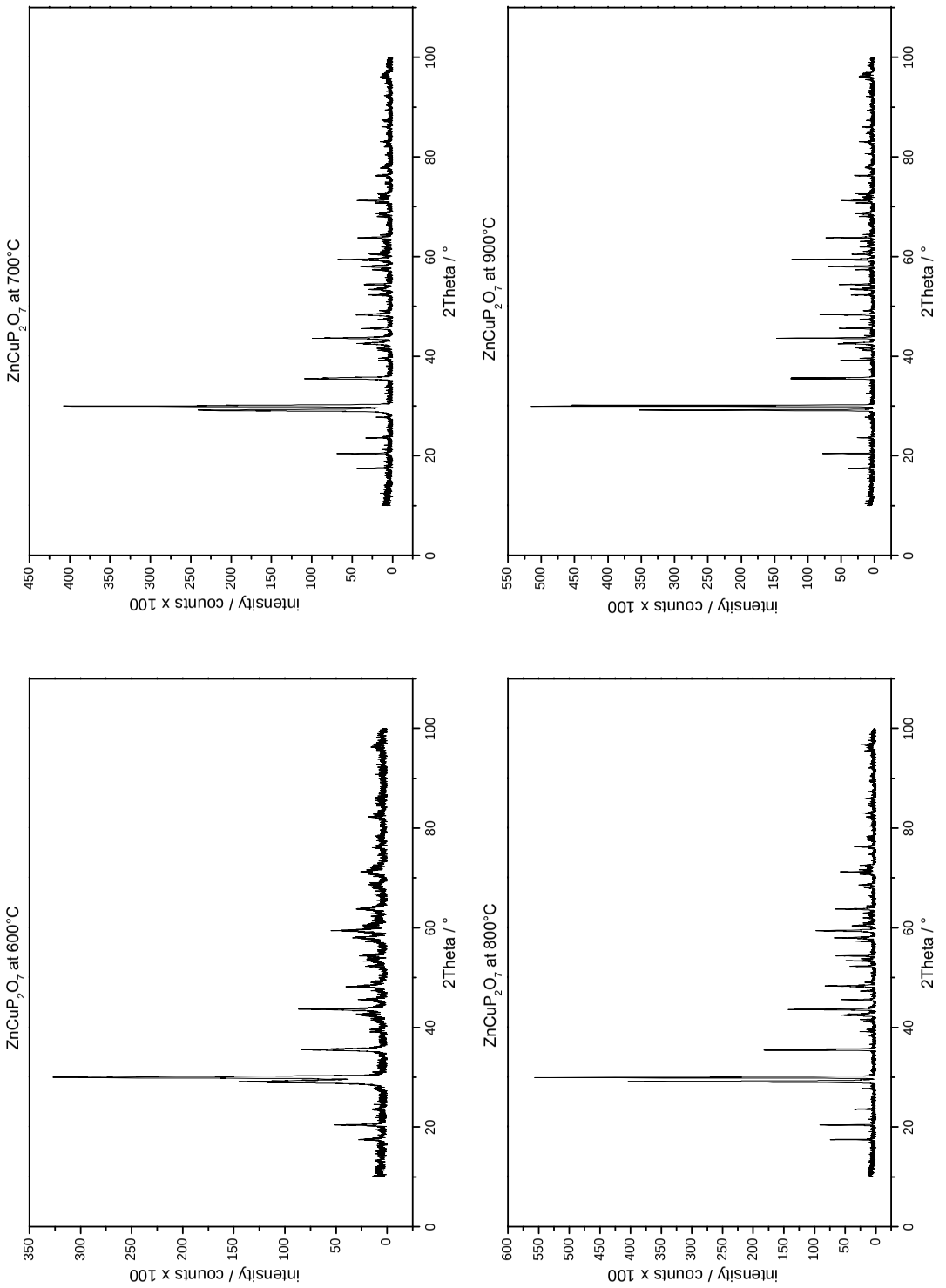

Figure 6.18: $ZnCuP_2O_7$ X-ray pattern from 600 °C to 900 °C.

6.2.8 Conclusion

The $(Mg,Cu)_2P_2O_7$ and $(Zn,Cu)_2P_2O_7$ systems have been studied with a full characterisation of the latter by PND and EXAFS.

Although these two series are closely related since they both crystallise in the *thortveitite* structure type and copper was found for both series in an elongated octahedral site, the intensity of their absorption differs greatly. This has been proven to result from a distortion which relaxes the *Laporte* selection rule giving a higher absorption.

In a phosphate environment, the elongated copper oxygen bonds of the octahedral coordination sphere should be in the order of 2.40 Å to obtain a peak maximum right after the visible region without greatly disturbing the colour of the substrate. In addition to this the octahedral site has to be heavily distorted to maintain a high vibronic coupling giving a high intensity of the absorption band.

The $(Zn,Cu)_2P_2O_7$ system has demonstrated both of these properties, in particular the $Zn_{0.6}Cu_{1.4}P_2O_7$ material which shows a good absorption intensity in the near-infrared and a light colour in the visible. However, an additional feature that should be further improved for that phase is the particle size. If the particle size could be decreased below 50 nm it would give rise to a very effective transparent near-IR absorbing pigment.

CHAPTER 7

ZINC IRON DIPHOSPHATE

7.1 Introduction

Iron is one of the most prevalent elements on Earth; it gives to the earth its red or yellow colouration. It would therefore be economically beneficial to develop a pigment using this element.

In the previous chapters, mixed metal copper phosphates were revealed to be useful materials for near-infrared absorption purposes. This is due to the intense and broad single absorption band resulting from splitting of the free ion term ^2D into ^2E_g and $^2T_{2g}$ and the *Jahn Teller* effect on these levels. Also other transition metal ions can have a free ion D term, which is in particular the case for Fe^{2+} (d^6) in high spin state. The difference when compared to copper(II) is in the energetic levels of the ground state and the excited state, which are reversed compared to Cu^{2+} [97]. The t_{2g} orbital being asymmetrically occupied, Fe^{2+} is less prone to *Jahn Teller* distortion and the absorption should therefore occur as a sharper band.

As reported by *Annersten et al.* [98] iron and zinc form a solid solution in $(Zn,Fe)_3(PO_4)_2$ with iron(II) supposedly situated on the octahedral sites of the structure (Figure 7.1). Due to the phosphates being weak field ligands, it is believed that in this structure iron(II) is in a high spin configuration. Therefore a spectroscopic investigation of this material was of interest for this study.

This section describes the synthesis and characterisation of the $(Zn,Fe)_3(PO_4)_2$ solid

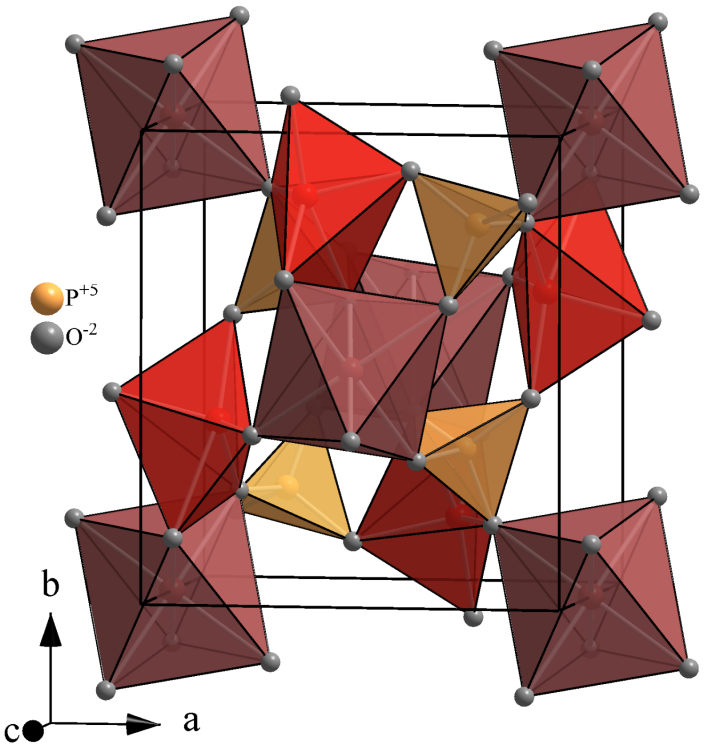

Figure 7.1: Projection along the a axis of the $(Zn,Fe)_3(PO_4)_2$ structure. The PO_4 units are shown as orange tetrahedra, the five-fold arrangement around the Zn atoms is shown in bright red and the distorted octahedral site for Zn/Fe atoms is shown in dark red.

solution.

7.2 Synthesis

Following the procedure described by *Nord* [99], pure orthophosphate $Zn_3(PO_4)_2$ was prepared by reaction of ZnO with ammonium dihydrogen phosphate at 1000 °C in an open platinum crucible. The synthesis time was one week. The $Fe_3(PO_4)_2$ orthophosphate was synthesised [100]. A stoichiometric solution of $Fe(NO_3)_3{\cdot}9H_2O$ and $NH_4H_2PO_4$ was gently dehydrated and then heated at 400 °C overnight. The resulting mixture was ground to a fine powder, placed in an alumina crucible and heated at 2 °C min^{-1} to 900 °C under a flow of wet 5% H_2/95% N_2. The temperature was

maintained for 24 hours before cooling at 2 °C min^{-1} to room temperature. The solid-solutions were finally prepared by heating a stoichiometric amount of previously prepared orthophosphates for one week at 800 °C in evacuated silica tubes to prevent the oxidation of iron.

Although this procedure produced fine material, it was time consuming and therefore it was impractical for preparing larger batches required by powder neutron diffraction.

In order to synthesise large homogeneous samples, the following method was preferred. $Fe(NO_3)_3{\cdot}9H_2O$, ZnO and $NH_4H_2PO_4$ were used as starting materials. They were dissolved in a minimum of dilute nitric acid solution and mixed together to obtain a clear brown solution. This solution was evaporated to dryness and the residue was subsequently heated to 350 °C overnight to decompose NH_4NO_3. The resulting mixture was ground to a fine powder, placed into an alumina boat and heated up slowly at 2 °C min^{-1} in a tube furnace to reach 900 °C under a flow of wet 5% H_2/95% N_2. The temperature was maintained for 24 hours before cooling at 2 °C min^{-1} to room temperature.

The resulting samples were analysed by powder X-ray diffraction, powder neutron diffraction and UV to near-infrared spectroscopy.

7.3 Structural Refinement

7.3.1 Powder X-ray Diffraction

PXD data were collected overnight on a D8 diffractometer using the method outlined in Chapter 2.

For each member of this series the pattern could be indexed in the space group of the γ-$Zn_3(PO_4)_2$, $P\,2_1/n$. Unit cell parameters were found with approximate values a = 7.56 Å b = 8.54 Å c = 5.05 Å and β = 95.4°. However, due to strong fluorescence of these materials the purity of the samples could not be accurately analysed.

7.3.2 Powder Neutron Diffraction

PND data were collected on D1A at the Institut Laue-Langevin on *ca.* 5 g size samples at room temperature over a period of 7 hours for each sample. *Rietveld* structural refinement was carried out using the model from *Nord* [99]. Zero correction, background coefficients and peak profiles were first evaluated then lattice parameters were refined to accurately locate the reflections.

The first observation was the presence of multiple phases in all of the samples containing more than 33% of iron in the synthesis mixture. These phases could not be dissociated from the main phase and it was therefore not possible to obtain full *Rietveld* refinements for these samples.

For the remaining samples, *i.e.* $Zn_{2.75}Fe_{0.25}(PO_4)_2$, $Zn_{2.5}Fe_{0.5}(PO_4)_2$, $Zn_{2.25}Fe_{0.75}(PO_4)_2$ and $Zn_2Fe(PO_4)_2$, after the profile fit has been performed, atomic positions were allowed to refine. However, the fractional site occupancies were fixed for both mixed sites at that stage of the refinement. Isotropic temperature factors were finally added.

As no impurity phases were detected to account for any loss of zinc or iron, distribution of both elements into either the octahedral site or the trigonal bipyramidal site was investigated using the systematic approach described by *Nord* [99]. All refinement parameters were allowed to vary while cations distribution was systematically altered. The *best fit* was identified by the lowest R values.

The refinements converged nicely and the profile fit for all the samples can be observed in Figure 7.2 to 7.5. The following tables (Tables 7.1 to 7.4) present the crystallographic data and refinement statistics for each phase. The bond lengths and angles for both sites are expressed in Tables 7.5 to 7.8.

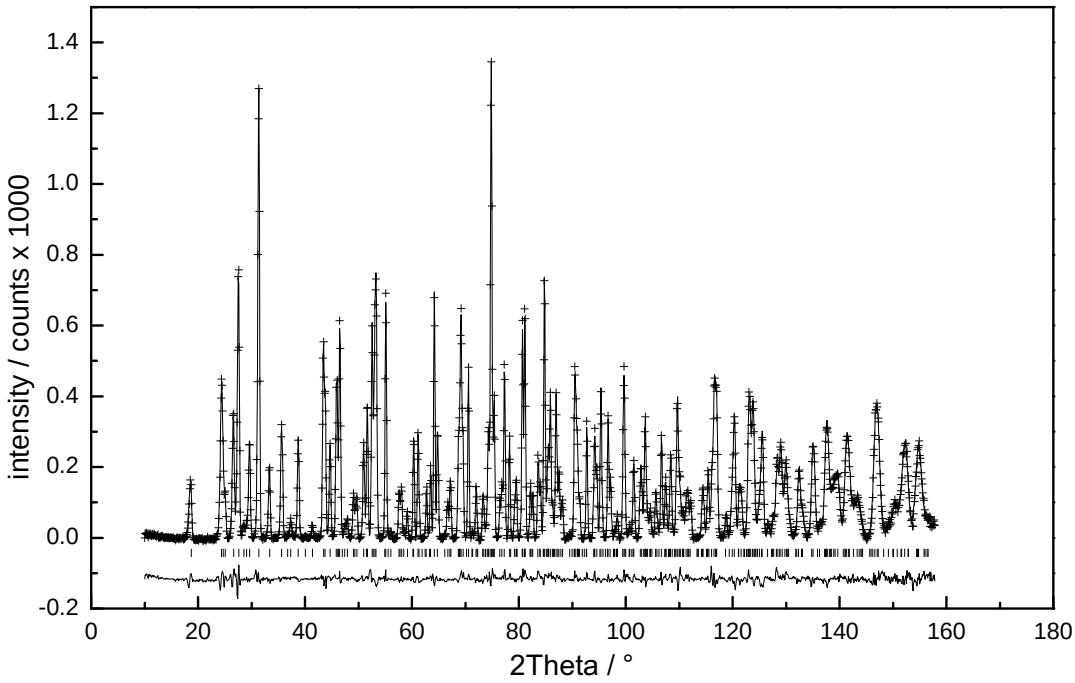

Figure 7.2: *Rietveld* refinement profile fit of $Zn_{2.75}Fe_{0.25}(PO_4)_2$. Observed data points are shown as crosses and the calculated pattern is shown as a solid line. The difference between the calculated and observed patterns is shown underneath. The position of the peaks are marked by the row of vertical lines.

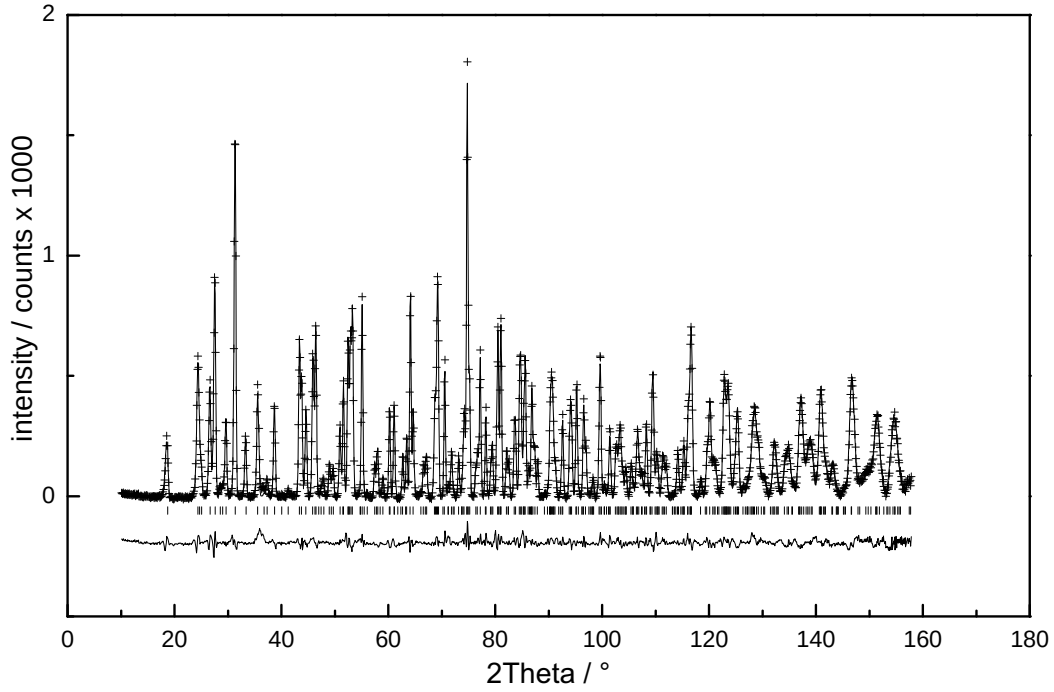

Figure 7.3: *Rietveld* refinement profile fit of $Zn_{2.5}Fe_{0.5}(PO_4)_2$. Observed data points are shown as crosses and the calculated pattern is shown as a solid line. The difference between the calculated and observed patterns is shown underneath. The position of the peaks are marked by the row of vertical lines.

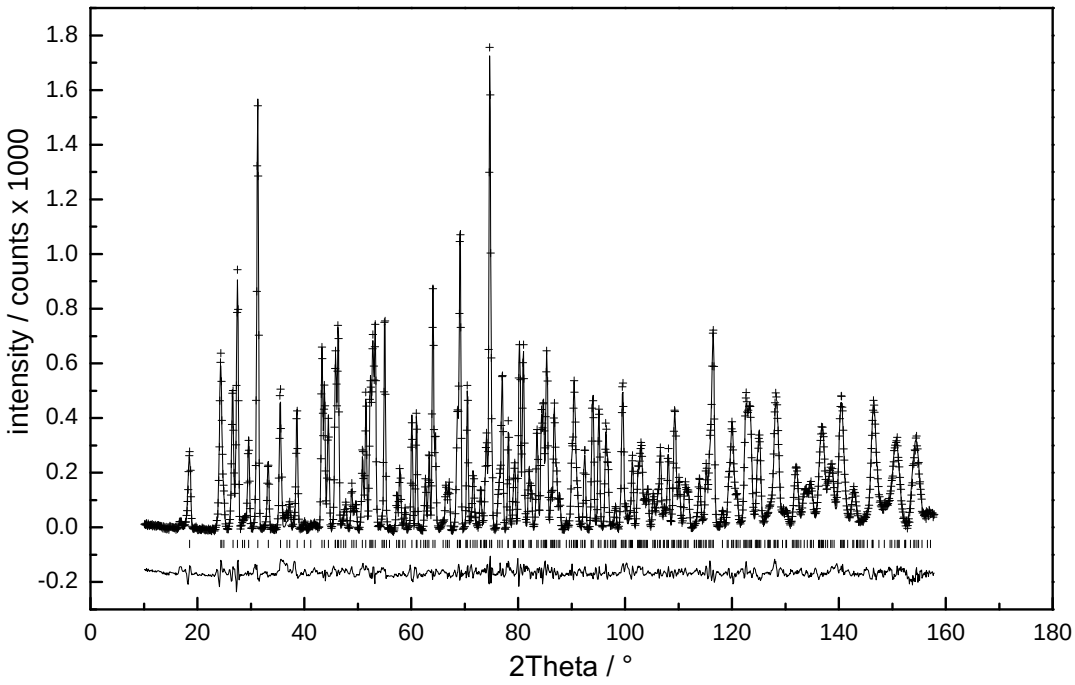

Figure 7.4: *Rietveld* refinement profile fit of $Zn_{2.25}Fe_{0.75}(PO_4)_2$. Observed data points are shown as crosses and the calculated pattern is shown as a solid line. The difference between the calculated and observed patterns is shown underneath. The position of the peaks are marked by the row of vertical lines.

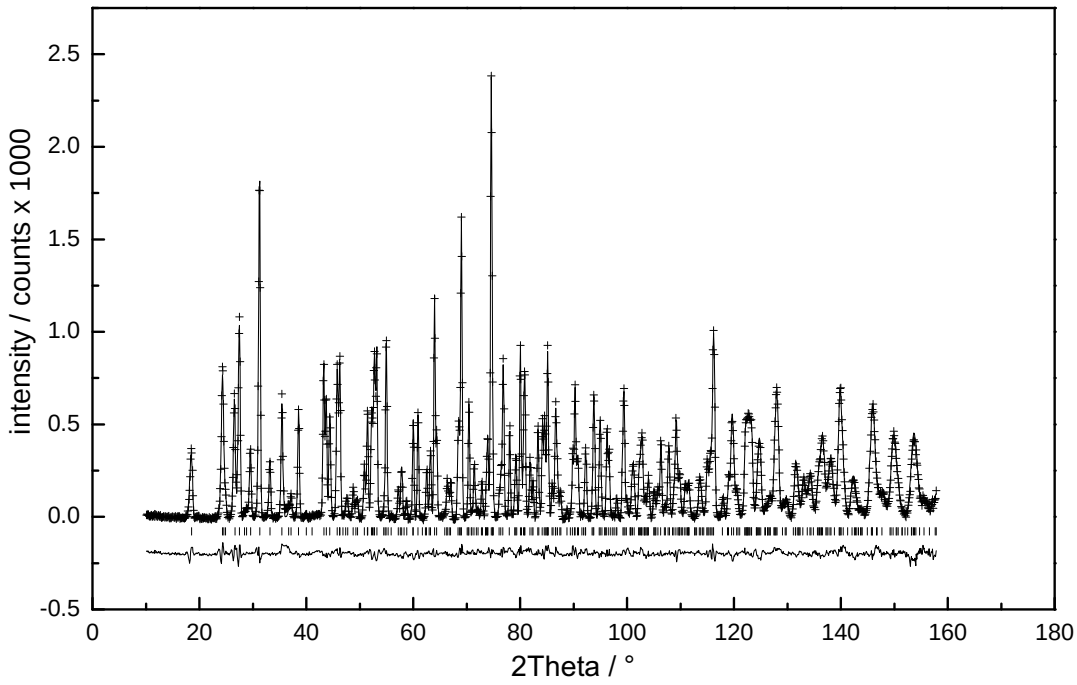

Figure 7.5: *Rietveld* refinement profile fit of $Zn_2Fe(PO_4)_2$. Observed data points are shown as crosses and the calculated pattern is shown as a solid line. The difference between the calculated and observed patterns is shown underneath. The position of the peaks are marked by the row of vertical lines.

Table 7.1: Refined crystallographic data for $Zn_{2.75}Fe_{0.25}(PO_4)_2$ (e.s.d.s in parentheses).

Space group $P\,2_1/n$.
Lattice parameters a = 7.54181(10) Å, b = 8.48485(13) Å, c = 5.04045(8) Å, β = 95.3267(8)°

Name	x	y	z	Frac.	U_{iso} / Å^2*100
Zn1	0.61924(21)	0.13809(19)	0.07447(34)	1	0.70(5)
Fe1	0.61924(21)	0.13809(19)	0.07447(34)	0	0.70(5)
Zn2	0	0	1/2	0.75	0.65(7)
Fe2	0	0	1/2	0.25	0.65(7)
P1	0.19667(22)	0.19116(20)	0.0327(4)	1	0.76(5)
O1	0.05071(21)	0.13106(19)	0.82691(34)	1	1.21(5)
O2	0.12774(24)	0.19738(19)	0.30933(34)	1	1.08(4)
O3	0.25180(20)	0.35486(20)	0.93299(33)	1	1.05(4)
O4	0.35905(23)	0.07974(18)	0.04975(33)	1	0.98(4)

Final fit parameters: χ^2 = 4.072, R(F^2) = 2.93%, R_{wp} = 3.69%, R_p = 2.84%

Table 7.2: Refined crystallographic data for $Zn_{2.5}Fe_{0.5}(PO_4)_2$ (e.s.d.s in parentheses).

Space group $P\,2_1/n$.
Lattice parameters a = 7.54924(14) Å, b = 8.50819(18) Å, c = 5.04225(10) Å, β = 95.3713(13)°

Name	x	y	z	Frac.	U_{iso} / Å^{2*}100
Zn1	0.61955(27)	0.13744(26)	0.0735(4)	1	0.75(6)
Fe1	0.61955(27)	0.13744(26)	0.0735(4)	0	0.75(6)
Zn2	0	0	1/2	0.5	1.28(6)
Fe2	0	0	1/2	0.5	1.28(6)
P1	0.19746(30)	0.19068(26)	0.0319(5)	1	0.76(6)
O1	0.05127(28)	0.13137(25)	0.8277(5)	1	1.23(6)
O2	0.12878(31)	0.19845(25)	0.3085(5)	1	0.93(6)
O3	0.25216(26)	0.35435(26)	0.9314(4)	1	0.98(6)
O4	0.35966(30)	0.08062(24)	0.0500(4)	1	1.00(6)

Final fit parameters: χ^2 = 7.325, R(F^2) = 3.62%, R_{wp} = 4.44%, R_p = 3.32%

Table 7.3: Refined crystallographic data for $Zn_{2.25}Fe_{0.75}(PO_4)_2$ (e.s.d.s in parentheses).

Space group $P\,2_1/n$.
Lattice parameters a = 7.55517(17) Å, b = 8.52827(21) Å, c = 5.04322(12) Å, β = 95.3824(15)°

Name	x	y	z	Frac.	U_{iso} / Å^{2*}100
Zn1	0.61947(31)	0.13712(29)	0.0723(5)	0.95	1.02(7)
Fe1	0.61947(31)	0.13712(29)	0.0723(5)	0.05	1.02(7)
Zn2	0	0	1/2	0.35	1.08(9)
Fe2	0	0	1/2	0.65	1.08(9)
P1	0.19801(34)	0.19064(30)	0.0305(6)	1	0.81(8)
O1	0.05212(32)	0.13077(28)	0.8282(5)	1	1.25(7)
O2	0.12939(36)	0.19989(28)	0.3077(5)	1	0.88(7)
O3	0.25230(30)	0.35419(29)	0.9301(5)	1	1.08(7)
O4	0.36011(35)	0.08086(27)	0.0509(5)	1	1.03(6)

Final fit parameters: χ^2 = 10.43, R(F^2) = 3.96%, R_{wp} = 4.59%, R_p = 3.47%

Table 7.4: Refined crystallographic data for $Zn_2Fe(PO_4)_2$ (e.s.d.s in parentheses).

Space group $P\,2_1/n$.
Lattice parameters a = 7.56512(10) Å, b = 8.54535(12) Å, c = 5.04918(7) Å, β = 95.3267(10)°

Name	x	y	z	Frac.	U_{iso} / Å^{2*}100
Zn1	0.62031(23)	0.13713(22)	0.0731(4)	0.9	0.81(5)
Fe1	0.62031(23)	0.13713(22)	0.0731(4)	0.1	0.81(5)
Zn2	0	0	1/2	0.2	0.74(4)
Fe2	0	0	1/2	0.8	0.74(4)
P1	0.19857(26)	0.19089(23)	0.0319(4)	1	0.59(6)
O1	0.05291(25)	0.13065(22)	0.8279(4)	1	1.16(5)
O2	0.12981(29)	0.19998(23)	0.3072(4)	1	1.10(5)
O3	0.25293(24)	0.35407(22)	0.9303(4)	1	0.96(5)
O4	0.36035(27)	0.08148(22)	0.0499(4)	1	1.03(5)

Final fit parameters: χ^2 = 5.859, R(F^2) = 3.53%, R_{wp} = 3.88%, R_p = 2.99%

Table 7.5: Derived bond distances and angles for the coordination spheres of copper in $Zn_{2.75}Fe_{0.25}(PO_4)_2$ (e.s.d.s in parentheses)

Bond	Distance / Å	Bond Angle	Angle / °
Fe1_O1	2.4166(22)	O2_Fe1_O3	124.13(10)
Fe1_O2	1.9383(22)	O2_Fe1_O4	103.16(9)
Fe1_O3	1.9826(22)	O2_Fe1_O4	116.59(11)
Fe1_O4	2.0172(22)	O3_Fe1_O4	118.00(10)
Fe1_O4	1.9642(21)	O3_Fe1_O4	105.64(10)
		O1_Fe1_O2	78.60(8)
		O1_Fe1_O3	67.05(8)
		O1_Fe1_O4	88.70(9)
		O1_Fe1_O4	163.60(10)
		O4_Fe1_O4	81.94(10)
Fe2_O1	1.9957(17)	O1_Fe2_O1	179.980(0)
Fe2_O1	1.9957(17)	O1_Fe2_O2	82.99(6)
Fe2_O2	2.1984(17)	O1_Fe2_O2	97.01(6)
Fe2_O2	2.1984(17)	O1_Fe2_O3	95.07(6)
Fe2_O3	2.2404(16)	O1_Fe2_O3	84.93(6)
Fe2_O3	2.2404(16)	O2_Fe2_O2	180.000(0)
		O2_Fe2_O3	95.23(6)
		O2_Fe2_O3	84.77(6)

Table 7.6: Derived bond distances and angles for the coordination spheres of copper in $Zn_{2.5}Fe_{0.5}(PO_4)_2$ (e.s.d.s in parentheses)

Bond	Distance / Å	Bond Angle	Angle / °
Fe1_O1	2.4304(30)	O2_Fe1_O3	123.74(14)
Fe1_O2	1.9396(30)	O2_Fe1_O4	103.26(13)
Fe1_O3	1.9823(29)	O2_Fe1_O4	116.87(14)
Fe1_O4	2.0142(30)	O3_Fe1_O4	117.94(14)
Fe1_O4	1.9682(28)	O3_Fe1_O4	105.83(14)
		O1_Fe1_O2	78.64(11)
		O1_Fe1_O3	66.78(11)
		O1_Fe1_O4	88.35(11)
		O1_Fe1_O4	163.24(13)
		O4_Fe1_O4	82.02(13)
Fe2_O1	2.0014(23)	O1_Fe2_O1	180.000(0)
Fe2_O1	2.0014(23)	O1_Fe2_O2	82.89(9)
Fe2_O2	2.2142(22)	O1_Fe2_O2	97.11(9)
Fe2_O2	2.2142(22)	O1_Fe2_O3	95.02(8)
Fe2_O3	2.2426(22)	O1_Fe2_O3	84.98(8)
Fe2_O3	2.2426(22)	O2_Fe2_O2	179.956(0)
		O2_Fe2_O3	95.39(8)
		O2_Fe2_O3	84.61(8)

Table 7.7: Derived bond distances and angles for the coordination spheres of copper in $Zn_{2.25}Fe_{0.75}(PO_4)_2$ (e.s.d.s in parentheses)

Bond	Distance / Å	Bond Angle	Angle / °
Fe1_O1	2.4424(33)	O2_Fe1_O3	123.53(16)
Fe1_O2	1.933(4)	O2_Fe1_O4	103.61(15)
Fe1_O3	1.9819(33)	O2_Fe1_O4	116.82(16)
Fe1_O4	2.0105(34)	O3_Fe1_O4	117.75(16)
Fe1_O4	1.9708(33)	O3_Fe1_O4	105.93(16)
		O1_Zn1_O2	78.78(13)
		O1_Zn1_O3	66.52(12)
		O1_Zn1_O4	88.36(13)
		O1_Zn1_O4	163.23(15)
		O4_Fe1_O4	82.11(15)
Fe2_O1	2.0041(26)	O1_Fe2_O1	180.000(0)
Fe2_O1	2.0041(26)	O1_Fe2_O2	82.74(10)
Fe2_O2	2.2315(25)	O1_Fe2_O2	97.26(10)
Fe2_O2	2.2315(25)	O1_Fe2_O3	94.71(9)
Fe2_O3	2.2470(25)	O1_Fe2_O3	85.29(9)
Fe2_O3	2.2470(25)	O2_Fe2_O2	180.000(0)
		O2_Fe2_O3	95.66(9)
		O2_Fe2_O3	84.34(9)

Table 7.8: Derived bond distances and angles for the coordination spheres of copper in $Zn_2Fe(PO_4)_2$ (e.s.d.s in parentheses)

Bond	Distance / Å	Bond Angle	Angle / °
Fe1_O1	2.4442(26)	O2_Fe1_O3	123.67(12)
Fe1_O2	1.9399(28)	O2_Fe1_O4	103.16(11)
Fe1_O3	1.9822(25)	O2_Fe1_O4	116.85(12)
Fe1_O4	2.0161(26)	O3_Fe1_O4	118.07(12)
Fe1_O4	1.9784(25)	O3_Fe1_O4	106.00(12)
		O1_Fe1_O2	78.73(10)
		O1_Fe1_O3	66.61(9)
		O1_Fe1_O4	88.40(10)
		O1_Fe1_O4	163.14(12)
		O4_Fe1_O4	81.90(12)
Fe2_O1	2.0061(20)	O1_Fe2_O1	179.980(0)
Fe2_O1	2.0061(20)	O1_Fe2_O2	82.64(8)
Fe2_O2	2.2382(20)	O1_Fe2_O2	97.36(8)
Fe2_O2	2.2382(20)	O1_Fe2_O3	94.61(7)
Fe2_O3	2.2473(19)	O1_Fe2_O3	85.39(7)
Fe2_O3	2.2473(19)	O2_Fe2_O2	179.960(0)
		O2_Fe2_O3	95.72(7)
		O2_Fe2_O3	84.28(7)

7.3.3 Site occupancies

Figure 7.6 shows the refined octahedral site occupancies for iron(II) together with a theoretical even distribution of Zn^{2+} and Fe^{2+} in both sites and a theoretical preferred distribution of Fe^{2+} in the octahedral site. It is obvious that iron(II) has a strong preference for the octahedral site. This explains the multiple phases formed if the iron content during synthesis is higher than 33%.

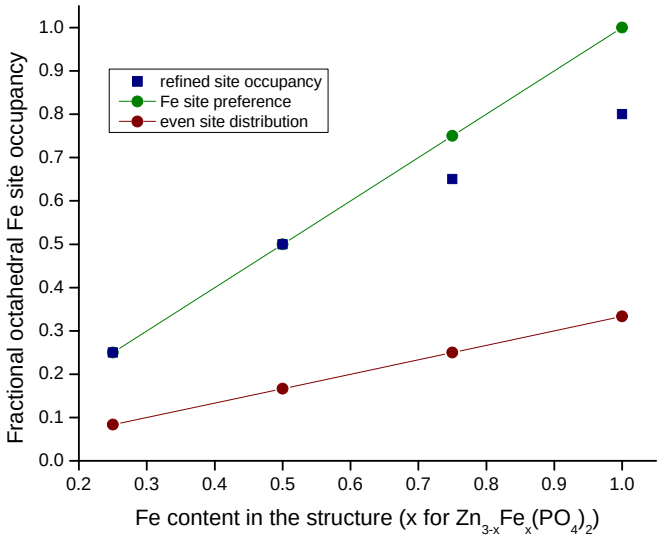

Figure 7.6: Description of iron(II) in the octahedral site.

7.4 UV to Near-infrared Spectroscopy

Solid state UV to near-infrared spectroscopical data were collected on undiluted samples according to the method outlined in Chapter 2.

Through the entire series, the absorption spectra consist of a sharp absorption band centred at 1000 nm and a broad band centred at 1850 nm. The intensity of both bands increase with the amount of iron in the structure.

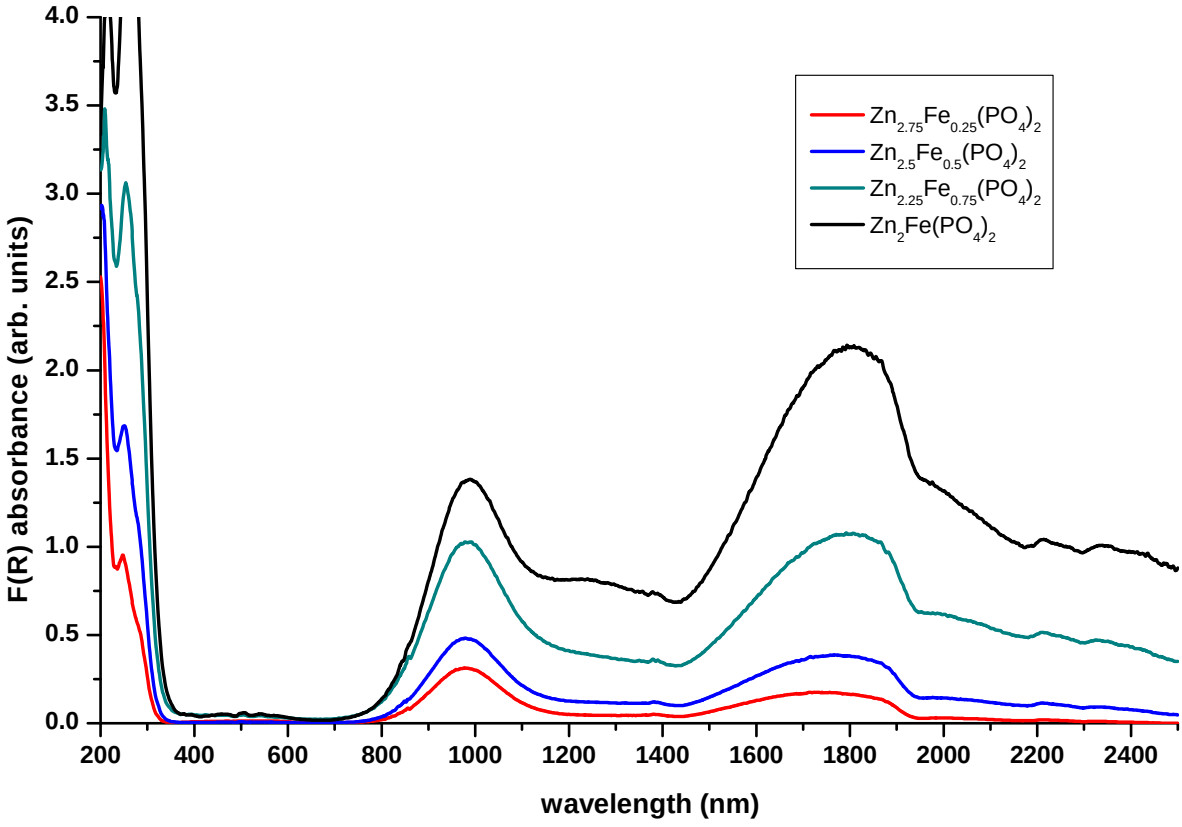

Figure 7.7: UV to near-infrared spectra of the $(Zn,Fe)_3(PO_4)_2$ series.

7.5 Discussion

In this structure, Fe^{2+} ions are situated mainly in the octahedral sites. This observation is correlated with the absorption band centred at 1000 nm. As iron(II) is a d^6 ion and phosphate ligands are known to be weak field ligands, iron(II) in this material is in high spin configuration. The free ion ground term is ^5D which splits in an octahedral symmetry into a ground state $^5T_{2g}$ ($t_2^4e^2$) and an excited state ^5E_g ($t_2^3e^3$) [101]. The absorption band at 1000 nm is therefore due to the $^5E_g \leftarrow {}^5T_{2g}$ electronic transition. This absorption band is relatively sharp compared to the absorption encountered generally for Cu^{2+} ions situated in octahedral sites, but it is much weaker.

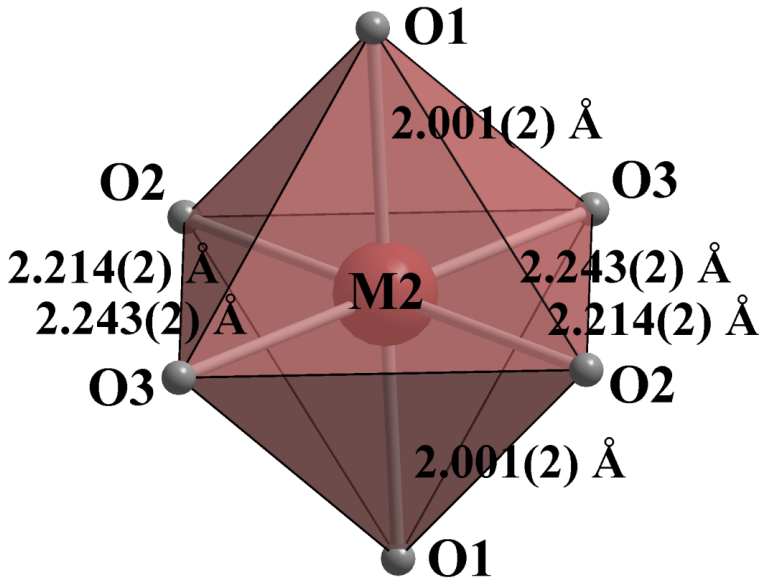

Figure 7.8: Nearly perfect compressed octahedral site in $Zn_{2.5}Fe_{0.5}(PO_4)_2$.

From Tables 7.5 to 7.8 the distortion undergone by the octahedron is an elongation of the equatorial bond lengths together with a compression of the axial bond lengths with increasing amount of iron(II), which should split the t_{2g} and e_g degenerate orbitals into b_{2g}, e_g and b_{1g}, a_{1g} respectively. However, it has been commonly reported that to give rise to a measurable *Jahn Teller* distortion, the asymmetrically occupied orbitals have to be e_g rather than t_{2g} [13]. As in Fe^{2+} ions in high spin configuration, t_{2g} is

asymmetrically occupied; Thus, the reason for the sharpness of the absorption band becomes obvious.

The weakness of the absorption intensity on the other hand is due to the *Laporte* selection rule. In $(Zn,Fe)_3(PO_4)_2$ the octahedral site is close to perfect symmetry (Figure 7.8). Therefore the vibronic coupling is not strong enough to relax the *Laporte* selection rule, and the absorption is almost completely symmetry forbidden.

The broad band centred at 1850 nm is less straightforward to assign. One hypothesis is that this band is due to an overtone of H_2O [102]. As the samples were prepared in wet H_2/N_2 gas flow conditions, they might have incorporated some water. This assumption would also explain the observed spongy appearance of these powders. On the other hand, the absorption intensity of this band is directly proportional to the amount of iron introduced which rules out this suggestion.

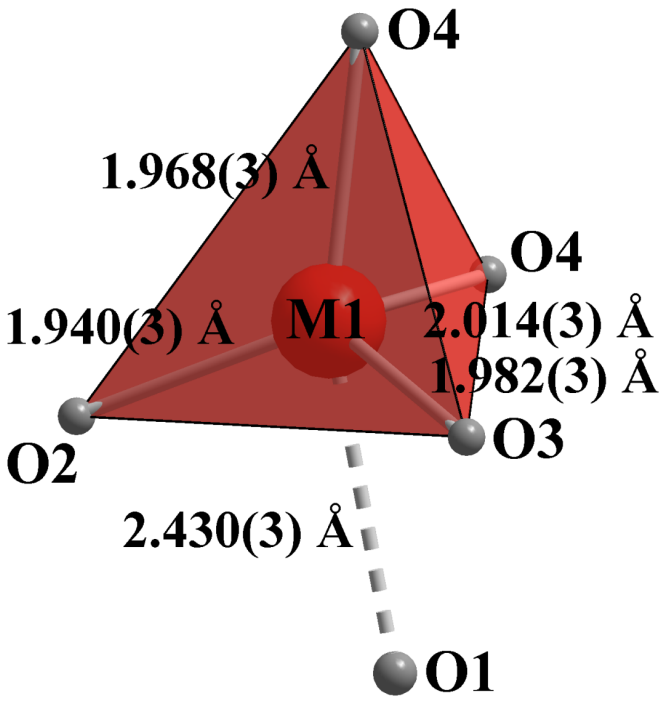

Figure 7.9: Description of the five-fold site in $Zn_2Fe(PO_4)_2$ as a distorted tedrahedral site plus one extended bond.

Another explanation would be the presence of Fe^{2+} in a tetrahedral site, often found in silicate glasses [103]. This is particularly surprising since in this structure, cations should be situated in octahedral sites or five-fold sites. However with regard to the bond distances and angles exhibited in the five-fold site, it could be perceived as a distorted tetrahedron plus one bond rather than a distorted five-fold site (Figure 7.9). A simple approximation contradicts this conclusion. For non-distorted octahedral and tetrahedral sites and for energy expressed in wavenumbers, $\Delta_t = \frac{4}{9}\Delta_o$. In the investigated system, Δ_o is approximately 10000 cm^{-1} (1000 nm), which would yield Δ_t at around 4444 cm^{-1} (2250 nm). Even by taking into account a strong distortion of this site, the observed absorption band is too far off from the theoretical position.

The most reasonable hypothesis is to have some Fe^{2+} in the five-fold coordinated site. In this structure, the five-fold site is supposed to have a strongly distorted trigonal bipyramidal symmetry (Figure 7.10). As seen in Tables 7.5 to 7.8, this site is com-

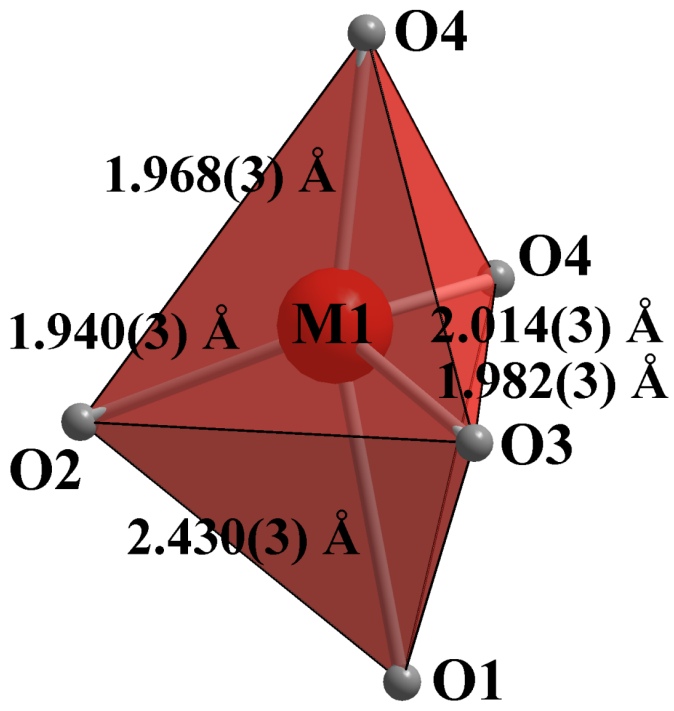

Figure 7.10: Description of the five-fold site in $Zn_2Fe(PO_4)_2$ as a strongly distorted trigonal bipyramidal.

posed of four equivalent bond lengths with an average angle of 105° between the basal bonds and the apical bond and an elongated bond. For a perfect trigonal bipyramidal symmetry these angles should averaged to 90°. However, the elongated bond lowers the hindrance of O1; O2, O3 and O4 are displaced out of the basal plane by the same amplitude (Figure 7.11) [104]. These movements change the shape and energy of some of the orbitals as described in Figure 7.12. Spectroscopically speaking, $^5A'_1$ is strongly lowered by the stabilisation of d_{z^2} orbital while $^5E'$ is only slightly stabilised and $^5E''$ is destabilised. Further splitting of these levels may occur; often too subtle to be described they account for the broadening of the band. The absorption band can therefore be interpreted by the $^5E'' \leftarrow {}^5A'_1$ electronic transition.

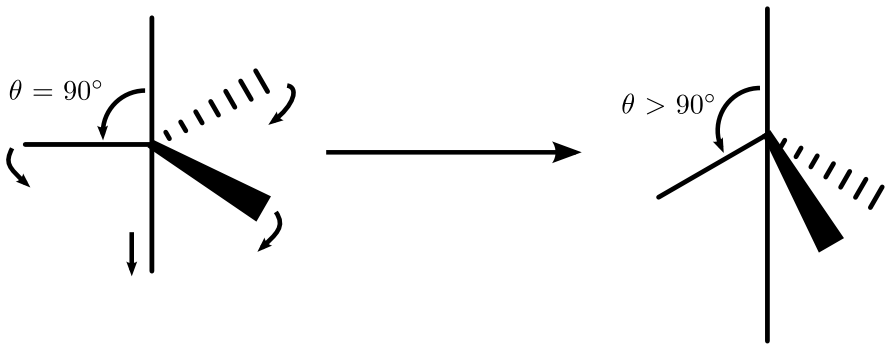

Figure 7.11: Scheme of the displacement undergone by the oxygens in the distorted trigonal bipyramid.

From Figure 7.6 it seems that iron(II) atoms start to occupy the five-fold coordinated site only when the content of Fe^{2+} in the structure is higher than 16%. However the spectra in Figure 7.7 shows some of the Fe^{2+} in this site for lower concentrations. Spectroscopy being more sensitive to transition metal coordination than diffraction methods, it is most probable that, although iron(II) shows a clear preference for the octahedral site, a small amount of the Fe^{2+} and Zn^{2+} is exchanged between these two sites because of their relatively close ionic radii.

The band centred at 1850 nm is more intense than the band centred at 1000 nm. This is mainly due to the complete lack of centre of symmetry in the distorted trigonal

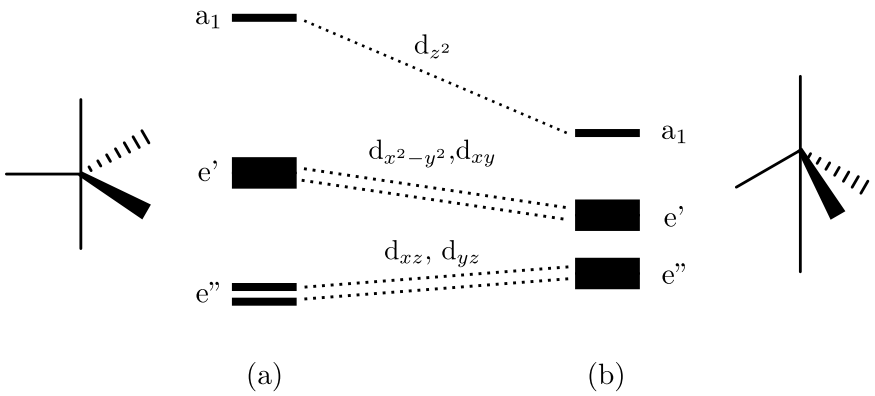

Figure 7.12: The orbital correlation diagram for (a) a trigonal bipyramid (D_{3h}) and (b) a distorted trigonal bipyramid (D_{3h}).

bipyramidal site.

7.6 Conclusion

The synthesis and spectroscopical characterisation of the $(Zn,Fe)_3(PO_4)_2$ system has been achieved. It was shown that Fe^{2+} in this series shows a strong preference for the octahedral site.

The absorption resulting from iron(II) in the octahedral site has been described to be relatively sharp which could be useful for applications such as laser wielding. However, the absorption is weak due to the nearly perfect octahedral symmetry.

On the other hand, the absorption band due to Fe^{2+} in the distorted five-fold coordinated site has shown a strong intensity although not in the desired region. This behaviour could however be associated to another transition metal ion such as copper(II) in a distorted octahedral site to obtain a material able to absorb through the entire near-infrared region.

CHAPTER 8

MAGNESIUM COPPER SILICATE

8.1 Introduction

Silicates and phosphates are very similar in terms of their structural and coordination chemistry. They are formed by interlinked tetrahedral units and are relatively weak ligands. However, in contrast to the latter, silicate materials need very demanding synthesis conditions such as high temperature, pressure and time for the reaction to occur. This is the main reason that only a few copper silicates can be found in nature and even then only as secondary minerals. One of these simple copper silicates is the mineral dioptase with the formula $CuSiO_3 \cdot H_2O$ which has a blue to green colour and is structurally composed of discrete SiO_4^{4-} units and copper(II) ions in a square planar environment [105]. In the previous chapters, square planar coordination has been described as a tetragonally distorted octahedron with infinite axial bond lengths. This distortion induces a blue shift of the absorption band. It should therefore be possible to obtain absorption in the near-infrared by having Cu^{2+} in an octahedral site or in a site with five-fold symmetry.

The few structurally investigated simple copper silicates found in the literature all exhibit copper situated in a square planar environment. It was therefore decided that a solid solution should be studied instead, in particular the clinopyroxene $Mg_{(2-x)}Cu_xSi_2O_6$. *Breuer et al.* [106] described this material as built up from chains of joint SiO_4 tetrahedral units and cations situated in two different octahedral sites (M1 and M2), with copper preferably situated in the M2 site. The M2 site is the less

tetragonally distorted site.

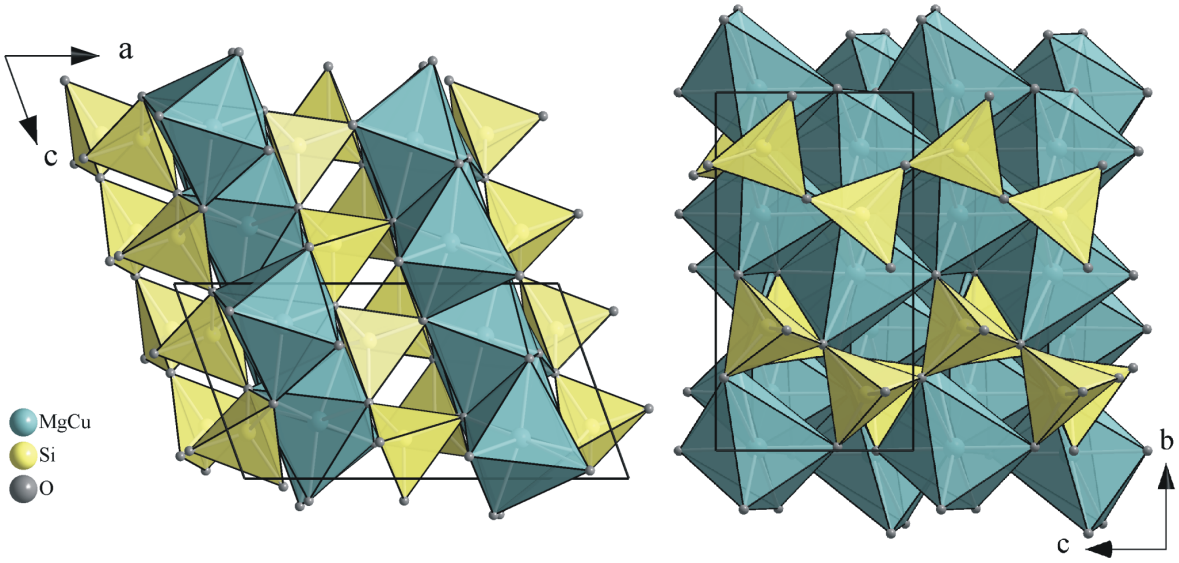

Figure 8.1: Projection of the $Mg_{1.2}Cu_{0.8}Si_2O_6$ structure. The SiO_4 units are shown as yellow tetrahedra forming infinite chains. The octahedral coordination environments around the Mg/Cu atoms are shown in blue.

In this chapter, the synthesis and characterisation of $Mg_{1.2}Cu_{0.8}Si_2O_6$ is described.

8.2 Synthesis

On the first hand, it was attempted to prepare a range of sample of the series of $Mg_{(2-x)}Cu_xSi_2O_6$ (x = 0.1, 0.3 and 0.5) using the method of *Breuer et al.* [106]. A stoichiometric mixture of CuO, MgO and SiO_2 was ground using an agate mortar. The resulting fine powder was heated in a platinum crucible for 4 weeks at 950 °C. Repeated mixing and regrinding through the process was necessary for the reaction to be effective.

The resulting samples were first analysed by powder X-ray diffraction. However, only the $Mg_{1.5}Cu_{0.5}Si_2O_6$ sample was exploitable due to the overwhelming presence of starting materials in both $Mg_{1.9}Cu_{0.1}Si_2O_6$ and $Mg_{1.7}Cu_{0.3}Si_2O_6$ samples. Therefore only the $Mg_{1.5}Cu_{0.5}Si_2O_6$ sample is described in this Chapter. Powder neutron diffraction

and UV to near-infrared spectroscopy techniques were also used. It was found for this sample that the composition differ from the expected solid solution and was better described as $Mg_{1.2}Cu_{0.8}Si_2O_6$.

8.3 Structural Refinement

8.3.1 Powder X-ray diffraction

PXD data were collected overnight on a Bruker D8 diffractometer using the method outlined in Chapter 2.

Inspection of the data showed the presence of two impurities besides the main phase. One impurity was unreacted SiO_2 starting material, the second was fosterite Mg_2SiO_4.

A *Le Bail* fit was performed for the main phase of this sample to determine the approximate lattice parameters. Using the atomic parameters of clinoenstatite $Mg_2Si_2O_6$ ($P2_1/c$) after *Morimoto et al.* [107], the unit cell was determined as a = 9.68 Å, b = 8.88 Å, c = 5.21 Å and β = 70.02 Å. These values were relatively close to the values from the literature for a phase with the formula $Mg_{1.2}Cu_{0.8}Si_2O_6$ phase. However, the presence of the two impurities restrain any attempt of *Rietveld* refinement . In order to accurately describe the structure, powder neutron diffraction was performed.

8.3.2 Powder Neutron diffraction

PND data was collected at the beamline D2B at the Institut Laue-Langevin on a *ca.* 5 g sample at room temperature over a period of 4 hours. A *Rietveld* structural refinement was carried out using the structural model from *Morimoto et al.* [107] with the lattice parameters obtained from the X-ray diffraction data as a starting point. Zero correction, background coefficients and peak profiles were first evaluated, then lattice parameters were refined to accurately locate the reflections. The fractional site occupancies were fixed for both mixed sites at that stage of the refinement. Peaks from the impurities

were modelled using *Le Bail* fits and atom positions for the main phase were allowed to vary with a linear constraint on Mg/Cu shared sites. Isotropic thermal factors were refined. Since some isotropic thermal factors became either negative or too large, the cation distribution was systematically altered using the systematic approach described by *Nord* [99].

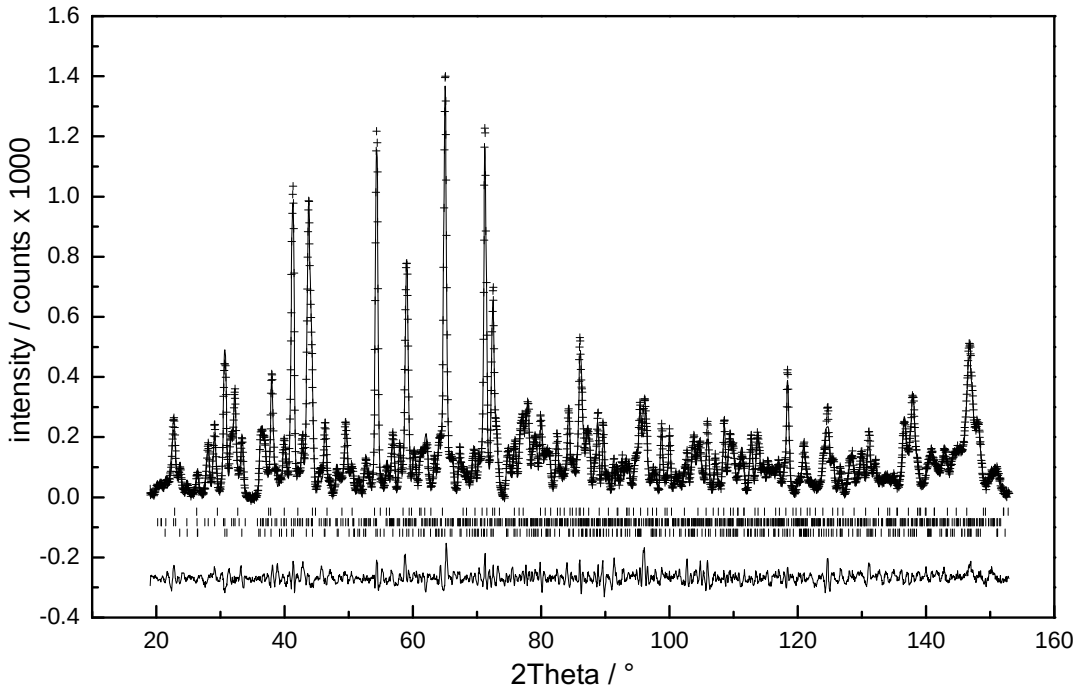

Figure 8.2: *Rietveld* refinement profile fit of $Mg_{1.2}Cu_{0.8}Si_2O_6$. Observed data points are shown as crosses and the calculated pattern is shown as a solid line. The difference between the calculated and observed patterns is shown underneath. The position of the peaks for the SiO_2 phase is marked by the first row of vertical lines, the second row marks the position of the peaks for $Mg_{1.2}Cu_{0.8}Si_2O_6$ phase and the last row marks the position of the peaks for the Mg_2SiO_4. Relative to $Mg_{1.2}Cu_{0.8}Si_2O_6$ the phase fraction of Mg_2SiO_4 is 8% and of SiO_2 is 11%

The *best fit* was identified for $Mg_{1.2}Cu_{0.8}Si_2O_6$. This is confirmed by the unit cell parameters which follow the trend of the cell parameters over the Mg/Cu ratio described by *Breuer et al.* [106]. This would account as well for the loss of some magnesium into the Mg_2SiO_4 fosterite impurity. By careful monitoring of both thermal factors and R

values, the copper(II) atoms were found to occupy preferentially the M2 site (Table 8.1).

Table 8.1: Refined crystallographic data for $Mg_{1.2}Cu_{0.8}Si_2O_6$ (e.s.d.s in parentheses).

Space group $P\,2_1/n$.
Lattice parameters a = 9.6906(6) Å, b = 8.8888(6) Å, c = 5.2162(4) Å, β = 70.075(5)°

Name	x	y	z	Frac.	U_{iso} / Å^{2*}100
Mg1	0.2444(8)	0.9931(9)	0.2071(14)	0.8	1.77(15)
Cu1	0.2444(8)	0.9931(9)	0.2071(14)	0.2	1.77(15)
Mg2	0.2440(7)	0.3425(8)	0.2266(12)	0.4	1.55(13)
Cu2	0.2440(7)	0.3425(8)	0.2266(12)	0.6	1.55(13)
Si1	0.4513(8)	0.6596(12)	0.2944(15)	1	0.55(16)
Si2	0.0501(11)	0.6564(16)	0.2634(20)	1	2.72(26)
O1	0.3700(8)	0.1609(12)	0.3168(15)	1	2.26(15)
O2	0.1177(10)	0.1642(15)	0.1416(16)	1	4.06(21)
O3	0.3860(8)	0.5001(10)	0.3136(17)	1	2.89(17)
O4	0.1460(8)	0.5102(9)	0.1145(14)	1	1.51(13)
O5	0.3947(9)	0.7688(9)	0.1131(16)	1	3.21(18)
O6	0.0934(7)	0.7969(7)	0.0412(15)	1	2.38(17)

Final fit parameters: $R(F^2)$ = 5.62%, R_{wp} = 5.19%, R_p = 3.90%

Table 8.2: Derived bond distances and angles for $Mg_{1.2}Cu_{0.8}Si_2O_6$ (e.s.d.s in parentheses)

Bond	Distance / Å	Bond Angle	Angle / °
Cu1_O1	2.123(10)	O1_Cu1_O2	87.4(4)
Cu1_O2	2.055(13)	O1_Cu1_O3	90.0(4)
Cu1_O3	2.044(11)	O1_Cu1_O4	80.5(4)
Cu1_O4	2.012(10)	O1_Cu1_O5	105.8(5)
Cu1_O5	2.419(10)	O2_Cu1_O3	92.6(5)
Cu1_O6	2.607(10)	O2_Cu1_O4	95.2(4)
		O2_Cu1_O5	158.3(5)
		O3_Cu1_O4	167.3(5)
		O3_Cu1_O5	70.7(4)
		O4_Cu1_O5	103.8(5)
Cu2_O1	2.170(10)	O1_Cu2_O1	92.0(4)
Cu2_O1	2.070(10)	O1_Cu2_O2	84.13(35)
Cu2_O2	2.139(13)	O1_Cu2_O2	85.9(5)
Cu2_O2	2.093(10)	O1_Cu2_O3	89.5(4)
Cu2_O3	2.118(11)	O1_Cu2_O4	174.7(5)
Cu2_O4	1.960(11)	O1_Cu2_O2	87.3(4)
		O1_Cu2_O2	177.5(7)
		O1_Cu2_O3	91.9(4)
		O1_Cu2_O4	83.0(4)
		O2_Cu2_O2	91.1(4)
		O2_Cu2_O3	173.5(5)
		O2_Cu2_O4	97.6(4)
		O2_Cu2_O4	99.1(5)
		O3_Cu2_O4	88.7(4)

8.4 UV to Near-infrared Spectroscopy

Solid state UV visible data were collected on an undiluted sample according to the method outlined in Chapter 2.

The spectrum observed shows an absorption band at about 800 nm, which is due to the Cu^{2+} ions being in octahedral sites. Along with this absorption band three other intensities are seen at 1020 nm, 1120 nm and 1300 nm, respectively.

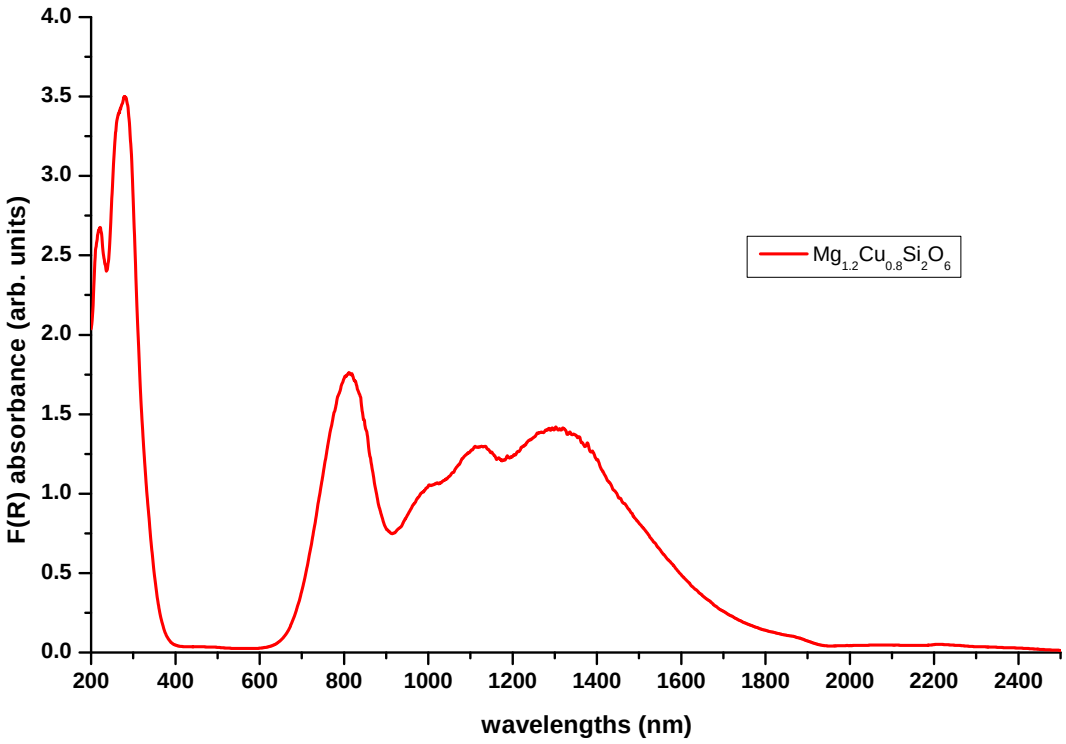

Figure 8.3: UV to near-infrared spectrum of magnesium copper pyroxene.

8.5 Discussion

In the clinopyroxene structure $Mg_{1.2}Cu_{0.8}Si_2O_6$, there are two sites that can accommodate the cations. From the *Rietveld* refinement data, copper atoms were found situated mainly in the second site (M2). This site occupancy preference is unlikely to be size related due to the similarity in size of copper(II) and magnesium(II) (0.73 Å and 0.72 Å respectively [68]). On the other hand, the ionic nature of Mg^{2+} compared to the covalent nature of Cu^{2+} qualitatively described by their chemical hardness (32.5 eV and 8.3 eV respectively [96]) may account for the preference of Cu^{2+} ions to accommodate the more directional bonding M2 site compared to the strongly distorted M1 site.

The octahedral M1 site undergoes a distortion which is not a *Jahn Teller* distortion. This may be energetically unfavourable for copper(II) which would therefore prefer to adopt the more conventionally octahedral M2 site.

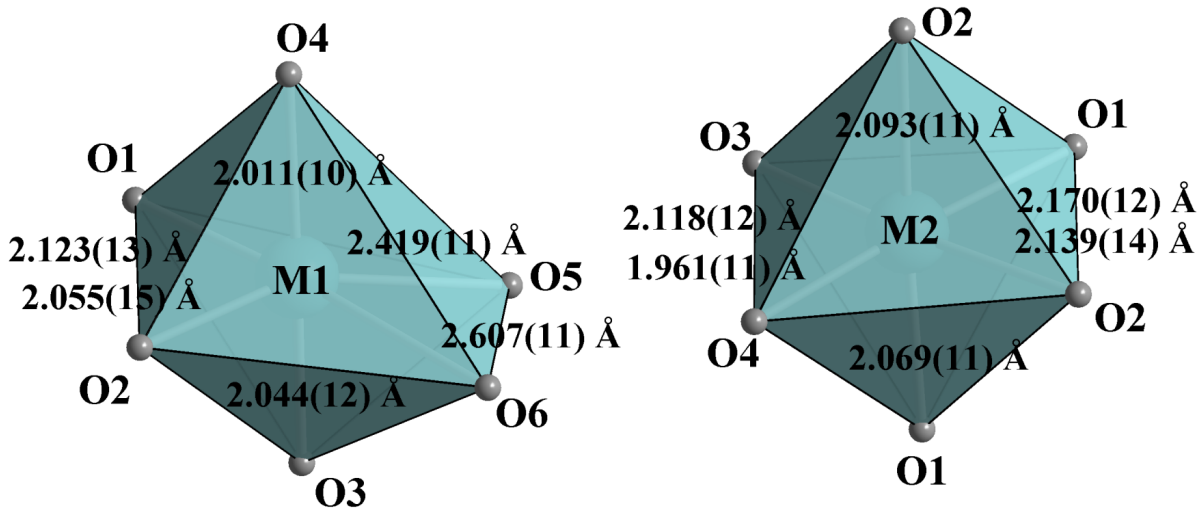

Figure 8.4: Octahedral sites M1 and M2 in the $Mg_{1.2}Cu_{0.8}Si_2O_6$ structure.

Looking closely at the M2 site and the derived bond lengths and angles obtained from the *Rietveld* refinement data in Table 8.2, this site can be considered as a slightly tetragonally distorted octahedral site with two shortened bond lengths compared to the basal plane (Figure 8.4). This distortion being negligible, the splitting of the e_g and t_{2g} hybridised orbitals should be minimised. The sharp absorption band centred at 800

nm can therefore be interpreted as being derived from the Cu^{2+} electronic transition $^2T_{2g} \leftarrow {}^2E_g$.

The three other bands result from copper(II) ions situated in the M1 site. However, due to the unusually strong distortion of this site, the absorption spectra can not be interpreted using a derived molecular model from common geometries. The relatively intense bands, compared to the amount of copper situated on this site (Table 8.1) is due to the absence of symmetry granting these three bands a fully symmetry allowed intensity.

8.6 Conclusion

The $Mg_{1.2}Cu_{0.8}Si_2O_6$ compound has been investigated using UV to near-infrared spectroscopy and powder neutron diffraction.

In this structure, the arrangement of the SiO_4 units into infinite chains and shape the cationic sites into two differently distorted octahedra. The copper(II) ions were shown to be situated preferentially in a slightly tetragonally compressed octahedral site due to its more covalent nature with regard to magnesium(II), resulting in a sharp absorption band at the very edge of the visible to the near-infrared region. The remaining Cu^{2+} ions are situated in the more distorted site and were shown to produce a rather intense absorption bands in the near-infrared due to the lack of symmetry of this site.

The synthesised pigment, despite its slow rate of formation during reaction, demonstrated excellent absorption properties in the near-infrared region and being colourless, it would be interesting to further investigate the method of synthesis in order to form nanoparticles of this compounds.

CHAPTER 9

CONCLUSION

Ideally, a transparent inorganic pigment with absorbing properties in the near-infrared region of the electromagnetic spectrum should have no visible colour, a high chemical and thermal stability, non-toxicity and very small particle sizes. This work has been focused on transition metal systems, characterising their structural properties to understand their physical properties.

Transition metal phosphates are known to provide chemically and thermally stable compounds. Due to the fact that phosphate entities are weak ligands and exist in various geometries formed by corner sharing of PO_4 tetrahedra, phosphate compounds containing transition metals are particularly interesting. Copper(II) phosphate systems, in particular, give a single absorption band at the edge of the visible to near-infrared region. The geometry of the cationic sites and their distortions have been shown to greatly influence the intensity of the absorption band and the position of the absorption maxima; materials with copper in five-fold sites exhibit a more intense absorption than materials with copper in tetragonally distorted octahedral sites. This has been demonstrated by the study of $Cu_2P_2O_7$ and $Cu_2P_4O_{12}$.

To influence the position of the absorption band one hypothesis was to form a mixed di-cation diphosphate. The idea was to weaken the ligand field strength of the phosphate ligands with the introduction of alkaline earth metal ions. Through the investigation of $CaCuP_2O_7$ and $SrCuP_2O_7$, such an indirect effect to influence the coordination sphere of the Cu^{2+} ions was shown to be minimal. However, the size of the alkaline earth cations has been seen to shape the five-fold sites, where copper(II) is situated.

Since copper phosphate materials are attractive pigments for the desired purpose and the size of the additional cation influences the position of the absorption band, it was natural to investigate some copper phosphate solid solutions implementing additional cations with similar ionic radii to copper. Such materials were the copper(II) mixed diphosphates $(Mg,Cu)_2P_2O_7$ and $(Zn,Cu)_2P_2O_7$. The copper ions in these pigments are situated in tetragonally distorted geometry, which reduces the absorption in the visible compared to copper ions in five-fold sites. The magnesium copper diphosphate was shown to have little impact for the design of a near-infrared absorbing pigment due to its low absorption intensity compared to the zinc copper diphosphate. On the other hand, the zinc copper diphosphate system presents intense absorption properties which were revealed to be a particularity of the zinc ions influencing the metal coordination sphere significantly.

It was found that instead of copper(II) also other non-toxic transition metal ions could be used to obtain a single absorption band in the near-infrared region. The solid solutions of $(Zn,Fe)_3(PO_4)_2$ were therefore studied. Within the investigated structure, iron(II) shows a strong preference to be situated in the octahedral site. Although the absorption band is not intense, it is very narrow which is perfect for laser welding purposes. On the other hand, the spectral study showed that some of the iron(II) ions are situated also in the distorted five-fold site, giving this material the ability to absorb a wide range of wavelengths in the near-infrared to infrared region.

Although more difficult to synthesise, another system with similar properties to phosphates exists which is the silicate system. One member of the $(Mg,Cu)_2Si_2O_6$ solid solution series was therefore studied. As expected, the ceramic method to obtain the material is economically non-viable for the pigment industry due to the high energy cost and effort necessary through several grinding cycles and the particularly slow rate of this reaction to yield the desired compound. However, the structural and spectroscopic investigation of this material shows promising near-infrared absorption properties. In this colourless pigment, the copper(II) ions are situated preferentially in a slightly tetragonally compressed octahedral site resulting in a sharp absorption band

at the very edge of the visible to the near-infrared region and because some of the Cu^{2+} ions are situated also in a more distorted site, the absorption covers the entire near-infrared region.

While, through this work, some very potent materials with the desired properties have been described, it is concluded that the best pigment with near-infrared absorbing properties that has been investigated was $Zn_{0.6}Cu_{1.4}P_2O_7$. Its light blue colour and its chemical and thermal stability make it already very interesting for application where transparency is not needed, such as painting. In addition it is a non-toxic material. Further improvement of the synthetic method to obtain nanoparticles of this material in order to make it transparent to visible light will enable it to be used into glass and plastic, and being an inorganic material, it will not be affected by the solar exposition.

Another material which is interesting for further investigation is the magnesium copper clinopyroxene. This pigment being colourless, already has the potential not to affect the colour property of the substrate. Therefore it is also considered as a promising candidate for industrial use.

APPENDIX **A**

MAGNESIUM COPPER PYROPHOSPHATE

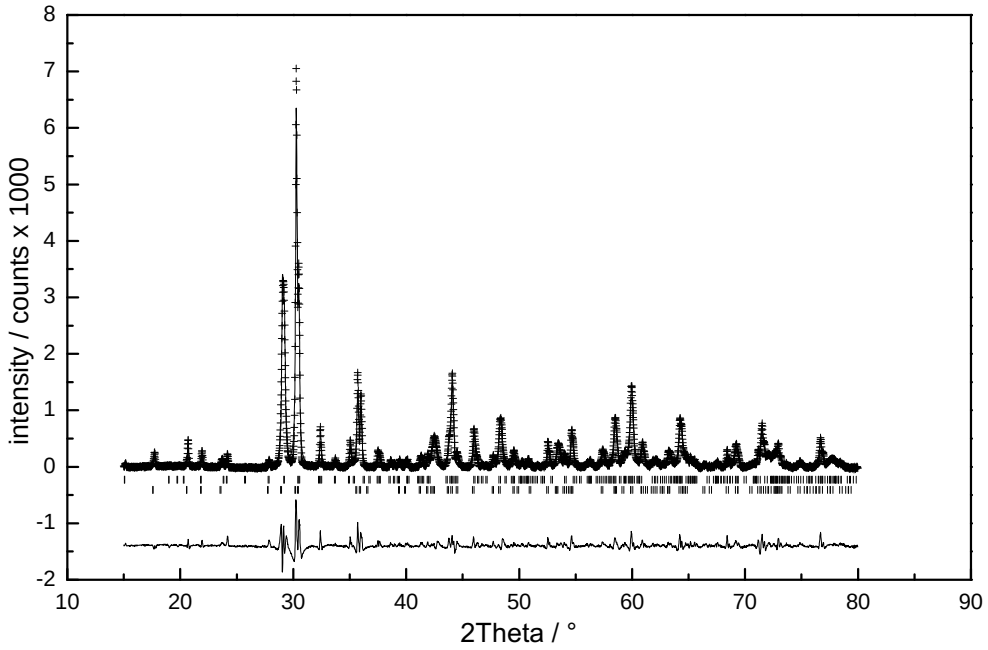

Figure A.1: *Le Bail* fit of $Mg_{0.4}Cu_{1.6}P_2O_7$. Observed data points are shown as crosses and the calculated pattern is shown as a solid line. The difference between the calculated and observed patterns is shown underneath. The position of the peaks for the $Mg_{0.4}Cu_{1.6}P_2O_7$ phase is marked by the second row of vertical lines, the first row marks the position of the peaks for $Cu_3(PO_4)_2$ phase. Relative to $Mg_{0.4}Cu_{1.6}P_2O_7$ the phase fraction of $Cu_3(PO_4)_2$ is 9%.

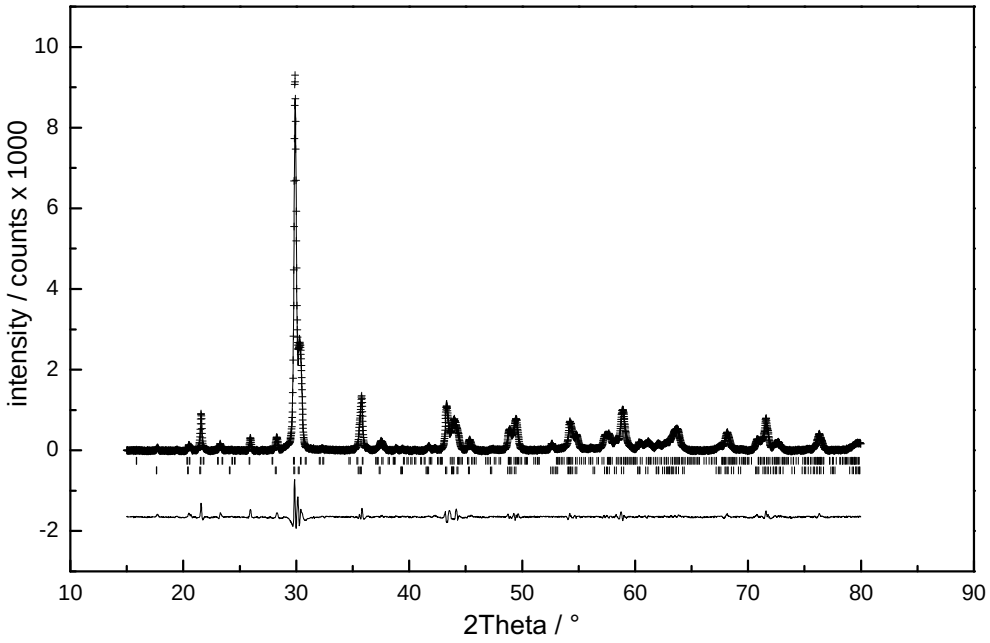

Figure A.2: *Le Bail* fit of $Mg_{1.6}Cu_{0.4}P_2O_7$. Observed data points are shown as crosses and the calculated pattern is shown as a solid line. The difference between the calculated and observed patterns is shown underneath. The position of the peaks for the $Mg_{1.6}Cu_{0.4}P_2O_7$ phase is marked by the second row of vertical lines, the first row marks the position of the peaks for $Mg_3(PO_4)_2$ phase. Relative to $Mg_{1.6}Cu_{0.4}P_2O_7$ the phase fraction of $Mg_3(PO_4)_2$ is 7%.

APPENDIX **B**

ZINC COPPER PYROPHOSPHATE

Table B.1: Refined crystallographic data for $Zn_{0.2}Cu_{1.8}P_2O_7$ (e.s.d.s in parentheses).

Name	x	y	z	Frac.	U_{iso} / Å^{2*}100
Zn1	0	0.68810(17)	1/2	0.1	1.48*
Cu1	0	0.68810(17)	1/2	0.9	1.48*
P1	0.69997(29)	1/2	0.9111(5)	1	0.62*
O1	0.87702(26)	1/2	0.22240(36)	1	0.58*
O2	0.70227(22)	0.65310(14)	0.72931(28)	1	1.76*
O3	1/2	0.45773(59)	0	0.5	2.36*

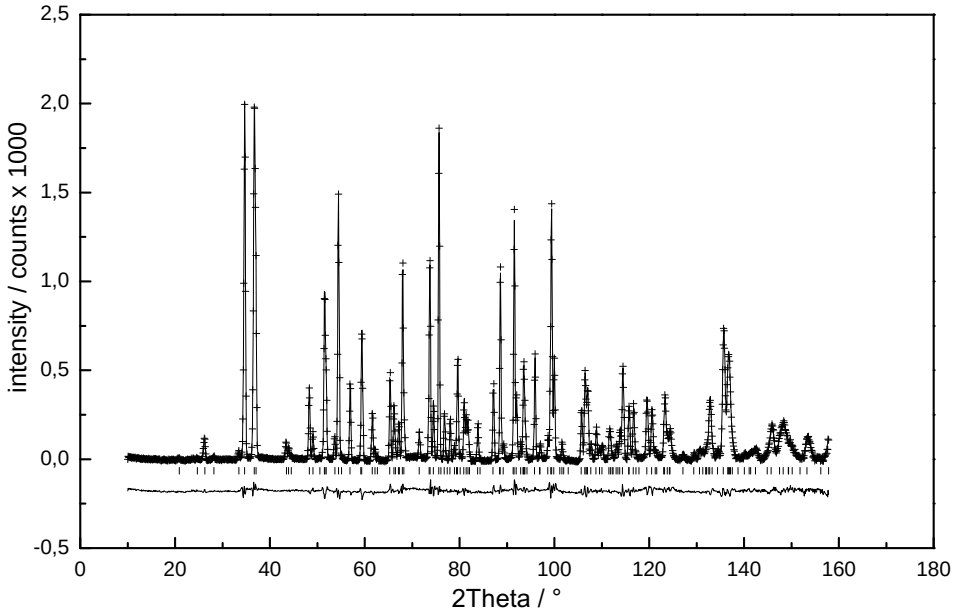

Figure B.1: *Rietveld* refinement profile fit of $Zn_{0.2}Cu_{1.8}P_2O_7$. Observed data points are shown as crosses and the calculated pattern is shown as a solid line. The difference between the calculated and observed patterns is shown underneath. The position of the peaks are marked by the row of vertical lines.

Table B.2: Refined crystallographic data for $Zn_{0.4}Cu_{1.6}P_2O_7$ (e.s.d.s in parentheses).

Name	x	y	z	Frac.	U_{iso} / Å^{2*}100
Zn1	0	0.68782(17)	1/2	0.2	1.57*
Cu1	0	0.68782(17)	1/2	0.8	1.57*
P1	0.70127(25)	1/2	0.9111(4)	1	0.74*
O1	0.87674(24)	1/2	0.22174(35)	1	0.71*
O2	0.70363(20)	0.65301(13)	0.72901(26)	1	1.91*
O3	1/2	0.45560(41)	0	0.5	2.30*

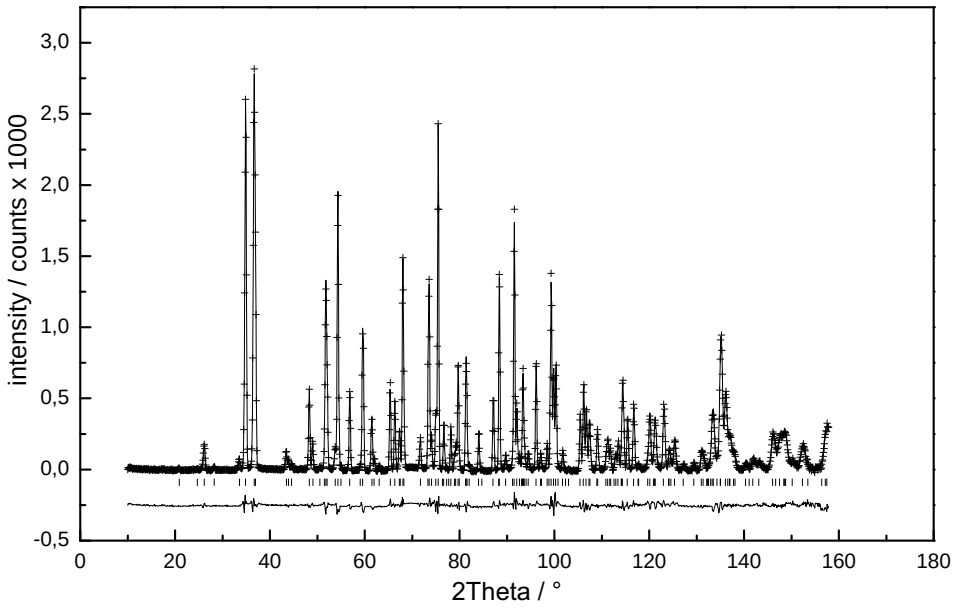

Figure B.2: *Rietveld* refinement profile fit of $Zn_{0.4}Cu_{1.6}P_2O_7$. Observed data points are shown as crosses and the calculated pattern is shown as a solid line. The difference between the calculated and observed patterns is shown underneath. The position of the peaks are marked by the row of vertical lines.

Table B.3: Refined crystallographic data for $Zn_{0.6}Cu_{1.4}P_2O_7$ (e.s.d.s in parentheses).

Name	x	y	z	Frac.	U_{iso} / Å^{2*}100
Zn1	0	0.68855(19)	1/2	0.3	1.78*
Cu1	0	0.68855(19)	1/2	0.7	1.78*
P1	0.70194(28)	1/2	0.9109(5)	1	0.89*
O1	0.87685(27)	1/2	0.22082(41)	1	0.83*
O2	0.70496(22)	0.65270(15)	0.72944(29)	1	2.16*
O3	1/2	0.45439(47)	0	0.5	2.83*

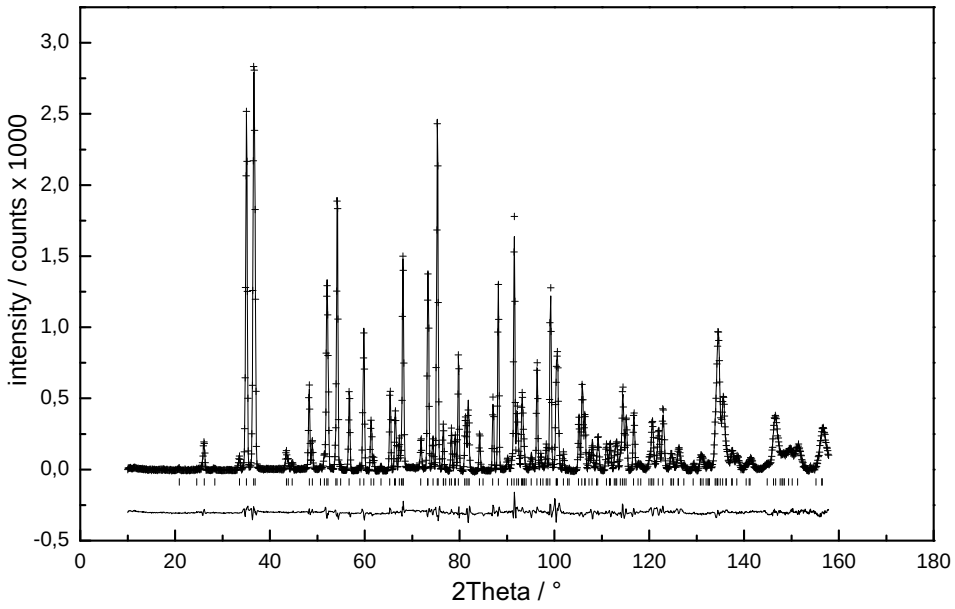

Figure B.3: *Rietveld* refinement profile fit of $Zn_{0.6}Cu_{1.4}P_2O_7$. Observed data points are shown as crosses and the calculated pattern is shown as a solid line. The difference between the calculated and observed patterns is shown underneath. The position of the peaks are marked by the row of vertical lines.

Table B.4: Refined crystallographic data for $Zn_{0.8}Cu_{1.2}P_2O_7$ (e.s.d.s in parentheses).

Name	x	y	z	Frac.	U_{iso} / Å^{2}*100
Zn1	0	0.68814(24)	1/2	0.4	1.88*
Cu1	0	0.68814(24)	1/2	0.6	1.88*
P1	0.7028(4)	1/2	0.9108(6)	1	0.89*
O1	0.87671(36)	1/2	0.2207(5)	1	0.80*
O2	0.70592(29)	0.65252(20)	0.7286(4)	1	2.22*
O3	1/2	0.45200(53)	0	0.5	2.53*

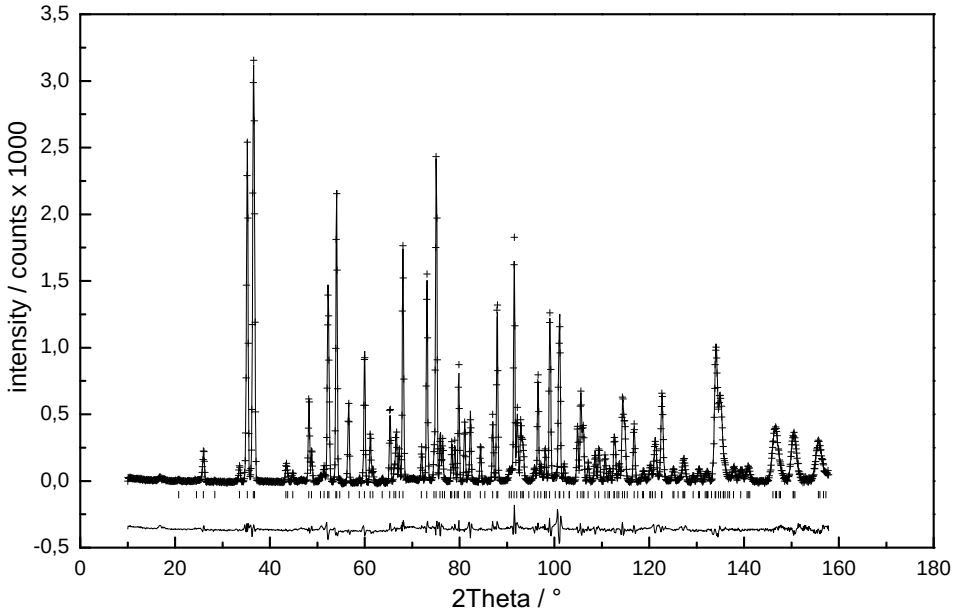

Figure B.4: *Rietveld* refinement profile fit of $Zn_{0.8}Cu_{1.2}P_2O_7$. Observed data points are shown as crosses and the calculated pattern is shown as a solid line. The difference between the calculated and observed patterns is shown underneath. The position of the peaks are marked by the row of vertical lines.

Table B.5: Refined crystallographic data for $ZnCuP_2O_7$ (e.s.d.s in parentheses).

Name	x	y	z	Frac.	U_{iso} / Å^{2*}100
Zn1	0	0.68819(25)	1/2	0.5	1.97*
Cu1	0	0.68819(25)	1/2	0.5	1.97*
P1	0.7040(4)	1/2	0.9111(6)	1	1.10*
O1	0.87716(37)	1/2	0.2195(5)	1	0.88*
O2	0.70709(29)	0.65239(20)	0.7290(4)	1	2.34*
O3	1/2	0.45068(53)	0	0.5	2.70*

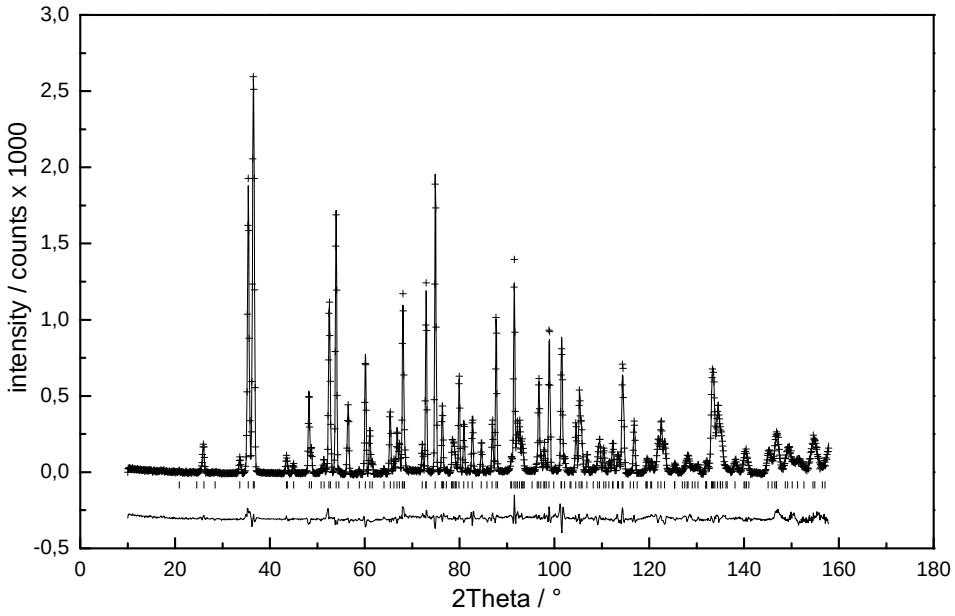

Figure B.5: *Rietveld* refinement profile fit of $ZnCuP_2O_7$. Observed data points are shown as crosses and the calculated pattern is shown as a solid line. The difference between the calculated and observed patterns is shown underneath. The position of the peaks are marked by the row of vertical lines.

Table B.6: Refined crystallographic data for $Zn_{1.2}Cu_{0.8}P_2O_7$ (e.s.d.s in parentheses).

Name	x	y	z	Frac.	U_{iso} / Å^{2*}100
Zn1	0	0.688717	1/2	0.620(15)	1.96*
Cu1	0	0.688717	1/2	0.380(15)	1.96*
P1	0.706197	1/2	0.911406	1	1.38*
O1	0.876459	1/2	0.218902	1	0.95*
O2	0.708543	0.651206	0.728580	1	2.25*
O3	1/2	0.449966	0	0.5	3.05*

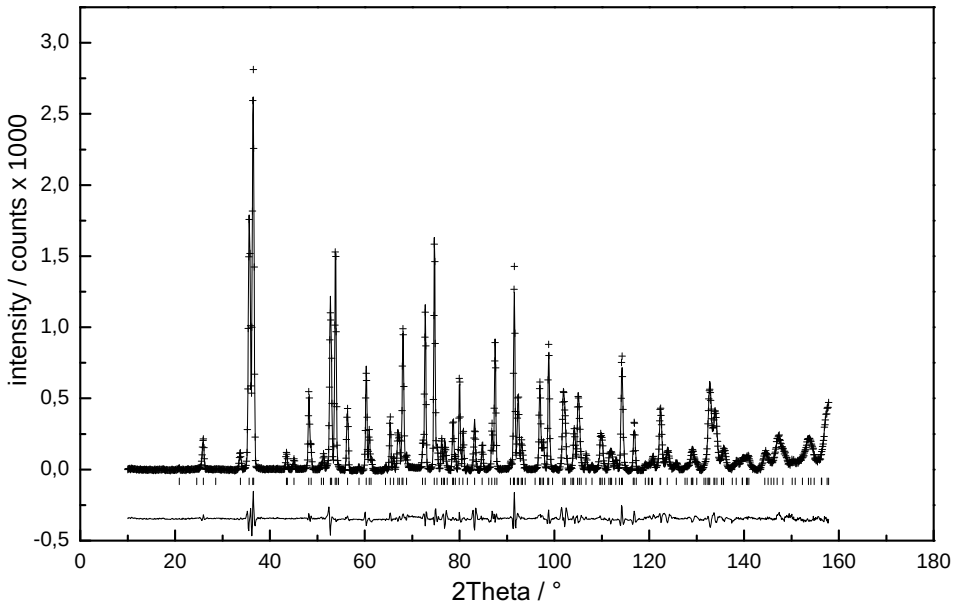

Figure B.6: *Rietveld* refinement profile fit of $Zn_{1.2}Cu_{0.8}P_2O_7$. Observed data points are shown as crosses and the calculated pattern is shown as a solid line. The difference between the calculated and observed patterns is shown underneath. The position of the peaks are marked by the row of vertical lines.

Table B.7: Refined crystallographic data for $Zn_{1.4}Cu_{0.6}P_2O_7$ (e.s.d.s in parentheses).

Name	x	y	z	Frac.	U_{iso} / Å^{2*}100
Zn1	0	0.6887(4)	1/2	0.7	2.33*
Cu1	0	0.6887(4)	1/2	0.3	2.33*
P1	0.7058(5)	1/2	0.9118(8)	1	1.56*
O1	0.8771(4)	1/2	0.2183(6)	1	0.83*
O2	0.7108(4)	0.65139(22)	0.7277(4)	1	2.42*
O3	1/2	0.44951(66)	0	0.5	2.93*

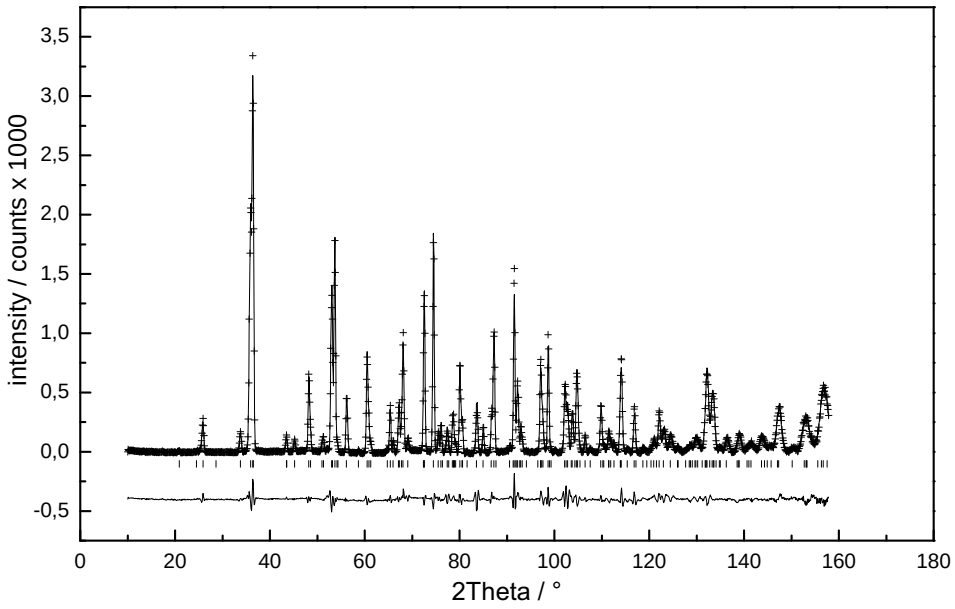

Figure B.7: *Rietveld* refinement profile fit of $Zn_{1.4}Cu_{0.6}P_2O_7$. Observed data points are shown as crosses and the calculated pattern is shown as a solid line. The difference between the calculated and observed patterns is shown underneath. The position of the peaks are marked by the row of vertical lines.

Table B.8: Refined crystallographic data for $Zn_{1.6}Cu_{0.4}P_2O_7$ (e.s.d.s in parentheses).

Name	x	y	z	Frac.	U_{iso} / Å^{2*}100
Zn1	0	0.6889(4)	1/2	0.8	2.36*
Cu1	0	0.6889(4)	1/2	0.2	2.36*
P1	0.7054(5)	1/2	0.9107(7)	1	1.34*
O1	0.8777(4)	1/2	0.2177(6)	1	0.88*
O2	0.7118(4)	0.65122(24)	0.7274(4)	1	2.26*
O3	1/2	0.45023(72)	0	0.5	3.16*

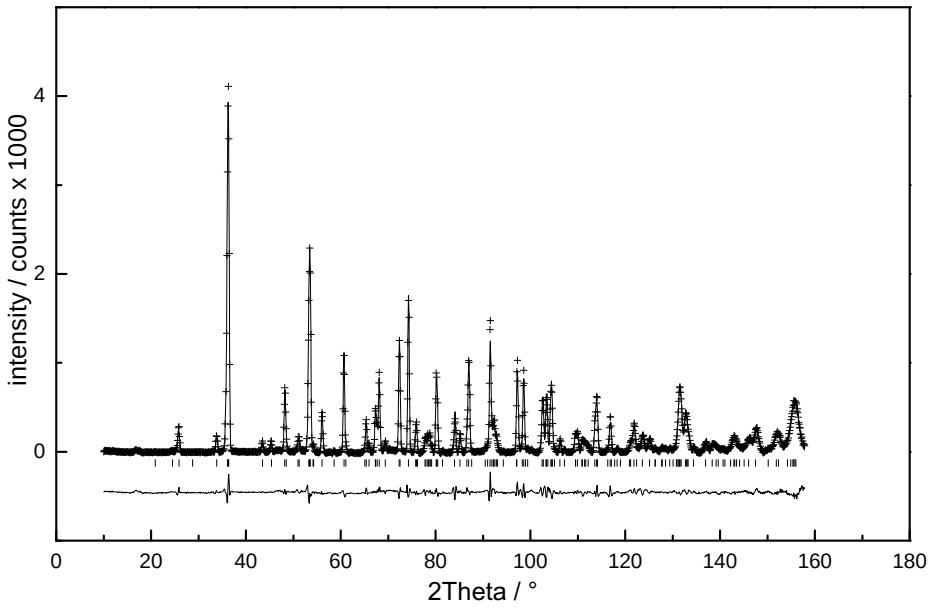

Figure B.8: *Rietveld* refinement profile fit of $Zn_{1.6}Cu_{0.4}P_2O_7$. Observed data points are shown as crosses and the calculated pattern is shown as a solid line. The difference between the calculated and observed patterns is shown underneath. The position of the peaks are marked by the row of vertical lines.

Table B.9: Refined crystallographic data for $Zn_{1.8}Cu_{0.2}P_2O_7$ (e.s.d.s in parentheses).

Name	x	y	z	Frac.	U_{iso} / Å^{2*}100
Zn1	0	0.6883(9)	1/2	0.9	3.56*
Cu1	0	0.6883(9)	1/2	0.1	3.56*
P1	0.7034(13)	1/2	0.9130(16)	1	2.20*
O1	0.8754(9)	1/2	0.2166(14)	1	1.80*
O2	0.7126(9)	0.6514(5)	0.7311(9)	1	3.10*
O3	1/2	0.4442(13)	0	0.5	2.52*

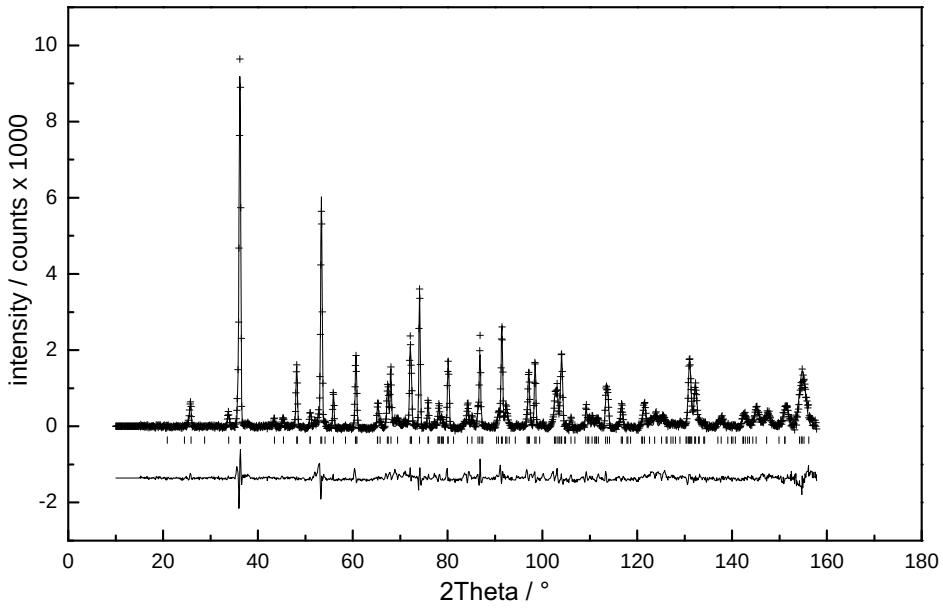

Figure B.9: *Rietveld* refinement profile fit of $Zn_{1.8}Cu_{0.2}P_2O_7$. Observed data points are shown as crosses and the calculated pattern is shown as a solid line. The difference between the calculated and observed patterns is shown underneath. The position of the peaks are marked by the row of vertical lines.

BIBLIOGRAPHY

[1] J. R. Barnett, S. Miller, and E. Pearce, "Colour and art: A brief history of pigments," *Optics & Laser Technology*, vol. 38, p. 445, 2006.

[2] P. Lewis, *Pigment Handbook Volume I, Properties and Economics*, 2nd ed., Wiley Interscience, Ed. New York: Wiley Interscience, 1990, vol. Volume I, Properties and Economics.

[3] G. Buxbaum and G. Pfaff, *Industrial Inorganic Pigments*, G. Buxbaum and G. Pfaff, Eds. Mörlenbach: Wiley VCH, 2005.

[4] J. Meng, G. Yang, L. Yan, and X. Wang, "Synthesis and characterization of magnetic nanometer pigment Fe_3O_4," *Dyes Pigm.*, vol. 66, p. 109, 2005.

[5] H. Hibst, "Magnetic pigments for recording information," *J. Magn. Magn. Mater.*, vol. 74, p. 193, 1988.

[6] T. Brock, M. Groteklas, and P. Mischke, *European coatings handbook*, Ulrich Zorll, Ed. Hannover: Vincentz, 2000.

[7] N. Serpone, D. Dondi, and A. Albini, "Inorganic and organic UV filters: Their role and efficacy in sunscreens and suncare products," *Inorg. Chim. Acta*, vol. 360, p. 794, 2007.

[8] R. Levinson, P. Berdhal, and H. Akbari, "Solar spectral optical properties of pigments - Part II: survey of common colorants," *Sol. Energy Mater. Sol. Cells*, vol. 89, p. 351, 2005.

[9] A. Pabst, "Structures of some tetragonal sheet silicates," *Acta Crystallogr., Sect. A*, vol. 12, p. 733, 1959.

[10] R. Marchand, R. Pastuszak, and Y. Laurent, *Rev. Chim. Miner.*, vol. 19, p. 684, 1982.

[11] M. Orchin, R. S. Macomber, A. Pinhas, and R. M. Wilson, *The Vocabulary and Concepts of Organic Chemistry*, 2nd ed., John Wiley & Sons, Inc., Ed. Hoboken: John Wiley & Sons, Inc., 2005.

[12] D. Nicholls, *Complexes and First-Row Transition elements*, D. Nicholls, Ed. London: Macmillan Chemistry Text, 1974.

[13] G. L. Miessler and D. A. Tarr, *Inorganic Chemistry*, 2nd ed., M. Hart, Ed. Englewood Cliffs: Prentice Hall, Inc., 1998.

[14] J. E. Huheey, E. A. Keiter, and R. L. Keiter, *Inorganic Chemistry Principle of Structure and Reactivity*, J. Piro, Ed. New York: HarperCollins College Publishers, 1993.

[15] H. A. Jahn, *Proc. R. Soc. London, Ser. A*, vol. A164, p. 117, 1938.

[16] H. A. Jahn and E. Teller, *Proc. R. Soc. London, Ser. A*, vol. A161, p. 220, 1937.

[17] D. F. Shriver, P. W. Atkins, T. L. Overton, J. P. Rourke, M. T. Weller, and F. A. Armstrong, *Inorganic Chemistry*, Oxford University Press, Ed. Oxford: Oxford University Press, 2006.

[18] R. J. D. Tilley, *Colour and optical properties of materials*, John Wiley & Sons, Ed. Chichester: John Wiley & Sons, 2000.

[19] A. Williams, *A theoretical approach to inorganic chemistry*, Springer, Ed. Berlin: Springer-Verlag, 1979.

[20] P. W. Atkins, *Physical chemistry*, Oxford University Press, Ed. Oxford: Oxford University Press, 2001.

[21] M. Fox, *Optical Properties of Solids*, Oxford University Press, Ed. Oxford: Oxford University Press, 2004.

[22] T. Xu, C. Song, Y. Liu, and G. Han, "Band structures of TiO_2 doped with N, C and B," *J. Zhejiang Univ. Sci. B.*, vol. 7, p. 299, 2006.

[23] A. K. Cheetham and P. Day, *Solid State Chemistry Compounds*, Clarendon Press, Ed. Oxford: Clarendon Press, 1992.

[24] R. S. H. Liu and A. E. Asato, "Tuning the color and excited state properties of the azulenic chromophore: NIR absorbing pigments and materials," *J. Photochem. Photobiol., C*, vol. 4, no. 3, pp. 179–194, 2003.

[25] J. Fabian, H. Nakazumi, and M. Matsuoka, "Near-Infrared Absorbing Dyes," *Chem. Rev.*, vol. 92, p. 1197, 1992.

[26] C. M. Warwick and M. Gordon, "Application studies using through-transmission laser welding of polymers," in *Joining Plastics*, 2006.

[27] R. A. Sallavanti and L. P. Frieder, "Visibly transparent dyes for through-transmission laser welding," US Patent 6 656 315, 2003.

[28] D. Reiner and K. Matthias, "Coloured inscription and marking of plastics and surface coatings," US Patent 6 924 077, 2005.

[29] A. Ritter, *Smart materials in architecture, interior architecture and design*, A. Muller, Ed. Basel: Birkhauser, 2007.

[30] M. F. Al-Kuhaili, A. H. Al-Aswad, S. M. A. Durrani, and I. A. Bakhtiari, "Transparent heat mirrors based on tungsten oxide-silver multilayer structures," *Solar Energy*, vol. 83, p. 1571, 2009.

[31] S. Schelm and G. B. Smith, "Dilute LaB_6 nanoparticles in polymer as optimized clear solar control glazing," *Appl. Phys. Lett.*, vol. 82, p. 4346, 2003.

[32] U. Lehmann and D. Heizler, "Dithiolene metal complex colourless ir absorbers," International Patent WO 2008/086 931 A1, 2008.

[33] A. F. Wells, *Structural Inorganic Chemistry*, 4th ed., A. F. Wells, Ed. Oxford: Oxford University Press, 1975.

[34] M. T. Averbuch-Pouchot and A. Durif, *Topics in phosphate chemistry*, A. Durif, Ed. London: World Scientific Publishing Co. Pte. Ltd., 1996.

[35] N. N. Greenwood and A. Earnshaw, *Chemistry of the elements*, N. N. Greenwood, Ed. Oxford: Elsevier, 2005.

[36] E. M. Hughes, "Synthesis and characterisation of inorganic pigments," Ph.D. dissertation, University of Southampton, 1999.

[37] M. Bethencourt, F. J. Botana, M. Marcos, R. M. Osuna, and J. M. Sanchez-Amaya, "Inhibitor properties of "green" pigments for paint," *Prog. Org. Coat.*, vol. 46, p. 280, 2003.

[38] W. H. Zachariasen, "The structure of thortveitite, $Sc_2Si_2O_6$," *Z. Kristallogr.*, vol. 73, p. 1, 1930.

[39] C. Chambers and A. K. Holliday, *Modern Inorganic Chemistry*, C. Chambers, Ed. London: Butterworths, 1975.

[40] A. R. West, *Solid State Chemistry and Its Applications*, John Wiley & Sons, Ed. Chichester: John Wiley & Sons, 1984.

[41] C. J. Brinker and G. W. Scherer, *Sol-Gel Science, the physics and chemistry of sol-gel processing*, Academic Press Limited, Ed. London: Academic Press Inc., 1990.

[42] M. Woolfson, *An Introduction to X-ray Crystallography*, Cambridge University Press, Ed. Cambridge: Cambridge University Press, 1970.

[43] W. L. Bragg, "The Diffraction of Short Electromagnetic Waves by a Crystal," *Math. Proc. Cambridge Philos. Soc.*, vol. 17, p. 43, 1913.

[44] M. T. Weller, *Inorganic Materials Chemistry*, Oxford University Press, Ed. Oxford: Oxford University Press, 1994.

[45] A. K. Cheetham and P. Day, *Solid State Chemistry: Techniques*, Clarendon, Ed. Oxford: Oxford Science Publications, 1988.

[46] T. Hahn, *International Tables For Crystallography*, D. R. P. Co., Ed. Dordrecht: D. Reidel, 1983, vol. A.

[47] Bruker Advanced X-rays Solutions, *EVA*, 6th ed., Bruker, 2000.

[48] J. Laugier and B. Bochu, *CELLREF*, Laboratoire des Matériaux et du Génie Physique, Ecole Nationale Supérieure de Physique de Grenoble INPG (France), 2000.

[49] D. P. Mitchell and P. N. Powers, "Bragg Reflection of Slow Neutrons," *Phys. Rev.*, vol. 50, p. 486, 1936.

[50] Institut Laue Langevin, "High-resolution two-axis diffractometer d1a," Internet, 2009. [Online]. Available: http://www.ill.eu/instruments-support/instruments-groups/instruments/d1a/

[51] Joint Committee on Powder Diffraction Standards, *International Centre for Diffraction Data*, Pennsylvannia, 19073-3273.

[52] H. M. Rietveld, "Line profiles of neutron powder-diffraction peaks for structure refinement," *Acta Cryst.*, vol. 22, p. 151, 1967.

[53] ——, "A profile refinement method for nuclear and magnetic structures," *J. Appl. Crystallogr.*, vol. 2, p. 65, 1969.

[54] A. C. Larson and R. B. V. Dreele, *General Structure Analysis System*, ms-h805 ed., Los Alamos National Laboratory, USA, 1990, n M 87545.

[55] B. Toby, "EXPGUI," *J. Appl. Crystallogr.*, vol. 34, p. 210, 2001.

[56] M. J. Buerger, *Contemporary Crystallography*, McGraw-Hill, Ed. New York: McGraw-Hill, 1970.

[57] G. Caglioti, A. Paoletti, and F. P. Ricci, *Nucl. Instrum. Methods Phys. Res.*, vol. 35, p. 223, 1958.

[58] P. Kubelka and F. Z. Munk, *Tech. Phys.*, vol. 12, p. 539, 1931.

[59] P. Kubelka, *J. Opt. Soc. Am.*, vol. 38, p. 448, 1948.

[60] P. Goodhew, J. Humphreys, and R. Beanland, *Electron Microscopy and Analysis*, 3rd ed., Taylor and Francis, Eds. London: Taylor and Francis, 2001.

[61] M. Newville, "Fundamentals of x-ray absorption fine structure," in *Consortium for Advanced Radiation Sources*, 2004.

[62] D. C. Koningsberger, B. L. Mojet, G. E. van Dorssen, and D. E. Ramaker, "XAFS spectroscopy; fundamental principles and data analysis," *Top. Catal.*, vol. 10, p. 143, 2000.

[63] P. A. Lee and J. B. Pendry, *Phys. Rev. B: Condens. Matter*, vol. 11, p. 2795, 1975.

[64] N. Binsted, *Program for the Analysis of X-ray Absorption Spectra*, University of Southampton, Southampton, 1998.

[65] N. Binsted, J. W. Campbell, S. J. Gurnman, and P. C. Stephenson, *EXCURV98 computer program*, SERC Daresbury Laboratory, Daresbury, 1992.

[66] G. Frank, E. Kauer, H. Kostlin, and F. Schmitte, "Transparent heat-reflecting coatings for solar applications based on highly doped tin oxide and indium oxide," *Sol. Energy Mater. Sol. Cells*, vol. 8, p. 387, 1983.

[67] W. Chen and Y. Kaneko, "Electrochromism of vanadium oxide films doped by rare-earth (Pr, Nd, Sm, Dy) oxides," *J. Electroanal. Chem.*, vol. 559, p. 83, 2003.

[68] R. D. Shannon, "Revised Effective Ionic Radii and Systematic Studies of Interatomic Distances in Halides and Chalcogenides," *Acta Crystallogr., Sect. A*, vol. 32, p. 155, 1976.

[69] N. G. Schmahl and G. F. Eikerling, "Ueber Kryptomodifikationen des Cu(II)-Oxids." *Z. Phys. Chem. (Muenchen, Ger.)*, vol. 62, p. 268, 1968.

[70] A. Murali and J. Rao, "Spectroscopic investigations on Cu(II) ions doped in the alkali lead boratellurate glasses," *J. Phys.: Condens. Matter*, vol. 11, p. 7921, 1999.

[71] E. I. Solomon, J. W. Hare, and H. B. Gray, "Spectroscopic studies and a structural model for blue copper centers in proteins," *Proc. Natl. Acad. Sci. U. S. A.*, vol. 73, p. 1389, 1976.

[72] D. R. Lide, *CRC Handbook of chemistry and physics*, D. R. Lide, Ed. Boca Raton: CRC Press, 2004.

[73] F. P. Okamura, S. Sueno, I. Nakai, and A. Ono, "Crystal structure of $Ba_2YCu_{3-x}O_{7-y}$. A superconductive compound determined by X-ray single crystal diffraction method." *Mater. Res. Bull.*, vol. 22, p. 1081, 1987.

[74] S. Meseguer, M. A. Tena, C. Gargori, J. A. Badenes, M. Llusar, and G. Monros, "Structure and colour of cobalt ceramic pigments from phosphates," *Ceram. Int.*, vol. 33, p. 843, 2007.

[75] K. B. N. Sharma, L. R. Moorthy, B. J. Reddy, and S. Vedanand, "EPR and electronic absorption spectra of copper bearing turquoise mineral," *Phys. Lett. A*, vol. 132, p. 293, 1988.

[76] B. E. Robertson and V. Calvo, "The crystal structure and phase transformation of α-$Cu_2P_2O_7$," *Acta Cryst.*, vol. 22, p. 665, 1967.

[77] G. L. Shoemaker, J. B. Anderson, and E. Kostiner, "Copper(II) Phosphate," *Acta Crystallogr., Sect. B*, vol. 33, p. 2969, 1977.

[78] M. Brunel-Lauegt and J. C. Guitel, "Structure cristalline de $Cu_5O_2(PO_4)_2$," *Acta Crystallogr., Sect. B*, vol. 33, p. 3465, 1977.

[79] J. B. Forsyth, C. Wilkinson, S. Paster, and H. Effenberger, "The antiferromagnetic structure of triclinic copper(II) phosphate," *J. Phys.: Condens. Matter*, vol. 2, p. 1609, 1990.

[80] M. Laugt, G. Bassi, I. Tordjman, and J. C. Guitel, "Crystal structure of copper tetrametaphosphate, $Cu_2P_4O_{12}$," *Acta Crystallogr., Sect. B*, vol. 28, p. 201, 1972.

[81] J. B. Anderson, G. L. Shoemaker, and E. Kostiner, "The crystal structure of $Cu_4(PO_4)_2O$," *J. Solid State Chem.*, vol. 25, p. 49, 1978.

[82] A. Boukhari, A. Moqine, and S. Flandrois, "Synthesis and Characterization of a New Copper(II) Mixed Diphosphates (M, $Cu)_2P_2O_7$ with M = Mg, Ca, Sr and Ba," *J. Solid State Chem.*, vol. 87, p. 251, 1990.

[83] D. Riou and M. Goreau, "$CaCuP_2O_7$: a structure closely related to α $Ca_2P_2O_7$," *Acta Crystallogr., Sect. C*, vol. 46, p. 1191, 1990.

[84] A. Moqine, A. Boukhari, L. Elammari, and J. Durand, "Structure Cristalline du Diphosphate $SrCuP_2O_7$," *J. Solid State Chem.*, vol. 107, p. 368, 1993.

[85] C. Calvo, "The crystal structure of α-$Ca_2P_2O_7$," *Phase Transition*, vol. 38, p. 127, 1992.

[86] N. Clavier, N. Dacheux, P. Martinez, V. Brandel, R. Podor, and P. L. Coustumer, "Synthesis and characterisation of low-temperature precursors of thorium-uranium (IV) phosphate-diphosphate solid solution," *J. Nucl. Mater.*, vol. 335, p. 397, 2004.

[87] M. P. Carrasco, M. C. Guillem, and J. Alamo, "Synthesis and structural study of sodium titanium phosphate-sodium tin phosphate solid solutions. II. Thermal expansion," *Mater. Res. Bull.*, vol. 28, p. 547, 1993.

[88] A. Moqine, A. Boukhari, and S. Flandrois, "The solid solution and magnetic properties of $(Mg,Cu)_3(PO_4)_2$ phosphates," *Mater. Res. Bull.*, vol. 22, p. 965, 1987.

[89] C. Calvo, "Refinement of the crystal structure of β-$Mg_2P_2O_7$," *Can. J. Chem.*, vol. 43, p. 1139, 1965.

[90] S. F. A. Kettle, *Physical Inorganic Chemistry A Coordination Chemistry Approach*, W. H. Freeman, Ed. Oxford: Spektrum Academic Publishers, 1996.

[91] A. Elmaadi, A. Boukhari, E. M. Holt, and S. Flandrois, "Synthesis And Characterization Of $(Zn,M)_2P_2O_7$ (M=Mn, Cu)," *Journal Of Alloys And Compounds*, vol. 205, p. 243, 1994.

[92] B. E. Robertson and C. Calvo, "Crystal structure of β - $Cu_2P_2O_7$," *Can. J. Chem.*, vol. 46, p. 605, 1968.

[93] V. F. Sears, "Neutron scattering lengths and cross sections," *Neutron News*, vol. 3, p. 26, 1992.

[94] C. Calvo, "The crystal structure and phase transitions of β−$Zn_2P_2O_7$," *Can. J. Chem.*, vol. 43, p. 1147, 1965.

[95] M. Moreno, M. Bariuso, and J. Aramburu, *J. Phys.: Condens. Matter*, vol. 4, p. 9481, 1992.

[96] R. G. Parr and R. G. Pearson, "Absolute hardness: Companion Parameter to Absolute Electronegativity," *J. Am. Chem. Soc.*, vol. 105, p. 7512, 1983.

[97] D. Sutton, *Electronic Spectra of Transition Metal Complexes*, P. Sykes, Ed. London: McGraw-Hill London, 1968.

[98] H. Annersten, T. Ericsson, and A. G. Nord, "The cation ordering in iron-containing zinc and magnesium orthophosphates determined from Mossbauer Spectroscopy," *J. Phys. Chem. Solids*, vol. 41, p. 1235, 1980.

[99] A. G. Nord, "Use of Rietveld technique for estimating cation distributions," *J. Appl. Crystallogr.*, vol. 17, p. 55, 1984.

[100] J. K. Warner, A. K. Cheetham, and D. E. Cox, "Determination Of The Cation Distribution In $NiFe_2(PO_4)_2$ Using Resonant X-Ray And Neutron Powder Diffraction," *J. Appl. Crystallogr.*, vol. 28, pp. 494–502, 1995.

[101] B. E. Douglas, D. H. McDaniel, and J. J. Alexander, *Concepts and models of Inorganic Chemistry*, 2nd ed., B. E. Douglas, Ed. New York: Jhon Wiley &Sons, Inc., 1983.

[102] S. Ohlhorst, H. Behrens, and F. Holtz, "Compositional dependence of molar absorptivities of near-infrared OH^- and H_2O bands in rhyolitic to basaltic glasses," *Chem. Geol.*, vol. 174, p. 5, 2001.

[103] W. B. White and K. L. Keester, "Optical absorption spectra of iron in the rock-forming silicates," *Am. Mineral.*, vol. 51, p. 774, 1966.

[104] Y. Jean, *Molecular Orbitals of Transition Metal Complexes*, Oxford University Press, Ed. Oxford: Oxford University Press, 2005.

[105] K. H. Breuer, W. Eysel, and R. Mueller, "Structural and chemical varieties of dioptase, $Cu_6(Si_6O_{18})(H_2O)_6$ II. Structural properties." *Z. Kristallogr.*, vol. 187, p. 15, 1989.

[106] K. H. Breuer, W. Eysel, and M. Behruzi, "Copper(II) silicates and germanates with chain structures," *Z. Kristallogr.*, vol. 176, p. 219, 1986.

[107] N. Morimoto, D. E. Appleman, and H. T. Evans, "The crystal structure of clinoenstatite and pigeonite," *Z. Kristallogr.*, vol. 114, p. 120, 1960.